DIAGNOSTICS IN A HIGH DENSITY

Z PINCH PLASMA

by

Brian K. Hilko

B.Sc., University of Waterloo, 1974
M.Sc., University of British Columbia, 1977

A THESIS SUBMITTED IN PARTIAL FULFILLMENT OF
THE REQUIREMENTS FOR THE DEGREE OF
DOCTOR OF PHILOSOPHY

in

THE FACULTY OF GRADUATE STUDIES
(Department of Physics)

We accept this thesis as conforming
to the required standards

THE UNIVERSITY OF BRITISH COLUMBIA

May 1981

BRIAN HILKO

Department of PHYSICS

The University of British Columbia
2075 Wesbrook Place
Vancouver, Canada
V6T 1W5

Date NOVEMBER 27, 1981.

ABSTRACT

A Z-pinch plasma, suitable for the study of CO_2 laser-plasma interaction mechanisims, is thoroughly diagnosed using a number of non-perturbing, optical probe techniques.

Simple streak and shadow methods give an important preliminary view of the spatial distribution and radial dynamics of plasma during the high compression phase. The electron density and temperature are determined as a function of time by spectrally resolving the ion feature of Thomson scattered ruby laser light. Peak electron densities well in excess of 1×10^{19} cm^{-3} and temperatures near 50 eV are observed. Complementing the scattering results, holographic interferometry is performed to examine both the temporal and spatial variation of electron density.

The diagnostics used are well suited to the examination of moderately dense, hot plasma and have been developed specifically for application in our laser-plasma interaction studies.

TABLE OF CONTENTS

TABLE OF CONTENTS (Cont'd)

LIST OF TABLES

LIST OF FIGURES

LIST OF FIGURES (Cont'd)

ACKNOWLEDGEMENTS

As part of a large experimental project, I have had the great pleasure of working alongside a number of fine people. I wish to express my sincere appreciation and thanks to Dr. Jochen Meyer for his aid and supervision throughout this project. Dr. G. Albrecht, H. Houtman, Dr. C.J. Walsh and A. Cheuck have been unselfish and continual sources of help and encouragement.

My stay at U.B.C. would not have been possible without the financial assistance of the Plasma Physics Group. This work has been supported by a grant from the National Science and Engineering Research Council of Canada.

CHAPTER 1 INTRODUCTION

This thesis reports a series of diagnostic experiments that have been specifically developed in conjunction with, and as part of, an ongoing investigation of laser-plasma interaction mechanisms. Therefore, in this introduction, some consideration will be given to the experiment as a whole in order to place the objectives of this thesis work into full perspective.

The peak compression phase of a Z-pinch discharge in Helium is the target plasma, into which a high power CO_2 laser beam is focussed. High intensity laser light can couple to the plasma via a number of different non-linear processes (Siebe, 1974; Milroy et.al., 1979). The effects of the laser on the plasma depend strongly on the local temperature and density distribution of the target. As well, many of the coupling processes can (and often do) occur simultaneously. The experiments that are underway at this laboratory will attempt to isolate and study the fundamentally different processes of laser-plasma interactions. The following discussion will indicate that the Z-pinch plasma is very well suited to such an endeavour.

In many similar experiments, the target plasma is created during the early portions of the incident laser pulse (Grek et.al., 1978; Jackel et.al. 1976; Milroy et.al., 1979). In these cases, however, it is difficult to divorce the processes of plasma formation and laser-plasma interaction. Therefore, it seems more desirable to study the interactions using a target plasma, which has been pre-formed, and whose initial conditions can be established independently of the laser pulse.

In a Z-pinch discharge, the progression of plasma collapse will make available a wide range of plasma conditions. The plasma parameters, such as density, temperature, and corresponding gradients, vary reproducibly as functions of radius and time. As well, the plasma conditions in the Z-pinch change on a time scale which is long compared to the incident laser pulse. Hence, the Z-pinch plasma may be used as a target of varying but controlled and predictable parameters. If the plasma conditions are well known before hand, one can hope to study the laser-plasma interaction process in detail. It is, therefore, very important to establish the initial conditions for the interaction studies. This has been done, and the results of this thesis constitute a thorough and detailed experimental evaluation of the Z-pinch plasma parameters, prior to irradiation with the CO_2 laser.

The primary subject here is optical diagnostics of the Z-pinch using ruby laser light, but, the underlying emphasis is on diagnostic methods that are directly applicable to the interaction studies. As a result, it will not be possible to avoid periodic discussions of the interaction experiments, though such occurrences have been minimized and kept brief. Since the coupling mechanisms of interest occur near the critical density, n_c for the incident CO_2 laser light ($n_c = 1 \times 10^{19}$ electrons cm^{-3}) the diagnostics must, in particular, be suited to plasma having an electron density which covers the range above and below n_c. In the course of this presentation, it will become clear that the actual definition of a high density plasma depends a great deal on the particular diagnostic being considered. What may be the limitation of one experiment can be the justification for another. Four separate experiments have been performed: streak and shadowgram photography, Thomson scattering, and holographic interferometry. The remainder of this introduction outlines the subject material of this thesis and previews the experiments to be presented.

Chapter 2 gives a description of the Z-pinch apparatus and reviews established characteristics of the discharge. The plasma temperature and density during the pre and post pinch phases of the discharge have been carefully measured (Houtman, 1977) using spectroscopic methods. However, during peak compression, the plasma emits only continuum radiation and spectroscopy could not be used. In Chapter 3, two relatively simple diagnostics are presented, streak and shadowgram photography, both taking advantage of the high plasma density. The resulting pictures give an important preliminary view of details of the plasma structure and dynamics during all stages of the on-axis collapse. The remainder of this thesis is devoted to detailed measurement of the plasma temperature and density using the methods of Thomson scattering of ruby laser light and holographic interferometry.

Thomson scattering examines the plasma at the microscopic level by looking at fluctuations in the particle density, i.e. plasma waves. Usually, scattering from electron plasma waves is observed. However, Chapter 4 shows that with scattering methods, a high density plasma is most easily investigated by scattering from ion acoustic fluctuations, a technique not often considered as a diagnostic tool. Chapter 5 discusses the arrangement of the scattering geometry and describes the experiment in detail. The geometry has been chosen to serve a two-fold purpose, namely, the measurement of thermal fluctuation levels giving the plasma temperature and density, and, extension of the experiment to examine induced or enhanced fluctuations which are expected to occur with the introduction of the CO_2 laser. The scattering observations and results are presented in Chapter 6. Complications in the technique, arising from the high plasma density, are also pointed out.

At the macroscopic level, holographic interferometry measures the index of refraction, a bulk plasma property that is related in a simple way to the electron density. Some basic principles of this technique are given in Chapter 7, but the main consideration will be for the effects of refraction. The first portion of Chapter 8 describes the generation of short duration diagnostic pulses through cavity dumping of the ruby laser oscillator. This effort advances the diagnostics towards time scales more appropriate to the interaction studies. The remainder of Chapter 8 completes the presentation of the experimental arrangement for interferometry. A few interferograms are shown in Chapter 9 along with the final data. The interferometry has given a full view, both temporally and spatially, of the electron density distribution in the pinched plasma column.

Individually, each of the diagnostic experiments is insufficient to give a complete picture of the high temperature, high density phase of this Z-pinch plasma. Together though, this series of experiments has been well-suited to providing complementary and corroborative measurements of the plasma properties. It has been found that the pinch phase of this discharge produces a plasma which (i) varies in electron density from $n_e \ll 10^{18}$ cm^{-3} to $n_e = 6 \times 10^{19}$ cm^{-3}, (ii) reaches a maximum temperature $T \simeq 50$ eV, and (iii) is contained in a cylindrical volume that ranges in diameter from a few millimeters to less than one millimeter. The plasma parameters do not change significantly on a time scale of a few nanoseconds. The different diagnostic methods agree, in the case of overlap, to typically within 40% while shot-to-shot variations in the experimental data are typically less than 20%. Hence, this thesis shows that the Z-pinch is a very suitable target plasma for CO_2 laser-plasma interaction experiments since the CO_2 laser finds already a fully ionized plasma with well established characteristics.

The final chapter of this thesis presents a brief summary of the important features of both the plasma, and the diagnostic experiments. As well, some consideration will be given to the application of these methods in the interaction studies.

CHAPTER 2 THE Z-PINCH APPARATUS

The Z-pinch discharge used throughout the investigations presented in this report is a constant and major component of the interaction experiments. This chapter is not intended to provide a complete analysis of the Z-pinch, but rather to review established characteristics (Houtman, 1977) and provide a background for the remainder of this work. In order to supplement the following discussions, Table I gives the basic parameters and operating conditions of the discharge while the photograph of Figure 1 shows the apparatus which has been assembled for interaction and diagnostic experiments.

The discharge chamber is constructed in a cylindrically symmetric manner using a pyrex vacuum vessel 10.2 cm inside diameter. Electrodes are made from copper discs of the same diameter and have an axial separation of 35.6 cm. Brass wire mesh is wrapped about the vessel exterior to form a co-axial return conductor. The discharge is formed in a continuously flushed helium atmosphere that is maintained at 1.2 torr pressure.

The energy storage bank consists of six 14 μF capacitors which are charged in parallel to 11.5 kV. Directly atop each capacitor is a spark gap switch. When these so-called 'main gaps' are triggered, the capacitors are discharged in parallel through the Z-pinch. In order to minimize the total inductance of the circuit, the current from each capacitor is transported to the Z-pinch anode through 5, electrically parallel, 16 ohm high voltage transmission cables. There is a total of 30 such cables, all these being of equal length.

The discharge is initiated in the following manner. A 'master' spark gap is used as the common element for seven separate trigger circuits. Six of the circuits are identical and these supply the trigger pulses for the six main spark gaps. The main gaps are triggered simultaneously. The Z-pinch anode receives the seventh trigger pulse, such that, at the same time the main gaps are triggered, a low density glow discharge

TABLE I

BASIC PARAMETERS OF THE Z-PINCH DISCHARGE

Vacuum vessel	pyrex glass, 10.2 cm I.D. 11.4 cm O.D.
Electrode separation	35.6 cm
Filling gas	1.2 torr Helium, 3.9×10^{16} atoms per cm^3 @ 24°C
Capacitor bank	84 μF
Charging voltage	11.5 kV
Ringing frequency	86 kHZ
Available energy	5.6 kJ
Time of maximum compression	1.9 μs
Bank energy remaining @ 1.9 μs	2.7 kJ

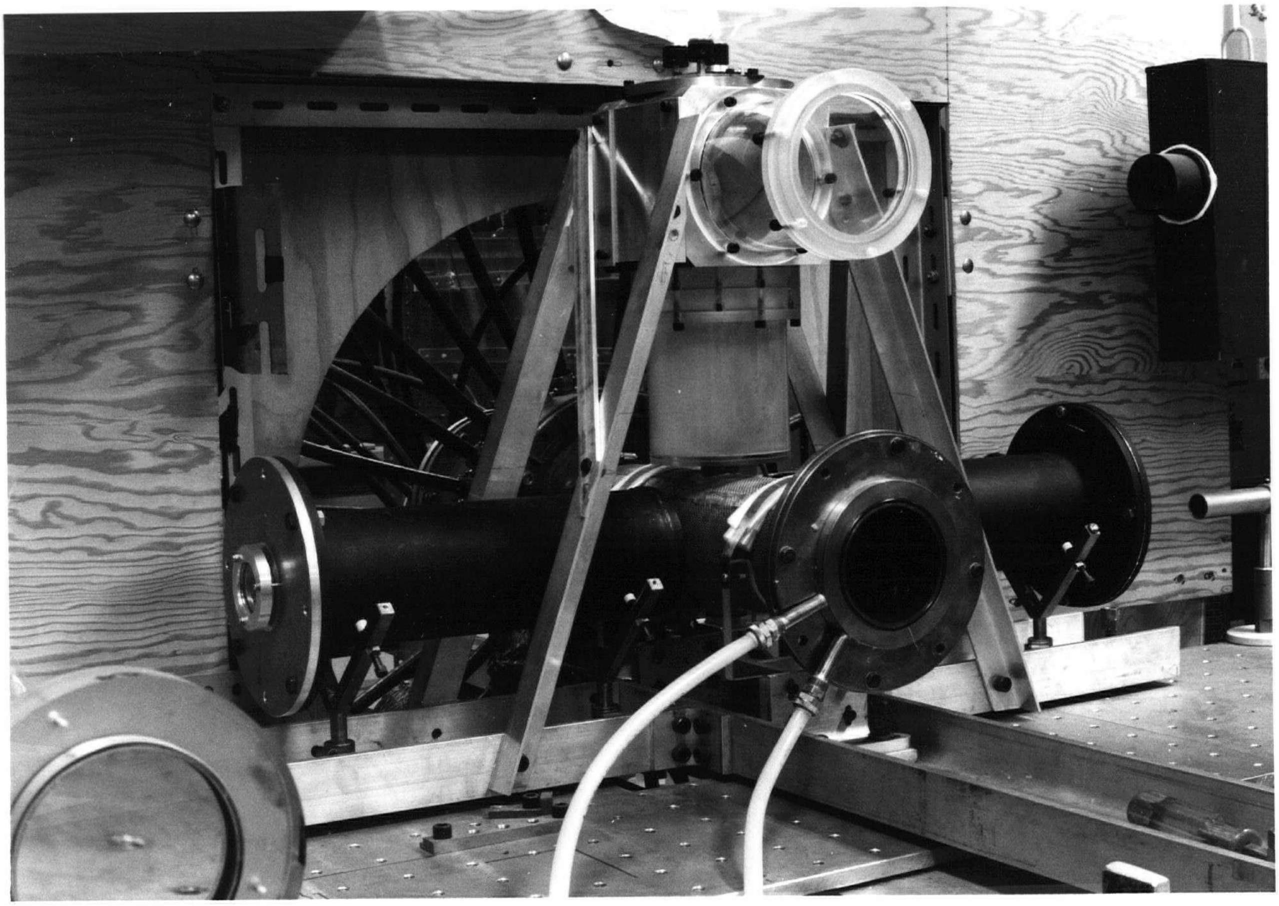

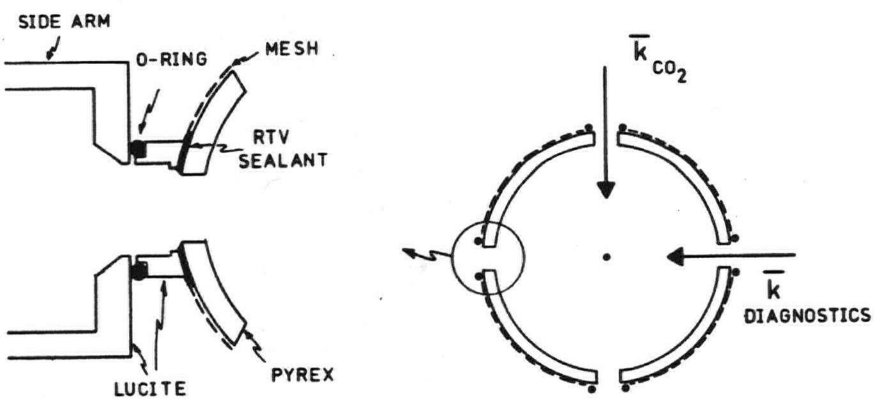

Figure 1

(A) Photograph of the Z-pinch apparatus.
(B) A cross-sectional view of the ports.

fills the chamber. This provides for pulsed pre-ionization of the plasma. Appendix A contains some additional details concerning the trigger circuitry and timing. With pre-ionization, the discharge can be initiated with a jitter of less than 10 ns. The important point to be made here is that pre-ionization of the plasma has been essential for the coordination of plasma and diagnostic events.

All the diagnostic studies of this report have been performed in the radial direction with the cylinder axis oriented horizontally (see Figures 1 and 3). Midway between the electrodes and diagonally opposing one another are two diagnostic ports. These ports were made by drilling holes in both the pyrex vessel and return conductor. Two more identical holes are drilled in the vertical direction for incident and transmitted CO_2 laser light. The CO_2 laser beam is also focused into the plasma in the radial direction, and, like the diagnostic ports, midway between electrodes. In other words, the line-of-sight through the diagnostic ports is a horizontal diagonal of the discharge vessel while the CO_2 laser beam will travel along a vertical diagonal of the vessel. These two diagonals are coplanar.

The holes that were drilled through the vessel and mesh are, respectively, 1.9 cm and 3.7 cm in diameter. The holes in the brass mesh constitute only 10% of the total length of the plasma column whereas four such holes represent about 40% of the circumference of the return conductor. Note here that the access ports will introduce perturbations in the plasma column. Therefore, in the vicinity of these holes, rotational symmetry of the plasma column is not guaranteed.

Two side-arms are horizontally mounted at the diagnostic ports and sealed to the vessel with o-rings (Figures 1 and 3). Windows and lenses, etc., are mounted on the side-arm end plates. The CO_2 laser beam enters the discharge chamber via an L-shaped focussing channel. This channel is mounted on the discharge vessel at the top vertical hole, as shown in Figure 1. A 50 cm focal length salt lens is used as the air-vacuum interface. A copper mirror, mounted inside the vacuum channel, steers the (converging) CO_2 laser beam into the discharge chamber. Optical components are removed from the immediate discharge vicinity and suffer only minor damage due to the deposition of the debris that is generated during the discharge.

The discharge current, I(t) was measured using a small Rogowski coil pick-up located in a region near the anode where magnetic fields due to the discharge current could be sampled. The primary measurement here is a changing magnetic flux inducing a coil current proportional to dI/dt. Passive integration provides direct oscilloscope display of the main discharge current. A sample of the complete current trace and an expanded portion of dI/dt are shown in Figure 2. Also, Figure 2 gives the capacitor voltage $V_c(t)$ as measured at one of the spark gaps. The voltage drop across the plasma column itself was not measured. Therefore, only charge drainage from the capacitor bank was determined.

Passive elements in the discharge circuit control early stages of the rising current pulse. As compression proceeds, the inductance of the plasma column itself increases and begins to dominate the circuit parameters. The reduction or dip in current approximately 2 μs after discharge initiation, occurs at maximum compression. In the expanded dI/dt trace, the current dip, and hence, the maximum compression or pinch phase, can be easily identified. Since this moment of maximum compression is clearly evident in the dI/dt signal, the time at which dI/dt is zero will be used as the time reference for all diagnostics presented in this thesis.

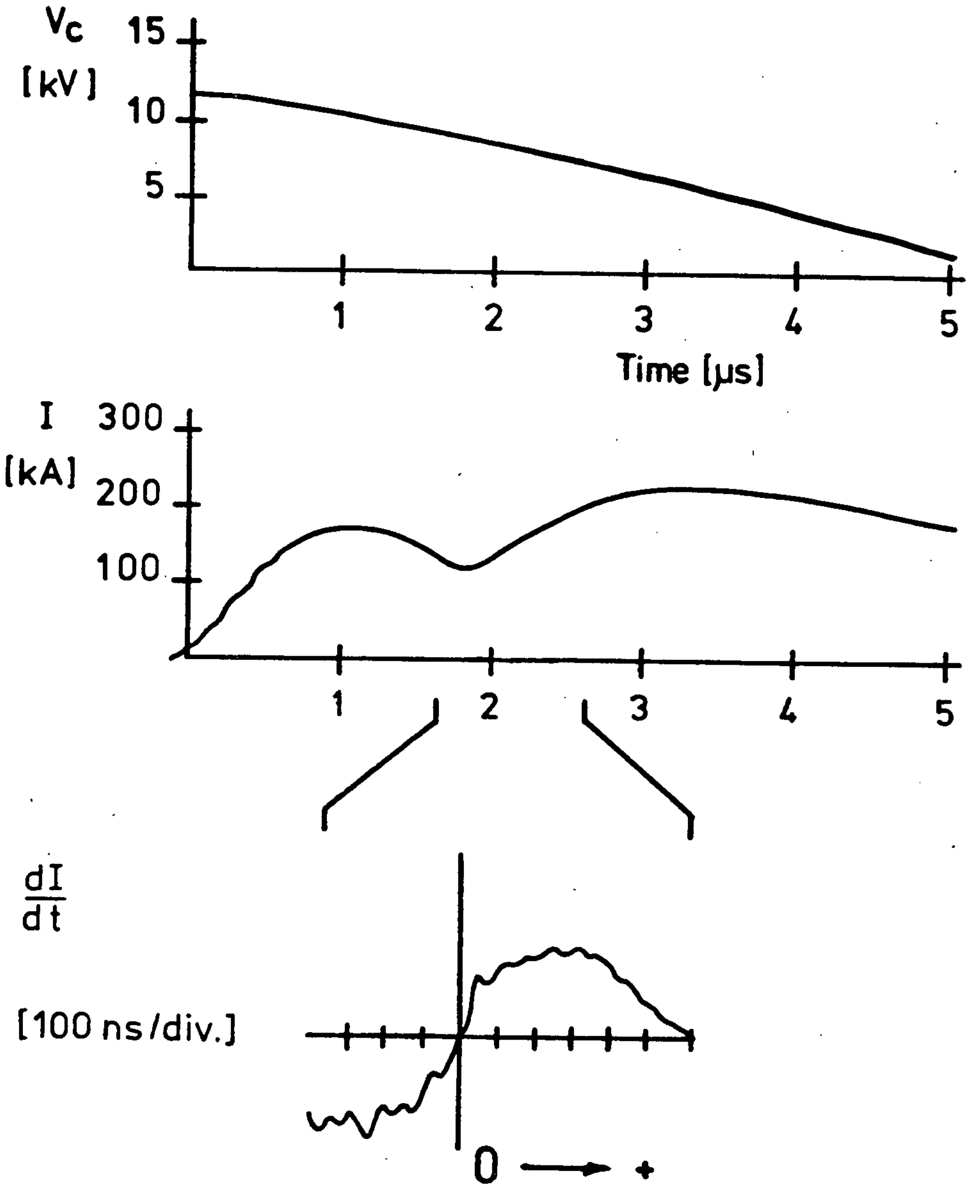

Figure 2

Voltage and current traces for the discharge circuit.

Characterization of the discharge dymanics and plasma conditions began with the measurements of Houtman (1977). The experiments described therin included end-on framing camera studies and electron temperature and density determinations from spectral line broadening measurements. These experiments give a complete and detailed description of the collapse phase, i.e. times prior to the dip in current. Accurate measurement of plasma parameters and radial dynamics during the high compression phase were, unfortunately, not possible. Indications were that the pinched plasma had electron temperatures and densities in the range of 40 eV and 8.0×10^{18} cm^{-3} respectively, with a minimum luminous radius of the order of 5 mm. These estimates represent a starting point for the present work in which it is intended to extend measurements to time and size scales relevant to the pinch phase of the discharge.

CHAPTER 3 STREAK AND SHADOWGRAM PHOTOGRAPHY

3.1 Introduction

The experiments described in this chapter were intended to examine, in as simple a way as possible, basic features of the plasma distribution during the time of maximum on-axis compression. This phase of the pinch has not been investigated with sufficient spatial or temporal resolution to observe details of either the plasma structure or motion. In this respect, the present experiments are a significant improvement and extension of earlier work.

The important parameter determined here is the plasma radius as a function of time, r(t), near the time of maximum compression. Changes in the radius give the velocities v = dr/dt associated with the plasma collapse and subsequent expansion. Because z-pinch plasmas are notoriously unstable to several magnetohydrodynamic perturbations (e.g.: see Artsimovich, 1964), the pinch phase can be expected to terminate in some highly unstable manner. Irregular disruption of the plasma column has been clearly seen in these measurements. This observation establishes the time during which the plasma is sufficiently well behaved to serve as a target plasma for interaction studies.

Two relatively simple techniques are employed, streak and shadowgram photography. Both of these depend on a high plasma density for their application.

The streak photographs give an image of the plasma from self-emitted radiation. Throughout the visible region of the spectrum, a high temperature ionized gas produces electron-ion bremsstrahlung radiation (Zel'dovich, 1966) with an intensity that is only weakly dependent on the plasma temperature. However, because the intensity of the bremsstrahlung radiation depends on the frequency of electron-ion collisions, the plasma emission coefficient will be proportional to the product of the electron and ion number densities, or, simply, $n_e{}^2, n_e$ being the electron density. Intensity variations in the streak photographs will therefore reflect the distribution of electron density.

For the shadow method, the plasma is considered an essentially transparent object with the variation in electron density replaced by its equivalent refractive index distribution. The plasma is then illuminated with a spatially uniform and collimated beam of light. Upon passage through the plasma, portions of the beam are deflected from their original path, the deflection angle being proportional to the gradients in refractive index that must be traversed (Barnard, 1975). Since the incident beam has an initially uniform intensity distribution, those regions of the plasma that are deflecting incident light will show up a reduction in the transmitted beam intensity. In this sense then, a photograph of the transmitted beam represents the plasma's shadow. From a more general point of view, the technique may be termed refraction contrast imaging. The method is of course quite similar to the way in which one can observe small bubbles or imperfections embedded in ordinary window panes.

In keeping with the simplicity of these techniques, only the above brief description of the methods has been given. With these descriptions, the experimental arrangement (Section 3.2) can be shown, and the basic observations pertaining to the size and structure of the pinch phase can be interpreted. Then, it will be worthwhile to give a better indication of how the shadowgram method used here relates to more general refraction contrast imaging techniques. Following this, numerical results are given for the plasma parameters obtained from this photographic study. Section 3.4 uses the streak pictures and a simple snow-plow model of plasma collapse in order to estimate the electron density. Section 3.5 considers the shadowgrams in more detail. In particular, some structure in the shadow images are the result of interference effects produced through the use of a coherent probe beam. Such interference effects have led to a second, independent estimate of the electron density.

It will be seen that the streak and shadow techniques are quite complementary in nature. Each can provide a close look at plasma motion during the pinch phase. As well, they both give an indication of the spatial distribution of electron density. Though the information in this regard is more qualitative in nature, these experiments have given fairly reasonable estimates of the electron density.

3.2 Experimental Method

The experimental arrangement for both techniques can be described with the aid of Figure 3. For shadowgrams, the beam of a Q-switched ruby laser (500 mJ in 20 ns) is passed through a x10 expander and spatial filter combination to produce a collimated beam approximately 8 cm in diameter. Only the central 2 cm portion of the expanded beam is used to illuminate the plasma, thus providing for a strictly uniform intensity distribution in the incident beam. The transmitted beam is observed in a plane which is located some distance beyond the plasma, e.g., in the object plane indicated in Figure 3. The plasma shadow, as it appears in the object plane, is then imaged onto polaroid film using lens L. A cardboard box protects the film from ambient exposure. Direct plasma light is reduced to negligible levels by imaging through a Kodak gelatin filter (#92) which cuts out all light with wavelengths below about 6400 Å. Additionally, gelatin neutral density filters were used to adjust the exposure due to the ruby laser.

In obtaining the shadow pictures, the distance from the plasma axis to the image plane was held fixed. However, the distance from the plasma to the object plane could be varied by changing the position of lens L (Figure 3). By observing the plasma shadow in different object planes,

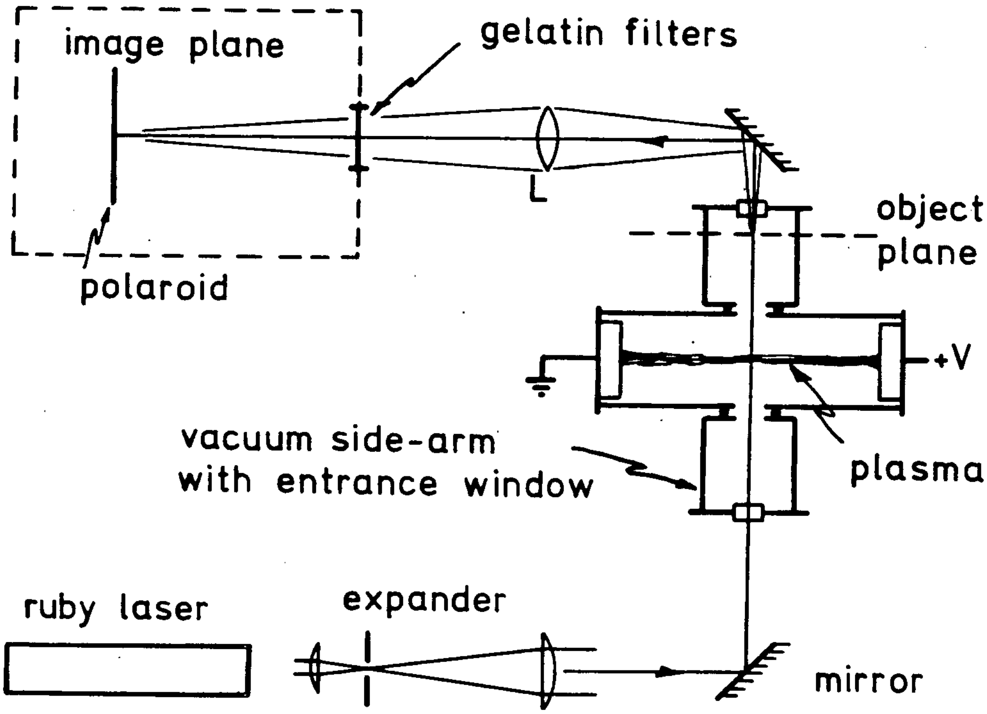

Figure 3

Schematic of the shadowgram experiment. Object planes less than 43 cm from the plasma are contained within the vaccum vessel. The distance from plasma to image plane is approximately 350 cm.

some discrimination can be made between those regions of the plasma that are responsible for either large or small angular deflections. For example, when the object plane is located close to the plasma axis, the incident rays that suffer only small deflections will not have diverged sufficiently to contribute to the image contrast. In this case then, the size of the shadow will reflect the extent of the strongly refracting regions of the plasma. On the other hand, if the shadow is observed in very distant object planes, the weakly refracting regions will also become apparent. Samples of the plasma shadow seen in different object planes will be presented shortly.

Streak photographs have been obtained in a more straight forward manner. Returning to Figure 3, in order to take streak pictures, the ruby laser is not used, gelatin filters are removed, and a 4 mm wide vertical slit replaces the polaroid film. The schematic lens L (now a four element system of imaging and image transport lenses) is arranged to image the plasma axis horizontally across the slit with a total magnification of x7. Plasma light transmitted through the slit is viewed using a TRW model 1D image converter camera. The camera records a streaked image of the plasma on polaroid film. The picture thus obtained gives a radius vs time plot of the plasma self-luminosity.

3.3 Streak and Shadowgram Pictures

This section gives a full view of the pinch phase from photographs obtained with both streak and shadow techniques. The description here is qualitative, but serves to illustrate basic features of the pinch as well as the correspondence between the two methods. Section 3.4 gives measurements of the plasma diameter and shows that this correspondence can be quite good.

Figure 4 presents a composite of the observed streak photographs. Each of the three frames shown were obtained from separate firings of the discharge. Between shots, the exposure window of the streak camera was translated with respect to the pinch time. As a reminder, the time axis is referenced to the zero-crossing of dI/dt, as indicated in Figure 2, so that $dI/dt = 0$ at time $t = 0$. The bright vertical line at the beginning of each frame is an overexposed image of the slit. (This image results from a 'hesitation' in the ramp voltage that is applied to the deflection plates of the image converter tube.) Based on the slit image, it is easy to determine that the temporal resolution is approximately 5 ns.

At early times $t < -100$ ns a diffuse and weakly luminous plasma shell can be seen moving radially inwards. Incoming plasma converging on axis is compressed, and the bremsstrahlung emission increases significantly, beginning at about $t = -80$ ns. The on-axis plasma therefore has a much higher density than the surrounding shell. The high intensity (i.e. high density) region continuously grows in diameter as plasma accumulates on axis. Later than approximately $t = +100$ ns, the clarity and symmetry of the plasma boundary deteriorates. This is presumed to correspond to a disruption of the plasma column due to instabilities.

The features of the pinch phase mentioned above, namely, (i) an early time, incoming shell, (ii) a high density plasma core on axis, surrounded by a low density region, and, (iii) break-up of the plasma column, can also be clearly seen in the shadowgram pictures.

Figure 5 presents a sampling of some typical shadowgram pictures that were recorded. The circle of exposure is a projection of the pinch vessel holes. These holes have a diameter of 1.9 cm and serve as a reference for image magnification. Also in Figure 5, the Z-axis of the discharge chamber is shown. Now, the plasma can be viewed in both the radial and axial directions, and, in all the pictures of Figure 5, the plasma appears well aligned on the geometrical axis of the discharge vessel.

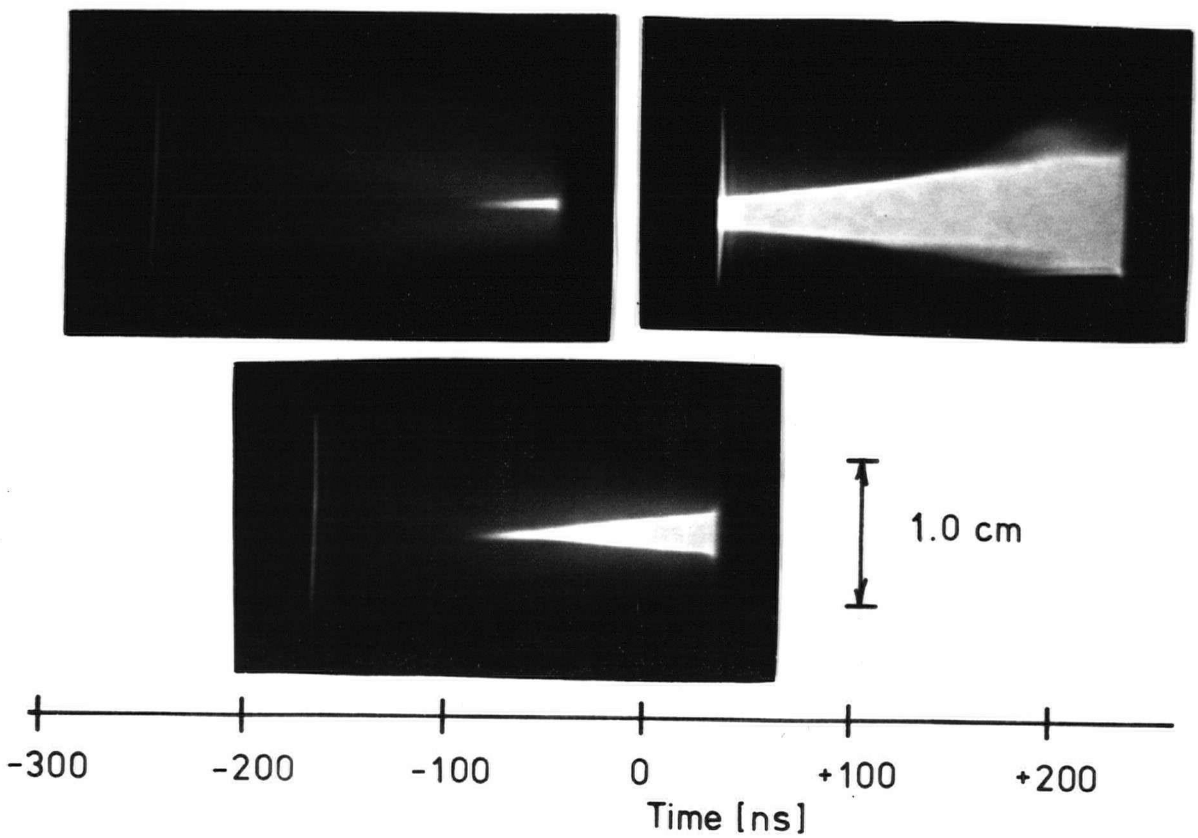

<u>Figure 4</u>

Streak photographs of the pinch phase. Each frame spans a 200 ns time interval.

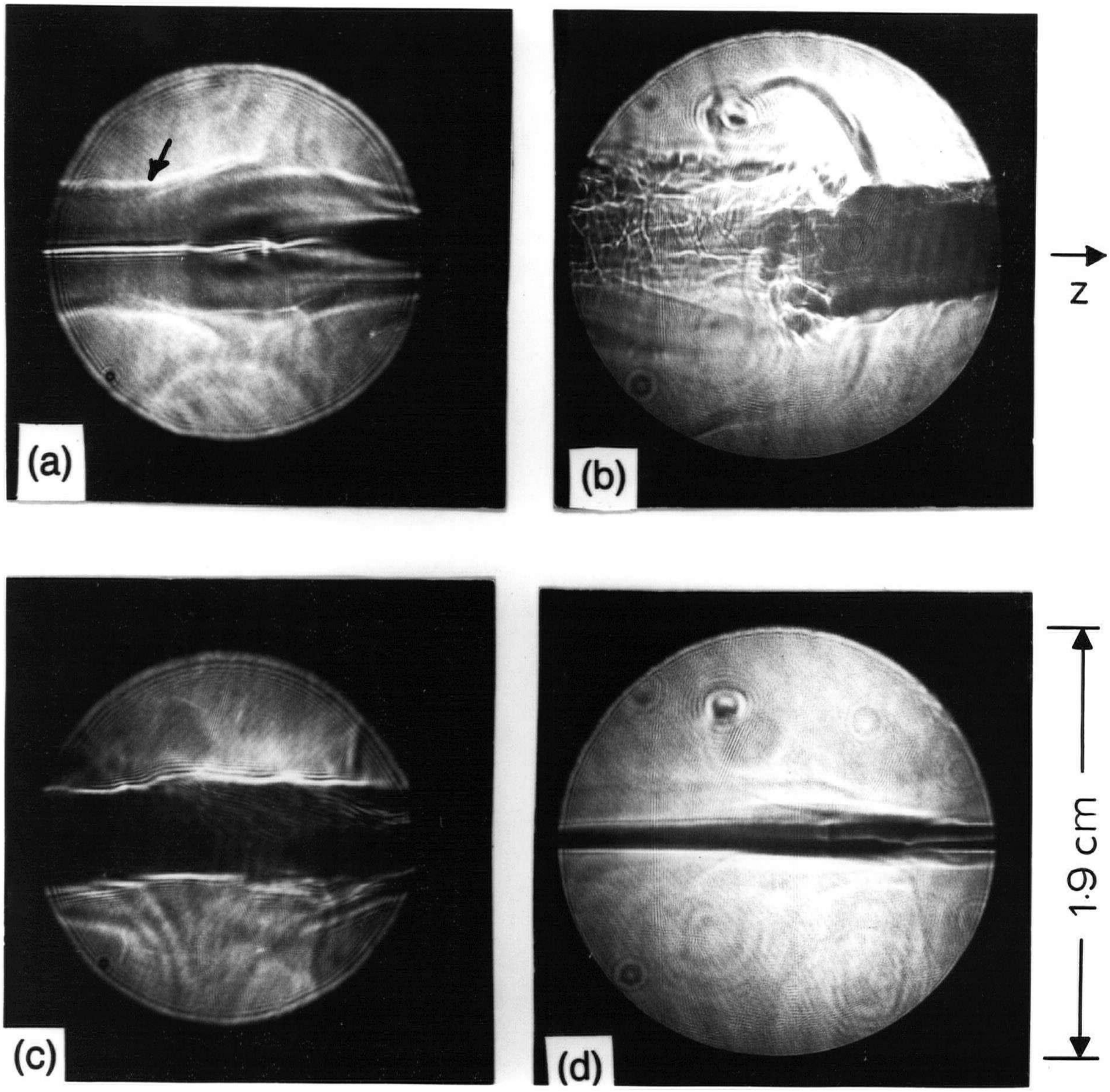

Figure 5

Shadowgram pictures. The exposure time and distance from plasma to object plane are: (A) -70 ns, 32 cm; (B) +110 ns, 7 cm; (C) -20 ns, 32 cm; and (D) -30 ns, 7 cm. The outer boundary of the plasma is, for example, indicated by the arrow in picture (A).

The exposure of Figure 5(A) was taken at time t = -70 ns, just as the incoming plasma reaches the axis (see Figure 4). Since the plasma is only weakly refracting at these times, a large plasma to object plane distance of 32 cm was used in order to obtain good contrast in the image structure. While testing the optics, various index of refraction distributions were photographed, including a glass rod or tube, a gas stream, etc. The bright on-axis exposure of Figure 5(A) is indicative of an object whose refractive index decreases with increasing radius. Consequently, the on-axis plasma must have a lower electron density than the immediate surroundings. As well, the outermost boundary of the refracting region can be seen. Figure 5(A) therefore does confirm that incoming plasma has a diffuse though definite shell structure.

Late times are shown in a somewhat lucky photograph, Figure 5(B). The exposure was taken at t = +110 ns and the object plane is 7 cm off axis. This photograph distinguishes quite dramatically between the plasma structure before and after the pinch column has broken up.

Development of the high density plasma core is illustrated in the shadowgrams of Figures 5(C) and (D). These pictures were taken at almost identical times (t = -20 ns and -30 ns respectively), though in different object planes (32 cm and 7 cm respectively). The dark column of Figure 5(D) is produced by rays deflected from the central dense plasma core. Small ray deflections become apparent in a much more distant object plane, Figure 5(C) where the shadow diameter corresponds in size to the surrounding low density plasma.

Having had a look at the plasma shadow in off-axis image planes, it is worthwhile here to indicate how the pictures appear when the plasma axis itself is imaged. Doing this will lead to a basic distinction between the shadow method used here and the usual, and possibly more familiar technique of Schlieren photography. However, the following discussion does not presume to replace the expert analysis of the subtleties of refraction contrast imaging, i.e.: Holder, 1963.

If the plasma axis and object plane are coincident (see Figure 3 or 6(A)), the shadowgrams show a noticeable though very weak variation in exposure due to rays missing the first collection lens. This lens views the pinch axis with an F/# of 14 implying a maximum deflection angle of 2.2°. When imaging the plasma axis, exposure variations occur mainly within 50 ns of maximum compression and appear just inside the boundary of the high density core where density gradients, and hence ray deflections, are largest.

Now, when plasma is not present, the photographs of Figure 5 would of course be uniformly exposed for all object planes since the incident illumination is uniform. If plasma is present, and the object plane coincides with the plasma axis, the film would again be uniformly exposed. This latter case requires that two conditions be fulfilled. (i) The imaging optics must have a sufficiently small F/# to collect all refracted light, and, (ii) the refracted rays do not diverge appreciably within distances comparable to the plasma radius. Figure 6 and the following discussion will help to illustrate the difference between conditions (i) and (ii).

When condition (i) only is not satisfied, exposure variations are due primarily to vignetting by some aperture in the imaging system. Figure 6(A) shows such a situation where all rays deflected by more than some minimum angle are lost at the imaging lens This corresponds to Schlieren photography where the object itself is imaged and limited F/# viewing replaces the role of a knife edge or grid, etc., in eliminating specific angular deflections. In turn, the deflection angles are determined by the refractive index gradients that are traversed. Therefore, Schlieren systems are sensitive to $\nabla\mu$, μ being the refractive index.

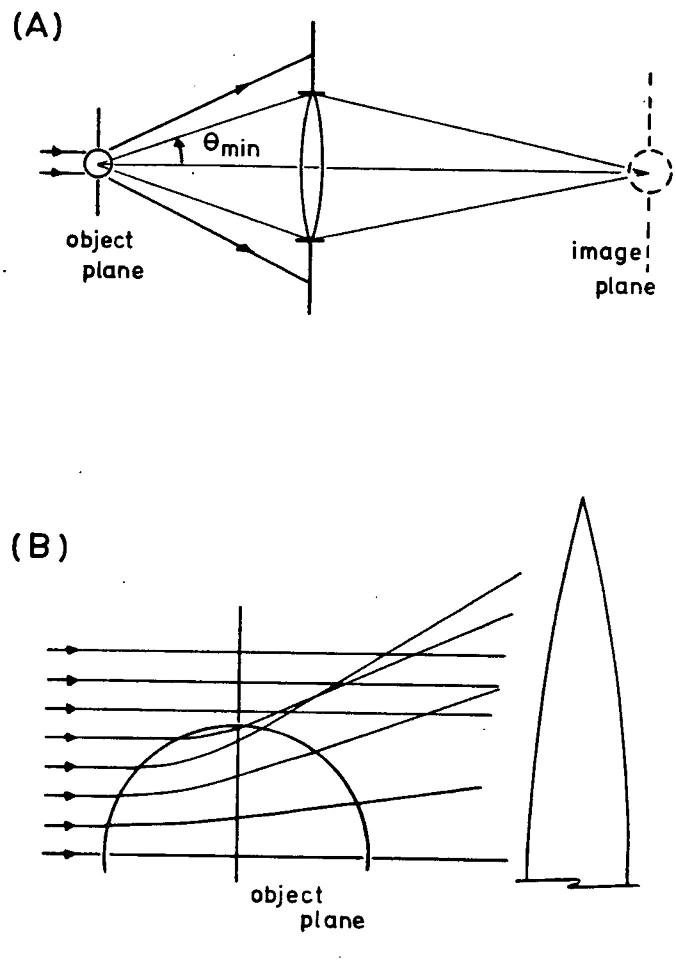

Figure 6

Formation of contrast in on-axis images. Refracted rays can be (A) vignetted and/or (B) divergent.

In contrast, when all refracted light is collected, but condition (ii) above is not satisfied, then exposure variations will occur when refraction produces a local spreading or divergence of the incident light. Figure 6(B) depicts a uniform intensity incident beam as a set of equally spaced ray paths. In the object plane, the rays are clearly not equally spaced. In this case then, a non-uniform deflection angle, that is, $\nabla^2\mu$ determines the image structure.

The shadow method is not restricted to image planes containing the refracting object. In fact, the object (plasma) boundaries are more well defined in the shadow when off-axis planes are imaged. The shadow (as opposed to Schlieren) method has been appropriate here since it was intended to establish the plasma dimensions during the pinch phase.

3.4 The Plasma Diameter vs Time

In order to quantify the observations of this photographic study, two plots of the plasma diameter D(t) are given in this section. The streak and shadowgram pictures have been analyzed separately. Comparison of the results will show the close correspondence between the information obtained with either technique. As well, based on these plots, a simple estimate of the electron density at maximum compression is given.

Figure 7(A) gives the data obtained from eight streak frames. The diameter of the high density core, denoted by crosses, was clearly marked in the photographs. The outer boundary of the shell, shown as dots, was not so well defined and was estimated to be just at the outer edges of the weakly luminous regions. Velocities associated with the shell and core were determined for each frame, independent of the diameter measurements since measurement of the speed will not depend on locating the boundaries precisely. The solid lines in Figure 7 have slopes given by:

$$dD/dt\ (\text{shell}) = -1.97 \pm 0.27 \times 10^6\ \text{cm s}^{-1}$$

$$dD/dt\ (\text{core}) = +2.14 \pm 0.11 \times 10^6\ \text{cm s}^{-1}$$

and were positioned on the plot to give the best visual fit to the data points.

Measurements made on approximately thirty shadowgrams resulted in the plot of Figure 7(B). As indicated previously (see Figures 5(C) and 5(D)), shadow pictures taken with the image plane 7 cm off-axis isolate the highly refracting core while pictures in the 32 cm plane delineate the region occupied by low density plasma. Diameters are taken to be the (radial) extent of the unexposed regions, though, since the diameter is slightly z-dependent, some visual averaging was done. Because of this averaging, the core and shell diameters are estimated to be uncertain to $\pm$ 0.3 mm and $\pm$ 0.5 mm respectively.

Comparison of these two plots is to be made on the basis of the solid lines. Those drawn on Figure 7(A) have been transferred exactly, in position and slope, to Figure 7(B). The lines were determined from the streak measurements only, but are judged to fit both sets of data equally well.

Given the size of the plasma, the electron density can be estimated using a 'snow-plow' model of the z-pinch (Leontovich, 1957). One assumption of this model is that all gas contained within the discharge vessel is swept-up and confined to a cylinder having a radius r which decreases as constriction proceeds. The plasma density therefore increases in direct proportion to the volumetric compression ratio. This assumption is quite good and has often been used as a cross-check for other density diagnostics.

With total sweep-up, the maximum density achieved will occur when the plasma radius is minimum. Figure 7 indicates that the minimum radius

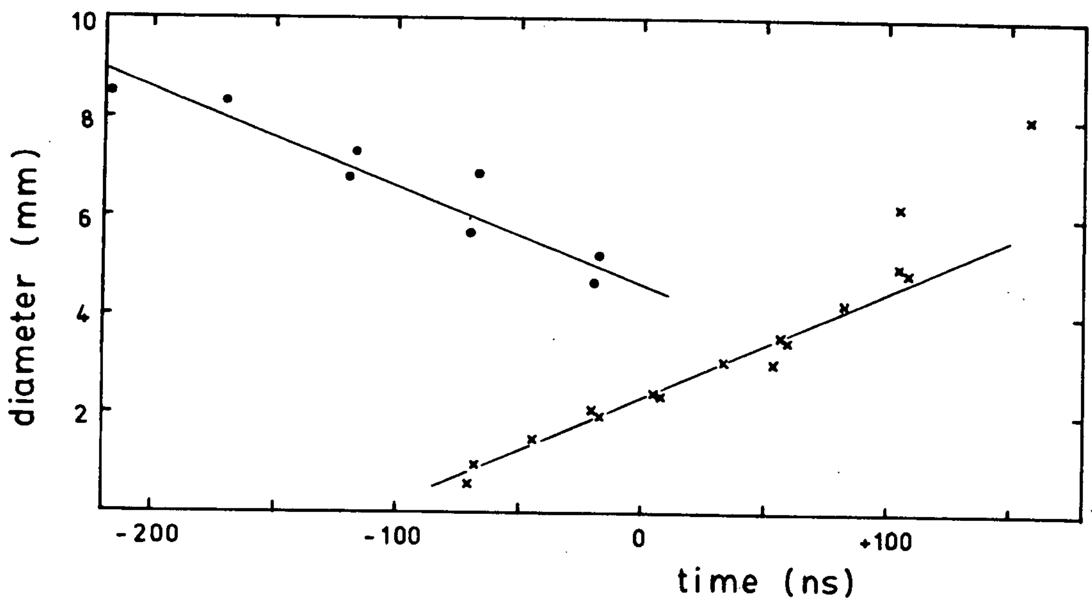

Figure 7(A)

Plasma diameter vs time from streak photographs.

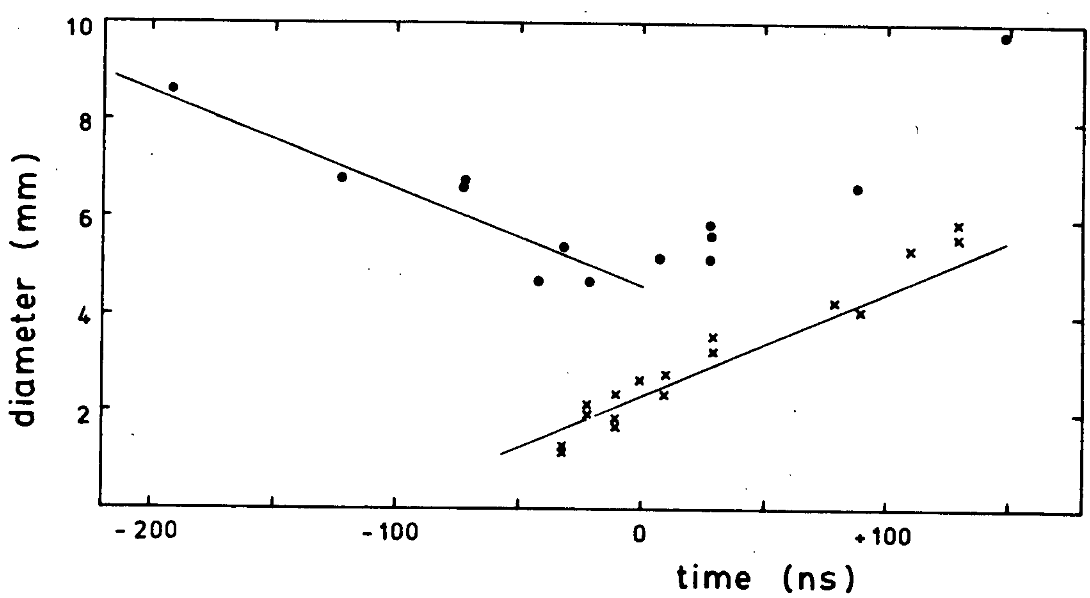

Figure 7(B)

Shadowgram results for the plasma diameter.

r_m is, at most, approximately 2.5 mm. The distribution of plasma for $r < r_m$ will be assumed uniform. If the average ionization is Z, then the electron density is given simply by

$$n_e = Zn_o(R/r_m)^2. \qquad [1]$$

The initial conditions prior to firing the discharge are the inner radius of the vessel, R = 5.08 cm and fill density $n_o = 3.90 \times 10^{16}$ helium atoms per cm^3 (see Table I). At the minimum radius, ionization is assumed complete, so Z = 2. With these numbers, equation [1] predicts an average electron density of:

$$n_e = 3.2 \times 10^{19}\ cm^{-3}$$

at r_m. This density is considerably higher than the original estimates of Houtman, but the minimum plasma radius was not well established at that time.

The high density predicted by equation [1] is fully supported in the next section where electron density estimates are made by an entirely different method.

3.5 Electron Density from Ray Refraction

Here, the shadowgrams are re-examined through an analysis of ray deflections. The result will be an estimate for the electron densities in both the core plasma and surrounding low density region. First though, in order to define the quantities that need to be determined from the shadow pictures, ray bending in a cylindrically symmetric refractive index distribution is considered.

The electron density distribution in the plasma is assumed to depend only on the radial coordinate r and is replaced everywhere by its equivalent refractive index:

$$\mu(r) = (1 - n_e/n_c)^{1/2}. \qquad [2]$$

The refractive index depends on the wavelength of the probe beam through n_c, the critical or cut-off density. At ruby laser wavelengths $n_c = 2.3 \times 10^{21}\ cm^{-3}$. The plasma is confined to be within a cylinder of radius r_o, outside of which, $\mu = \mu_o = 1$.

The probe beam is collimated and travels parallel to the x-axis. Figure 8 depicts the path of one ray, incident on the plasma at height y. In cylindrical coordinates, the ray trajectory will be governed by Bouguer's formula (Born, 1975)

$$\frac{dr}{d\theta} = \frac{r}{\rho}(\mu^2 r^2 - \rho^2)^{\frac{1}{2}} , \qquad [3]$$

where the so-called impact parameter is $\rho = \mu_o y = y$.

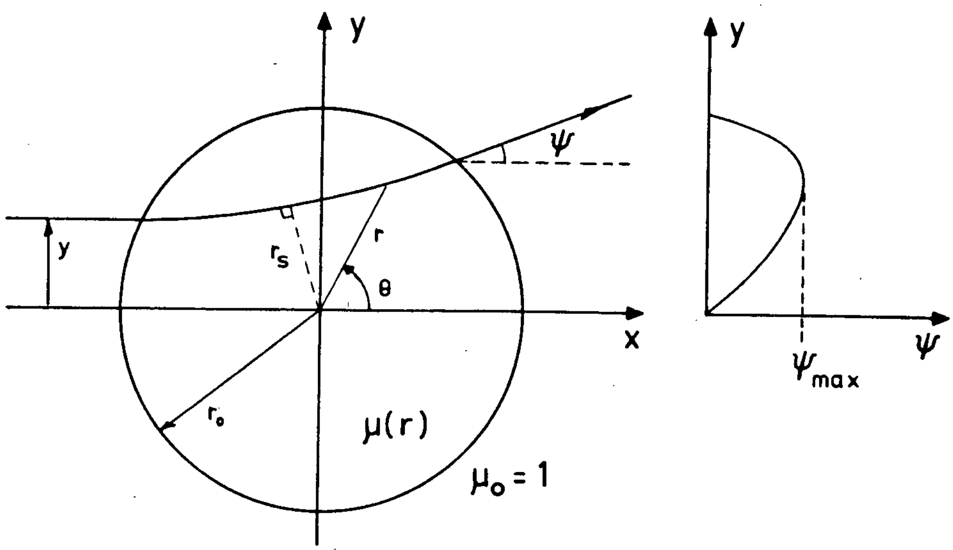

Figure 8

Ray path in an axisymmetric plasma.

When $r > r_o$, the ray will travel a straight line path since the refractive index is constant. Within the object (plasma) the ray will be deflected from its original path. If n_e decreases with increasing r, then the path will be as indicated in Figure 8. Upon exiting the plasma, the ray will have suffered a net angular deviation ψ. Using equation [3], it is easy to see that:

$$\psi(y) = \pi - 2\int_{r_s}^{\infty} (d\theta/dr)dr \ , \qquad [4]$$

where r_s is the stationary point, determined from Bouger's formula as the radius for which dr/dt = 0. Parenthetically, it should be noted that equation [3] should begin with a +/- sign to clarify the fact that $dr/d\theta$ changes sign at r_s. The quantity that can be directly measured with shadow or Schlieren methods is the angular deflection determined by equation [4].

Given an object with a specified refractive index distribution, enables one to calculate a deflection curve $\psi(y)$ that will characterize the distribution. Conversely, by knowing $\psi(y)$, $\mu(r)$ can be found. Completely specifying $\mu(r)$ requires that the impact parameter(s) y corresponding to each value of ψ be measured. Experimentally, this demands a considerably more sophisticated arrangement (e.g.: Kogelschatz, 1972) than the current shadowgram experiments. However, the shadow pictures available have allowed extraction of a useful, though somewhat crude deflection curve.

The important information to be obtained from the deflection curve is the maximum deviation angle ψ_{max} as shown in the curve of Figure 8.

Shmoys (1961) and Keilmann (1972) have performed detailed calculations of $\psi(y)$ using a variety of functional forms for the plasma distribution $n_e(r)$. The functions chosen for $n_e(r)$ are all well behaved. The density is maximum on axis and decays monotonically to zero at r_o. There were no sharp discontinuities in either $n_e(r)$ or dn_e/dr. All of their deflection curves, though different in detail, could be approximated by a single curve, the form of which is indicated in Figure 8. The results of Shmoys and Keilmann's calculations are that, to within an uncertainty of about 35%,

$$\psi_{max} = 1.0\ n_e(r{=}0)/n_c\ . \tag{5}$$

Equation [5] will be used to obtain the desired electron density estimates. The following considerations illustrate how the shadowgrams were analyzed.

Certainly some bounds can be put on the deflection angle just from a knowledge of the shadow radius in a given object plane. For example, at about t = +30 ns, the high density core has a shadow radius of 1.6 mm in an object plane 7 cm from the plasma. Therefore, it should be safe to say that the maximum deflection angle is at least 23 mrad and occurs for an impact parameter no greater than 1.6 mm. Similarly, observations in both the 7 cm and 32 cm plane place bounds on the deflection angle for rays passing through the low density shell region.

A second way used to obtain deflection angle data depends on the fact that the probe beam is coherent. Returning to the shadow photographs themselves, particularly Figure 5(C), it is clear that the image structure near the plasma boundary is dominated by a number of well defined fringes. These fringes result from the interference between undeviated rays passing outside the plasma boundary, and refracted rays which pass thorugh the edges of the plasma. Notice also that the fringe spacing decreases with increasing distance from the axis indicating that the refracted rays are being deflected by uniformly increasing angles.

Given, as in Figure 8, the typical form of a deflection curve, the above interpretation of fringes is considered substantially correct. In order to obtain data points for the deflection curve, the distance d between adjacent interference minima is measured. This gives the deflection angle:

$$\psi = \sin^{-1}(\lambda/d) \simeq \lambda/d$$

associated with the ray producing a particular fringe. Referring to the coordinate system of Figure 8, the object plane will be located at a distance x = l from the plasma. In the object plane, the fringe appears at height y'. With this (measured) information, extrapolation back to the y-axis gives the impact parameter:

$$y = y'(1-l\psi)$$

of the ray deflected by ψ.

Using the above arguments, shadowgrams taken at t = +30 ns were analyzed. The time chosen for this exercise corresponds to the minimum radius of collapse. The resulting deflection curve is shown in Figure 9. The data points were determined by fringe analysis of shadowgrams recorded in object planes 32 cm (circles) and 7 cm (squares) from the plasma. The maximum deflection angle for the core and shell components of the plasma should be contained respectively within the upper and lower rectangular regions. These bounds were determined simply from the shadow diameters in the two object planes.

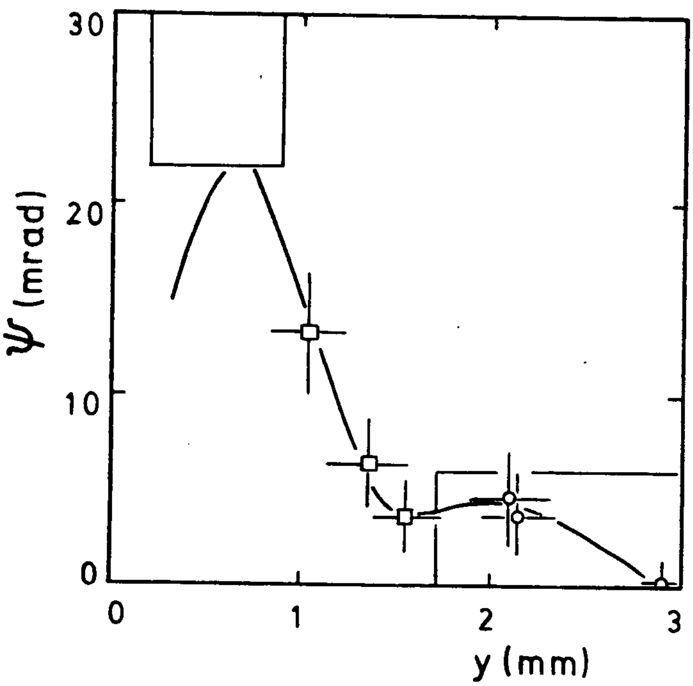

Figure 9

Deflection curve for the plasma at maximum compression.

Because the data is rather sketchy, critical examination of the shape of the deflection curve would be unjustified. The solid line in Figure 9 has been included only to represent a plausible fit to the data.

Since it is clear that the pinched plasma has a definite two component structure, it is not hard to imagine that Figure 9 can be composed by the superposition of two similar deflection curves, each scaling differently in radius and height. Both curves, and therefore both components of the plasma, can be characterized by equation [5]. Taking ψ_{max} for the shell and core plasmas as 5 mrad and 25 mrad respectively, and n_c for ruby laser light, gives:

$$n_e \text{ (shell)} = 1.1 \times 10^{19} \text{ cm}^{-3}$$

$$n_e \text{ (core)} = 6.0 \times 10^{19} \text{ cm}^{-3}$$

Even with the pessimistic view of an uncertainty of a factor of two, these figures agree well with the average density estimated from equation [1], based on a snow plow model of plasma compression.

3.6 Conclusion to the Photographic Study

The experiments that have been presented in this chapter were intended to give a closer view of the plasma pinch phase than had previously been obtained by Houtman. This has been done using photographic techniques that have been (i) relatively simple to implement, (ii) particularly applicable to plasmas of high electron density, and (iii) capable of providing adequate spatial and temporal resolution.

Primary aspects of the plasma dynamics and evolution of the electron density structure have been determined by measuring the plasma diameter as a function of time. Estimates for the electron density during maximum compression have been made with reasonable accuracy. The peak plasma densities achieved are well in excess of the critical density for CO_2 laser light, namely, 1.0×10^{19} cm^{-3}. In this respect then, the pinch phase is quite suitable for laser-plasma interaction experiments. Qualitatively, the density structure during collapse is smooth and well behaved for approximately 200 ns, after which, the pinched column breaks up in an irregular and unpredictable manner.

This concludes the initial observations of the pinch phase. The photographic study represents an important extension of earlier work and will prove vital to the interpretation of subsequent experiments. The following few chapters constitute the second portion of this work, namely, accurate determination of the plasma density and temperature during the pinch phase using Thomson scattering of ruby laser light.

CHAPTER 4 ELEMENTS OF THOMSON SCATTERING

4.1 Introduction

Thomson scattering by plasma fluctuations is a very common method for measuring temperature and density. Several good reviews of the subject have been published (Kunze, 1968; Evans, 1969; DeSilva, 1970) and these give a complete description of the theory and techniques of Thomson scattering. The analysis presented in these reviews has remained relatively unchanged to the present time. This chapter will not attempt detailed derivations pertaining to the theory of electromagnetic wave scattering in plasmas. However, results of the theory will be used to define the basic aspects and parameters of Thomson scattering that are important for the current Z-pinch diagnostics.

In plasmas, the Coulomb forces acting between particles allow for a wide variety of wave phenomenon. As a consequence, the frequency or wavelength spectrum of light scattered from plasma particle fluctuations is rich in structure and detail. Although only scattering from electrons is significant, strong Coulomb coupling between electrons and ions can result in scattering which is dominated by, and characteristic of, the ion distribution.

The first section of this chapter discusses the distinction between the so-called electron and ion features of the spectrum of scattered light. Separation of the total spectrum into two distinct components stems from the two basic types of fluctuations that occur in plasmas, namely, electron plasma waves and ion acoustic waves. The usual Thomson scattering method examines the electron feature. However, in the experiments to be presented, only the ion component of the spectrum is observed. Application of Thomson scattering to the current investigation is therefore, quite unconventional in the sense that details of the ion feature are not normally observed or even considered for routine diagnostic purposes.

The second portion of this chapter will demonstrate that the ion feature is particularly useful for determining plasma parameters in moderately hot, dense environments such as the current Z-pinch plasma. This conclusion will result from a comparison of the relative spectral brightness of electron and ion features. The emphasis will be on the ability to detect scattered light over and above the level of plasma bremsstrahlung emmission. Background light levels will increase with n_e^2 whereas the intensity of scattered light increases only linearly with n_e. At plasma densities where the electron feature is completely masked in background light, the ion feature may be easily detectable, and therefore represent an important extension of the usefulness of Thomson scattering diagnostics.

4.2 Distinction Between Electron and Ion Features

The spectral distribution, that is, the intensity vs frequency dependence of light scattered from a plasma is given by the so-called shape factor $S(k, \omega)$. This function is defined through the differential cross-section per unit volume:

$$\frac{d^2\sigma}{d\omega d\Omega} = n_e \sigma_e S(k,\omega) \ .$$

Here, n_e is the average electron density. The scattering properties of a single electron are contained in the Thomson cross-section, σ_e . Though not explicitly shown, σ_e also contains the usual angular dependence of electric dipole radiation. (By virtue of its much larger mass, scattering from ions is neglected). The scattering properties of the whole system of interacting particles is described by $S(k,\omega)$. Conservation of momentum determines the wavevector $\bar{k} = \bar{k}_o - \bar{k}_s$, with $\bar{k}_o$ and $\bar{k}_s$ being the wavevectors for incident and scattered light respectively. Wavevector $\bar{k}$ selects the spatial component of density fluctuations which contribute to the scattered signal of the frequencies $\omega = \pm |\omega_o - \omega_s|$ (conservation of energy).

The complete frequency and wavevector dependence of the scattering cross-section for plasmas has been calculated in detail by several authors, (e.g. Salpeter, 1960; Salpeter, 1963 or Rosenbluth, 1962). Salpeter (1960) has shown that the shape factor $S(k,\omega)$ may be written as the sum of two separate components,

$$S(k,\omega) = S_e(k,\omega) + S_i(k,\omega) \ , \qquad [6]$$

where the subscripts refer to the electron and ion features of the profile. This separation emphasizes the two different types of plasma waves that may be investigated by scattering techniques. The following description will isolate the basic difference between electrons which scatter into these two components of the spectrum, namely, the apparent electron inertia.

The electron feature results from scattering off electron Langmuir waves. These are longitudinal, electrostatic fluctuations in the density of electrons only. Perturbations in the electron density which produce a charge separation will set-up an electric field $\overline{\delta E}$ and this field provides the restoring force for oscillation. Electrons of course, can respond very rapidly to $\overline{\delta E}$ compared with the relatively massive ions. Ions can therefore be considered immobile and the electron motion is completely decoupled from the background of positive ions (except in so far as the ions ensure electrical neutrality over the plasma volume). Consequently, electron Langmuir fluctuations are of the high frequency type and the electron feature cannot be expected to give information on the ion motions.

The ion feature is the result of scattering from electrons which are tied (via Coulomb forces) to the ion motions. The inertia of these electrons will now be determined by the ion mass so that characteristic frequencies in the ion feature are much lower than those for the electron feature.

Ion acoustic fluctuations, though analogous to the more familiar low frequency sound waves, are also electrostatic oscillations (Chen, 1974). In response to perturbations in the ion density, electrons attempt to preserve local electrical neutrality by moving together with the ions. However, not all electrons contribute to neutralizing the electric fields produced by the ion disturbance. It is the residual electric field that maintains the ion oscillation. The magnitude of the residual field depends on the number of high energy electrons which do not participate in shielding, and, this in turn is determined by the distribution of electron velocities. Therefore, a full description of the ion feature will contain parameters of both electron and ion distributions.

The basis of equation [6] for separating the spectrum of scattered light into electron and ion features is, of course, the large disparity in frequency scales which results from the difference in the electron's apparent inertia. In a simple view of the electron term, the electrons can be considered uncorrelated. (Clearly, this is not the general case since correlations are required for the existence of plasma waves. The conditions under which correlation effects can be ignored will be presented shortly, when the spectra are described in more detail). If the electrons are also randomly distributed in space, the electron density will have spatial fluctuations that are statistically independent. Then, the scattered intensity, at a given frequency shift, will be proportional to the number of electrons that have a velocity corresponding to this Doppler shifted frequency. If the electron velocities are described by a Maxwellian distribution, the scattered spectrum will just be a Gaussian profile with a width determined by the mean thermal speed of electrons. In a very similar way, the ions can be considered to behave independently of one another. Those electrons that closely follow the ion motions will produce a scattered spectrum that reflects the velocity distribution of the ions.

Based on the simple description above, it is easy to see that the electron and ion features will have spectral widths determined by the respective electron and ion thermal velocities. The width of the electron feature will therefore be larger than that of the ion component by a factor of the order of:

$$v_e/v_i = (m_i/m_e)^{\frac{1}{2}} \ . \qquad [7]$$

For example, $v_e/v_i = 86$ in a fully ionized equilibrium helium plasma. Such a large discrepency in frequency scaling has serious consequences in terms of experimental application. This will be discussed further in Section 4.3.

The simple estimate above precludes the possibility of density fluctuations that are produced by the collective excitation of plasma waves. Nonetheless, in spite of such complications, equation [7] remains a very reasonable representation of both the source and magnitude of the relative widths of electron and ion features.

Figure 10 shows what a more typical scattered spectrum might look like. Certainly this spectrum cannot be described by a Gaussian. The appearance of resonant structure is quite evident. The remainder of this

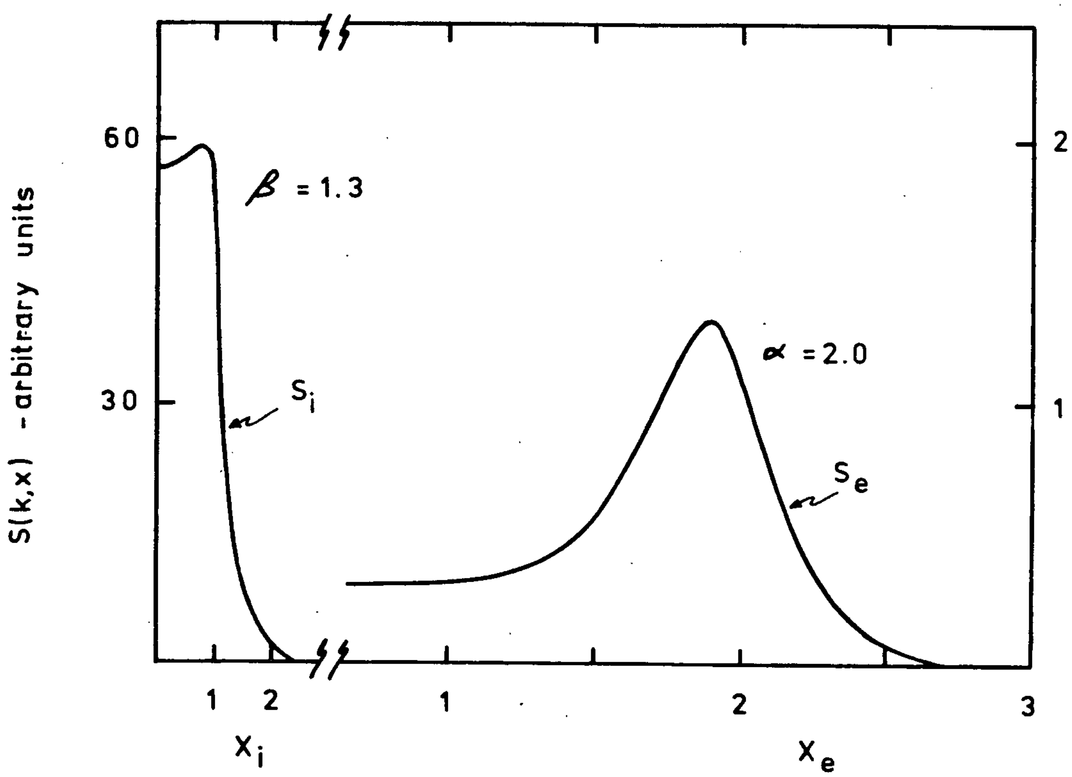

FIGURE 10

A 'typical' scattered spectrum. Frequency scales are normalized to either the electron or ion thermal velocities, $x = \omega/kv_{th}$. Note the relative intensity scales.

section will discuss this 'typical' spectrum in detail. In order to initiate this discussion, the fraction of the total amount of scattered light that will appear in either the electron or ion feature will be written down. The distribution of scattered light is determined by the frequency integrated shape factors (Evans, 1969)

$$S_e(k) = \int_{-\infty}^{\infty} S_e(k,\omega)d\omega = (1+\alpha^2)^{-1}$$

$$S_i(k) = \frac{Z\alpha^4}{(1+\alpha^2)[1+\alpha^2(1+ZT_e/T_i)]} \qquad [8]$$

These are calculated assuming the electron and ion distributions are Maxwellian, but at different temperatures. The degree of ionization is Z.

The most important parameter here, which determines the type of scattered spectrum observed is the correlation or scattering parameter,

$$\alpha = (k\lambda_D)^{-1} \qquad [9]$$

This is the ratio of two characteristic lengths. The density fluctuation which scatters incident light has a wavelength $\lambda = 2\pi/k$ and this determines the distance over which particle correlations will be investigated. In turn, λ is determined entirely by the experimenter through choice of the wavelength of incident light, and arrangement of the scattering geometry. The Debye shielding length for electrons,

$$\lambda_D = (\varepsilon_o \kappa T_e/e^2 n_e)^{\frac{1}{2}} \qquad \text{(mks)}$$

is fixed by the plasma conditions, i.e. the electron temperature T_e, and density n_e. The Debye length represents the distance over which a local perturbation in the charge density can be effectively shielded from the rest of the plasma by the attraction (or repulsion) of neighbouring charges. In order to get some idea of how correlation effects influence the frequency spectrum of scattered light, consider first only the electron feature where the spectral shape is completely determined by alpha.

The simplest illustration is found in the limit $\alpha << 1$ where incident light is scattered from density fluctuations whose scalelength k^{-1} is much less than the Debye length. Here, the long range nature of the Coulomb field is not apparent. Of course, the particles do interact via their electric fields. However, over distances small compared to the Debye length, the net effect of interactions is to produce a locally random distribution of charges. The scattering is the same as would be obtained from totally independent electrons. Because the electrons behave independently in this limit, the total scattered intensity in the ion feature approaches zero, while $S_e(k) \rightarrow 1$ (see equations [8]). The total scattering cross-section becomes $d\sigma/d\Omega = n_e\sigma_e$. The frequency spectrum will be Gaussian in shape corresponding to a Maxwellian distribution of electron velocities. This situation was described earlier in the discussion leading to equation [7]. Only T_e, the electron temperature may be measured from the shape. In order to obtain n_e, the total intensity of radiation scattered into the detection system must be determined. (Calibrating the scattered signal directly in terms of electron density is easily done by Rayleigh scattering from neutral gases. This procedure is described in the next chapter).

The long range nature of the Coulomb force becomes apparent as alpha approaches and exceeds unity. Then, the fluctuations that produce scattering have wavelengths the order of or greater than a Debye length. Scattering from these fluctuations will exhibit the cooperative behaviour of electrons and the spectra will be determined by the properties of the plasma waves.

The most dramatic example is found in the limit of $\alpha >> 1$ or $k^{-1} >> \lambda_D$. The electron feature consists of two narrow spikes or satellites centered about the ion line and shifted by a frequency approximately equal to the electron plasma frequency,

$$\omega_p = (e^2 n_e/\varepsilon_o m_e)^{1/2} . \qquad \text{(mks)} \qquad [10]$$

(Figure 10 shows the electron satellites are reasonably well developed even at modest values of alpha). These long wavelength fluctuations propagate with a large phase velocity. The perturbation field $\overline{\delta E}$, associated with these fluctuations, moves rapidly through the plasma. Slow moving electrons see $\overline{\delta E}$ as a high frequency field and do not have time to respond. However, electrons which are moving with the phase velocity of the wave will readily participate in the oscillation. Scattering off these fluctuations will result in Doppler shifts corresponding to the phase velocity of the wave.

Thus, at large alpha, the fluctuation that produces scattering is a normal mode of electrostatic plasma oscillation. The width of the electron satellites is small compared to their frequency, a feature characteristic of a natural oscillation experiencing only weak damping. Locating these spikes will give an accurate measure of the electron density, but information on the electron temperature is lost. However, the usefulness of the electron feature for large alpha is somewhat limited since, as equations [8] show very little scattered light will be contained in these resonance lines.

The reason that the cross-section for scattering into the electron feature decreases with increasing alpha can be understood as follows. At large alpha, the phase velocity of electron plasma waves greatly exceeds the mean thermal speed of the electrons. Because of the nearly frictionless nature of the electron fluid, the fluctuation amplitude will be determined by only those electrons with velocities comparable to the phase velocity of the wave. As alpha increases, the phase velocity moves farther and farther into the wings of the electron velocity distribution, so that fewer and fewer electrons are able to participate in the oscillation.

An example of the spectral shape corresponding to intermediate values of alpha, i.e. $\alpha \sim 1$ is shown in Figure 10. The important aspect to note is that the electron feature depends only on the parameters of the electron distribution, n_e and T_e through α. The shape of the ion feature is also entirely determined by a single parameter β, defined by:

$$\beta^2 = \frac{\alpha^2}{1+\alpha^2}(ZT_e/T_i) \ . \qquad [11]$$

Parameters of both electron and ion distributions are now present. Similarity with the electron feature can be emphasized if the Debye shielding length for ions is defined,

$$\lambda_{D_i} = (\varepsilon_o \kappa T_i / Ze^2 n_e)^{\frac{1}{2}} \qquad \text{(mks)} \ .$$

This allows a distinction to be made between $\alpha_e \equiv \alpha$, given in equation [9], and the corresponding parameter,

$$\alpha_i = \alpha(ZT_e/T_i)^{1/2} .$$

Then, the shape parameter β for the ion line becomes,

$$\beta = \alpha_i(1+\alpha^2)^{-1/2} .$$

When alpha is small, $\beta \simeq \alpha_i$ is also small and the ion line has a spectral shape which is approximately Gaussian. The ions behave nearly independent of one another so the spectral width is characterized by a Maxwellian distribution of ion velocities. Of course, $\alpha = 0$ corresponds to scattering from totally independent electrons and the ion feature disappears, $S_i(k) = 0$. However, the ion line begins to be a significant component of the spectrum as alpha exceeds a value of about 0.2.

At large α, the limiting value of β is $(Z\,T_e/T_i)^{1/2}$. The sharp satellites that appear in the electron feature for $\alpha >> 1$ only develop in the ion feature when $Z\,T_e/T_i >> 1$ (making β large). Ion acoustic fluctuations are normally heavily damped oscillations and therefore produce a broad scattered spectrum, corresponding to modest values of beta (see Figure 10, for example). Under non-equilibrium plasma conditions ($T_e >> T_i$) ion waves are only weakly damped and distinct ion satellites appear at Doppler shifts determined by the ion acoustic speed,

$$C_s = (Z\kappa T_e/m_i)^{1/2} . \qquad [12]$$

When the ion feature does develop a sharp resonance structure, the ion waves that produce the scattering have a phase velocity C_s which greatly exceeds the average thermal velocity of the ions. As the phase velocity moves farther into the wings of the ion velocity distribution, there are fewer and fewer particles contributing to the fluctuation amplitude. Hence, in complete similarity with the electron feature, the scattering cross-section $S_i(k)$ decreases with increasing beta when $\beta >> 1$. This implies not only large alpha, but also $Z\ T_e/T_i >> 1$. However, in high density plasmas, electron-ion thermalization is rapid and generally, one would not expect extremely large deviations from equilibrium. If $Z\ T_e/T_i < 20$, equation [12] will only approximately locate the ion resonance (Rosenbluth, 1962; Barnard, 1980).

The above distinction between electron and ion features has been necessarily brief. A detailed description of the subtleties of Thomson scattering and plasma wave theory is well beyond the scope of this thesis. In terms of experimental application, one important point to be extracted from the previous discussion is contained in equation [7] or equations [10] and [12], where the electron and ion mass determine the relative spectral widths. This difference is examined further in the following section.

4.3 Advantage of the Ion Feature

Since scattered light must be detected over the thermal self-emission of the plasma, the major advantage of the ion feature is its high spectral brightness. That is, the high scattered power per unit frequency interval. To compare the relative intensities of the two spectral components, the portion of scattered light appearing in either the electron or ion feature may be considered uniformly distributed over the respective frequency intervals,

$$\begin{aligned} \Delta\omega_e &= g(\alpha)kv_e \\ \Delta\omega_i &= g(\beta)kv_i \ . \end{aligned} \qquad [13]$$

The factors g in equations [13] have been introduced to allow for the fact that scattered light may be quite non-uniformly distributed. In particular, for large alpha or beta, sharply defined resonance structure can appear and $g \ll 1$. At very small values of the scattering parameter, the spectral shape approaches a Gaussian function, $g(0) = \ln 2$, and equations [13] specify the half width at half maximum. As well, equations [13] specify a common scattering vector k so that comparison will be made for a given, though arbitrary, scattering geometry.

The spectral intensity of the ion feature, relative to the electron feature can therefore be defined as:

$$I = \frac{S_i(k)\Delta\omega_e}{S_e(k)\Delta\omega_i}$$

Using equations [8] and the frequency intervals from equations [13] gives

$$I = \frac{g(\alpha)}{g(\beta)} \left\{\frac{T_e m_i}{T_i m_e}\right\}^{\frac{1}{2}} \frac{Z\alpha^4}{1+\alpha^2(1+ZT_e/T_i)} \qquad [14]$$

Equation [14] is presented graphically in Figure 11 where the plasma has been assumed to be an equilibrium helium plasma: $Z = 2$, $T_e = T_i$. As alpha increases from zero, the fraction of scattered light contained in the ion line increases with alpha like α^4. The two features have comparable brightness ($I = 1$) at $\alpha = 0.28$. At $\alpha = 1$, the ion line is 43 times brighter than the electron feature. At larger alpha, the narrow electron resonance structure begins to appear and the spectral intensity of the electron feature increases. The width of the electron resonance is determined by the amount of damping experienced by electron plasma waves. To evaluate equation [14] for large alpha, account must be made of both Landau damping and collisional damping contributions to the spectral width (Evans, 1969).

Landau or collisionless damping decreases exponentially with increasing alpha and the spectral intensity of the electron resonance correspondingly increases. However, the spectral width cannot decrease indefinitely since, ultimately, the frequency of electron-electron collisions will determine the rate of energy dissipation from the wave. Collisional contributions to the spectral width can be expressed in terms of $N_D = \lambda_D^3 n_e$, the number of particles in a Debye cube. Equation 14 corresponds to the collisionless case, that is, N_D approaching infinity. However, Figure 11 also illustrates how N_D affects the relative brightness.

The conclusion to be drawn from Figure 11 is that the ion line is indeed the most intense feature of the scattered spectrum over virtually the entire range of the scattering parameter alpha.

Because of the ease of detection, the ion feature finds its most important application in plasmas of relatively high electron density where

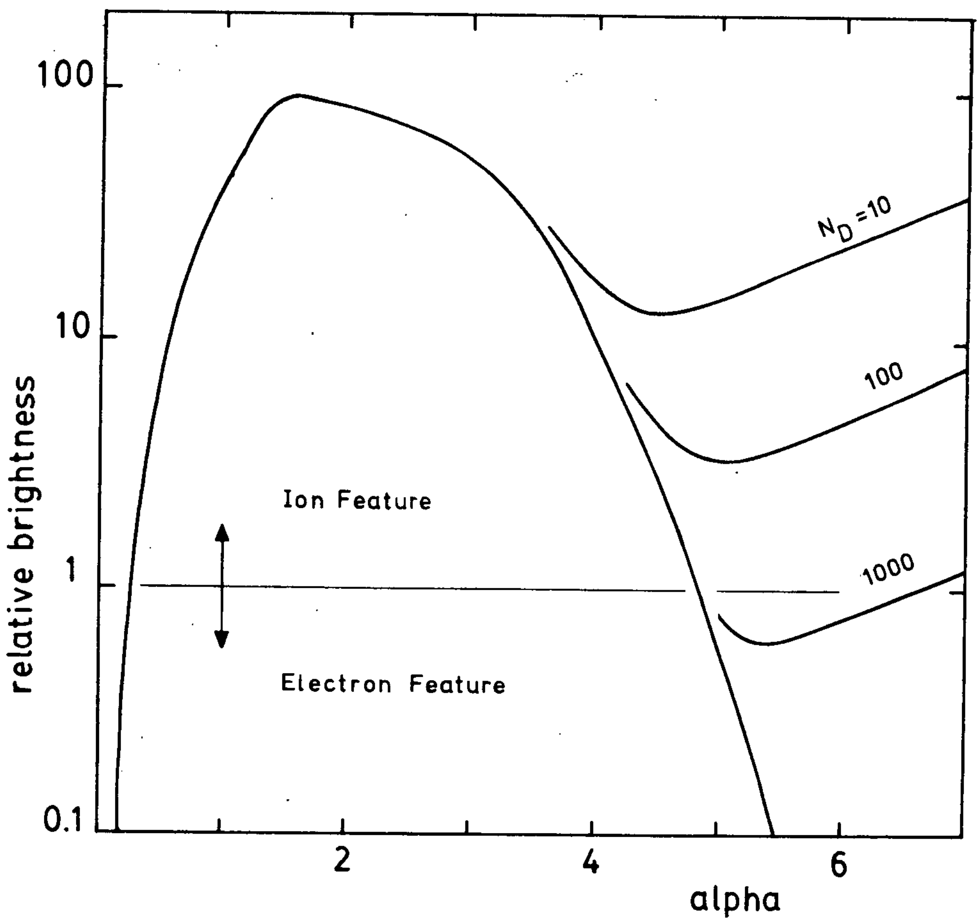

<u>Figure 11</u>

Comparative spectral brightness of electron and ion features. A relative brightness greater than unity indicates that the spectral brightness of the ion feature exceeds that of the electron feature (see equation 14).

bremsstrahlung emmission is large. The classical expression (Zel'dovich, 1966) for the spectral brightness of electron-ion bremsstrahlung, J_B has the dependence:

$$J_B \propto \frac{n_e^2}{T^{\frac{1}{2}}} \exp(-h\nu/\kappa T) \ .$$

At optical frequencies $h\nu \approx 2$ eV, the exponental factor is virtually constant for all plasmas having temperatures ($T_e = T_i = T$) more than a few eV. The total amount of scattered light however, is linearly proportional to the density and is contained in the interval $\Delta\omega \propto k(\kappa T)^{\frac{1}{2}}$. The corresponding spectral brightness of scattered light, J_s will behave like,

$$J_s \propto \frac{n_e}{kT^{\frac{1}{2}}} \ .$$

The k^{-1} dependence in J_s shows that scattering from slow fluctuations with small k will lead to bright scattered spectra. Forming the ratio:

$$J_s/J_B \propto (kn_e)^{-1}$$

shows that, roughly independent of the temperature, the higher the plasma density, the more difficult it is to interrogate with scattering techniques. Therefore, at high plasma densities, advantage must be taken of the brightness of the ion feature.

CHAPTER 5 DESCRIPTION OF THE SCATTERING EXPERIMENTS

5.1 Introduction

This chapter describes in detail the experimental arrangements that were used for Thomson scattering in the Z-pinch plasma. It is worth mentioning here that, in spite of the discussions from the last chapter, the scattering experiments first attempted to investigate the electron feature. If it could be detected, the electron feature would serve as a cross-check on the plasma parameters obtained from the ion feature. However, because of the very high levels of bremsstrahlung emission, signal to noise ratios in the electron feature were prohibitively low. As will be seen later, the ion feature did not suffer from this limitation.

The first section of this chapter shows the two separate geometries that were used to examine scattering from ion acoustic fluctuations. An analysis of the geometries will distinguish between the two scattering systems while a few numerical estimates will help to illustrate some of the characteristics and parameters of the ion feature that were mentioned in the previous chapter. The following considerations indicate why two separate scattering systems were chosen and that, in fact, the present diagnostic experiments are intimately related to the CO_2 laser-plasma interaction experiments.

One of the primary interests in laser-plasma interaction experiments is the study of non-linear parametric processes which, among others, includes stimulated Raman or Brillouin scattering. A complete description of these processes can be found elsewhere (e.g.: Chen, 1974; Siebe, 1974). These processes are scattering instabilities which are produced with very high incident laser intensities. The easiest instability to excite, and therefore most important, is the Brillouin mode, whereby the CO_2 laser is scattered by and enhances an ion acoustic wave. (Stimulated Raman scattering involves the electron Langmuir wave).

At the expense of some of the incident laser energy, plasma waves can be excited to amplitudes which are many orders of magnitude above the normal thermal level of plasma fluctuations. As well, the most unstable fluctuations are those which scatter the CO_2 laser beam directly back onto itself so that the enhanced plasma fluctuations will have a wavelength $\lambda = \lambda_{CO_2}/2$. The CO_2 laser-plasma interaction experiments will therefore generate specific, long wavelength, and highly non-thermal fluctuations in the plasma density.

One of the Thomson scattering geometries has been arranged to directly examine the properties of such enhanced fluctuations through the scattering of ruby laser light. In order to do this, the wavevector for Thomson scattering must be matched, in both magnitude and direction, with the wavevector of the fluctuation induced by CO_2 laser. This in turn requires that scattered ruby laser light be observed at very small forward angles. Also, in order to correlate the stimulated processes with the plasma parameters, one would like to have a simultaneous measurement of the plasma temperature and density in the interaction volume. This can be done by measuring the spectrum of the thermal level of density fluctuations. Therefore, a second Thomson scattering geometry is arranged to scatter from density fluctuations that are determined only by the thermal properties of the plasma and are totally uncorrelated with the stimulated scattering processes (except in as much as the CO_2 laser may change the local thermal properties). The second Thomson scattering geometry therefore looks at short wavelength fluctuations in the extreme back scatter direction.

For the present purpose of establishing the plasma conditions prior to introducing the CO_2 laser, both scattering systems are used to observe the thermal level of ion fluctuations. The plasma parameters measured from scattered spectra are the electron density from the intensity of scattered light, and the ion temperature from the spectral distribution. Even though it will be assumed throughout that the electron and ion temperatures are equal, it is important to reiterate that the spectral width of the ion feature is determined by the distribution of ion velocities. As a result of this, many details of the scattering geometry and detection systems will be dominated by the relatively high resolution capabilities needed to examine the ion feature. It will be seen shortly that only the back-scatter spectrum has a wavelength spread that is wide enough (a few angstroms) to be resolved easily.

The final section of this chapter describes calibration of the sensitivity of the detection systems by Rayleigh scattering from neutral gases. Calibration is required in order to determine the electron density. When scattering into the electron feature, this procedure is often not necessary since the spectral shape, determined by alpha, is quite sensitive to both the electron temperature and density. Then, measurement of the width and shape can be used to determine n_e and T. However, the shape of the ion feature, determined by the beta, is particularly insensitive to either plasma parameter (see equation [11]). Therefore, calibration of the detection systems will be necessary for density measurements which utilize the ion feature.

5.2 Arrangement of the Scattering Geometry

Orientation of the plasma with respect to the wavevectors for Thomson scattering is shown in Figure 12. With reference to Figure 12, the following description will give an indication of some of the numbers involved and help to clarify how the scattering systems are arranged. What can be expected in terms of the spectral distribution of scattered light will also be given. When plasma parameters are required in calculations, the initial estimate of Houtman is used for the maximum plasma temperature while the maximum density is taken from the estimates made in Chapter 3, i.e.:

$$n_e = 4 \times 10^{19} \text{ cm}^{-3}$$

$$T = 40 \text{ eV.}$$

The wavevector of the density fluctuation producing scattering is $\bar{k}_x = \bar{k}_o - \bar{k}_{xs}$. The double subscripting here and in Figure 12, distinguishes between forward, x = f and backward, x = b scattering directions. The incident ruby laser beam has $k_o = |\bar{k}_o| = 2\pi/6943$ Å or $k_o = 9.05 \times 10^4 \text{ cm}^{-1}$. Because scattered light is only slightly shifted from the incident laser wavelength $k_o = k_{xs}$ to a very good approximation so that $k_x = 2k_o \sin(\theta_x/2)$ is determined solely by the angle θ_x between incident and scattered beam directions. For the forward scattering system, k_f lies parallel to the plasma axis and $\theta_f = 7.5°$. This angle is determined by the requirement that the Brillouin process be interrogated: $k_f = 2\, k_{CO_2} = 1.19 \times 10^4 \text{ cm}^{-1}$.

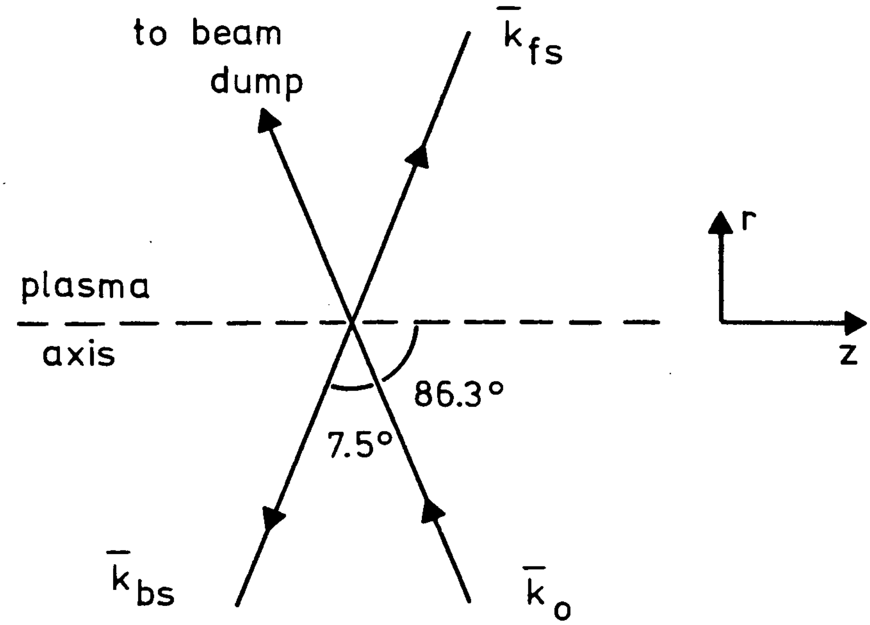

FIGURE 12

Geometry for the Thomson Scattering Measurements

Backscattered light is detected in the antiparallel direction having θ_b = 172.5° with $k_b = 1.81 \times 10^5$ cm^{-1}. The fluctuations observed in backscatter will propagate in the radial direction, perpendicular to both the plasma axis and k_f. As mentioned in the introduction, the k-vector arrangement has been chosen with the interaction experiments in mind.

Refering back to the previous chapter, the spectral width $\Delta\omega_i \simeq kv_i$ can be estimated using the above k-vectors and a plasma temperature of 40 eV. (As a matter of convenience, the widths will be expressed in wavelength units. The conversion is easily done since the frequency shifts $\omega_i = \omega_o - \omega_s \simeq d\omega_o$ are small, and incident light, at frequency $\omega_o = k_o c$, will appear shifted according to: $d\omega = cdk = \omega_o d\lambda/\lambda_o$, c being the speed of light in vacuum.) For the backward scattering system, the ion feature can be expected to have a FWHM of approximately 6.0 Å at maximum plasma compression, while the spectrum in forward direction will be narrower by the factor k_{fs}/k_{bs}, making the width only about 0.4 Å.

The above calculations, along with others such as the plasma Debye length and relevant scattering parameters, are quite straightforward. Table II gives a summary of numerical estimates for a few of the important parameters used to describe the plasma and the two scattering systems. Though these estimates are only representative of peak compression, they do serve to point out particularly that, in high density plasma, alpha is large while N_D is small. Comparing the relevant numbers from Table II with Figure 11 reinforces the fact that only the ion feature will be detectable in the current scattering experiments.

Since the objective of these experiments is to determine what the plasma parameters are during all stages of the high compression phase and therefore establish initial conditions for the interaction studies, both

TABLE II

Numerical Estimates for the Thomson Scattering Systems

Z-pinch plasma parameters: helium, Z = 2
(at peak compression)

$$n_e = 4.0 \times 10^{19}\ \mathrm{cm}^{-3}$$
$$T_e = T_i = T = 40\ \mathrm{eV}$$

$$v_i = 4.3 \times 10^{6}\ \mathrm{cm\ sec}^{-1}$$
$$\lambda_D = 7.4 \times 10^{-7}\ \mathrm{cm}$$
$$N_D = 16$$

Ruby laser scattering parameters:

$$\omega_o = 2.72 \times 10^{15}\ \mathrm{sec}^{-1}$$
$$k_o = 9.05 \times 10^{4}\ \mathrm{cm}^{-1}$$
$$\lambda_o = 6943\ \text{Å}$$

	Forward	Backward	
θ	7.5	172.5	(deg.)
k	1.2×10^4	1.8×10^5	(cm^{-1})
$\Delta\lambda_{FWHM}$	0.40	6.0	(Å)
α	112	7.5	
β	1.4	1.4	

scattering systems are used only to measure the unperturbed thermal properties of the Z-pinch. It is unfortunate that the scattering diagnostics has not been used to make measurements with the CO_2 laser incident in the plasma. The reasons for this stem from the two principle factors, the first of which is a circumstance essentially historical in nature.

Originally, the set-up for these laser/plasma interaction experiments (Albrecht, 1979) had the CO_2 laser beam introduced axially into the plasma. Parametrically enhanced fluctuations would therefore propagate in the axial direction and could be interrogated with the forward scattering arrangement shown in Figure 12. Such a configuration, however required that the CO_2 laser beam propagate almost parallel to, and half the length of the plasma column. Although many focussing schemes attempted to eliminate severe refraction effects, it was virtually impossible to introduce the CO_2 laser light axially so that the interaction volume and diagnostic volume had sufficient overlap without dramatically altering the plasma characteristics. The interaction geometry has since been changed to have the CO_2 laser incident radially into the plasma as was described in Chapter 2.

The second, and main reason for Thomson scattering without introduction of the CO_2 laser light is a direct result of the quite general experimental difficulties of any scattering experiment. In particular, the detection system must have sufficient resolution capabilities to see the shape of the ion feature. A spectral width of 6.0 Å corresponding to the expected backscatter spectrum is of course not large, but is well within the resolution range of typical monochromators. The forward scatter ion feature is considerably narrower making resolution of this spectrum with conventional techniques a much more difficult problem. Scattering with spectral resolution is therefore only attempted in the backscatter system where the proposed detection system can be used and the difficulties of extending the method to higher resolution experiments can be examined.

Non-resolved measurements of the forward scatter intensity are relatively easier to perform and can be done similtaneously with the backscatter measurements. Data obtained in forward scatter will be a valuable cross-check of the results obtained from the analysis of back-scattered light.

Having discussed the salient features of the scattering vectors and their geometrical arrangement, the remainder of the scattering experiment will now be described.

5.3 Overall Layout of Experiment

The full arrangement of the two scattering systems is shown in the semi-schematic diagram of Figure 13. The orientation of the discharge vessel with side arms and viewing ports, etc., will be recalled from the earlier descriptions of Chapters 2 and 3.

The incident light source is a conventional Q-switched ruby laser oscillator in combination with a single amplification stage. Because the scattered spectra are rather narrow, it is of interest to consider the spectral distribution of incident light.

The oscillator cavity has a 100% rear reflector and the output coupler is a 66% reflecting, multiple surface Fabry-Perot etalon. The etalon provides for some longitudinal laser mode selection. The etalon has a measured mode spacing of 0.37 Å, each mode being less than 0.06 Å in width. The mode spacing, however, is somewhat less than the gain narrowed width of the laser flourescence line. Consequently, the laser output has a

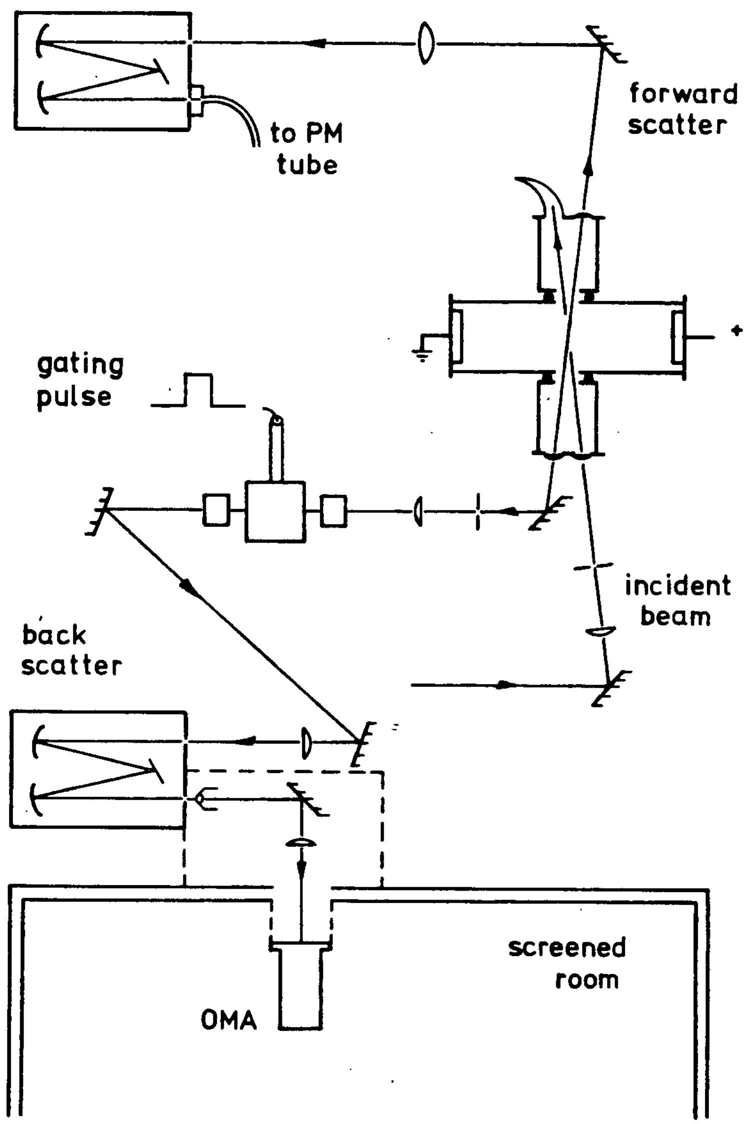

FIGURE 13

Layout of the scattering experiment.

wavelength distribution consisting of several narrow spikes separated by the etalon mode spacing. Usually, only one or two longitudinal modes of the etalon are present, but often, one or two slightly off-axis modes also appear in the output spectrum. This structure in the laser spectrum is always contained within less than a 0.6 Å interval. However, the scattered spectrum in the forward direction is expected to be much less than 1Å wide (see Table II). Therefore, spectrally resolved measurements of the forward scatter ion feature will require consistent isolation of a single etalon mode. In backscatter, the wavelength distribution of incident light is sufficiently small and can be ignored as being a significant contribution to the width of the scattered spectrum.

Power levels in the incident beam are typically about 300 MW, or 6 joules in a 20 ns FWHM pulse. In order to minimize the amount of stray laser light entering the detection optics, the entire laser and incident beam path is housed in a light tight arrangement of boxes and tubes. Also, immediately prior to introducing the beam into vacuum, it is focussed through a helium flushed spatial filtering pinhole. Helium gas is used to reduce the possibility of laser breakdown sparks at the pinhole (Morgan, 1975). Filtering the beam helped eliminate spurious off-axis lasing modes which were found to contribute significantly to stray light levels. The 'cleaned' beam is then focussed onto the pinch axis to a spot diameter of approximately 0.25 mm. Incident light which is transmitted through the plasma is collected in a Rayleigh horn beam dump, intended to absorb completely all unscattered radiation.

The forward scatter beam path consists of a series of mirrors and lenses which transport the scattered beam and image the scattering volume onto the entrance slit of a Spex 3/4 meter focal length monochromator. The ion feature though is not spectrally resolved so the monochromator acts only to filter out background light from the plasma. Exit slits are set to transmit only a 7 Å wide band, centered on the laser wavelength. Beyond the exit slit, a low loss optical fiber bundle collects and transports light to a photomultiplier. Oscilloscope traces of the photomultiplier output are photographed giving a temporal record of the light that is collected. Such power measurements provide additional discrimination against plasma light since scattered light is present only for the 20 ns duration of the laser pulse. On this time scale, the average level of plasma background light does not change significantly and background light essentially appears as an additional bias or baseline on the scattered signal. (The limitation here is due to fluctuations in the baseline that result from shot noise in both the photomultiplier and in the emission of photons by the plasma. Scattered light must still be detected over and above such statistical fluctuations.)

In backscatter, the detection system is designed to record the full spectral distribution of scattered light on single shot of the ruby laser. Much of the complexity of the backscatter optical system is based on matching the collection and dispersion optics to the detector characteristics. The detector is an Optical Multichannel Analyser (abbreviated OMA) produced by Princeton Applied Research Corp. (model 1205I detector head with model 1204 A electronic control console). The OMA is essentially an extremely sophisticated electronic image converter camera, this particular model having two stages of image amplification. Details of the design and operation of the OMA can be found in the instruction manuals available from PAR Corp. For a discussion of the backscatter optics, only the following brief description is given.

An optical image on the detector head photocathode is segmented into a linear array of 500 channels, each corresponding to a 0.025 mm wide by 5.0 mm high portion of the photocathode. The full active portion of the target area is 12.5 mm by 5.0 mm. Amplified photoelectron signals are collected during a 768 μs "on" time, after which, the accumulated signal in each channel is digitized and stored in memory. For any given channel, one digital count corresponds to the accumulated effect of approximately 20 visible photons incident on the photocathode. (The quantum efficiency of the photocathode is 60%). Two aspects of the detector are of importance here. First, the finite width of each detector channel requires that the OMA spatial resolution be matched with that of the dispersion instrument for optimum spectral resolution. Secondly, since optical input to the OMA is accumulated, i.e.: time integrated, discrimination between scattered light and plasma background must be made on the basis of energy rather than power.

Dispersion of the spectrum is provided using a second Spex 3/4 m focal length monochromator equipped with a 1200 line/mm grating, blazed in 1st order for 7000 Å. The monochromator has a collection ratio of F/7.5 and a reciprocal dispersion of 10 Å/mm. The entrance slit was set at 0.012 mm wide by 0.350 mm high. Imaging 1:1 at the exit plane gives a spectral resolution interval of 0.12 Å FWHM. Additional external optics, consisting of a x5 microscope objective and a beam transport lens, images the monochromator exit plane onto the OMA head with a total magnification of x10.5. The monochromator entrance slit therefore covers 75% of the height of 5 OMA channels. The maximum resolution with this arrangement is 0.12 Å (0.024 Å/channel). This matching is not quite optimal since the width of the monochromator entrance slit used is slightly more than twice the diffraction limited capabilities of the instrument. Also, the OMA has a spatial resolution of 3 channels FWHM, this limitation being due to electrical cross-talk between adjacent OMA channels. For the backscatter spectrum, attention to fine details of the matching is unimportant since Table II indicates that the system described above has more than adequate resolution. However, this system may not have sufficient resolution to examine the spectrum of forward scattered light. Therefore, the backscatter arrangement attempts to provide at least a near limitation test of the detection system.

Discrimination against plasma light is vital since bremsstrahlung is emitted over the several microsecond time interval of the discharge compared with the 20 ns duration of scattered light. The OMA has an electrical gating mode which permits light to be detected only for the duration of a user supplied voltage pulse. However, for short gating pulses there are distortions in the electronic imaging stages which severely degrade the resolution capabilities of the instrument (Simpson, 1977; Albrecht, 1978). The OMA is therefore used in the continuous recording (or 'real time') mode and an electro-optic shutter performs the gating function. The shutter operates in the following simple way.

Backscattered light is passed through the series combination of polarizer, pockels cell, and crossed polarizer. The pockels cell is a double crystal, KD*P unit having a half-wave voltage of 2.2 kV and polarizers are of the Glan-Thomson type. The first polarizer takes advantage of the linear polarization of the ruby laser beam by passing all scattered light and rejecting one-half of the plasma emission. Now, when the pockels cell is not activated, the polarization of light transmitted through the cell is not altered and therefore will be blocked by the second polarizer. If the pockels cell is supplied with its half-wave voltage, light entering the cell will exit with the plane of polarization rotated by 90°. Then, the second polarizer will be transmitting. For gating purposes, a krytron triggered, cable discharge circuit is used to generate a 2.2 kV, square wave voltage pulse of 100 ns duration. The gate pulse is centered in time on the incident laser pulse. Plasma emission occurring outside this time interval is suppressed.

In order to obtain a good on-off contrast ratio with this optical gating method, light passing through the polarizer/pockels cell arrangement must be accurately collimated. A 50 cm focal length lens collects the scattered light (F/16 collection cone) and images the scattering volume onto a field limiting pinhole. Scattered light is transmitted through the pinhole and then collimated. This collimated beam is passed through the shutter and then refocussed onto the monochromator entrance slit. (Overall, the entrance slit is imaged onto the plasma axis with X0.71 magnification).

With perfect collimation, the on-off contrast ratio can exceed 1000:1, but the observed contrast is about an order of magnitude lower. The effect of poor contrast has been very important because of the relative time scales involved. This can be understood by making the following observations. Plasma light and scattered light will of course be collected during the shutter's 100 ns on time. Also, because the OMA time integrates, plasma emission will register (as leakage light) for the full duration of the discharge, namely, a few microseconds. The overall effect for these experiments is that, by using the optical shutter, plasma background levels are reduced only by approximately a factor of 10. However, it will be seen that this has been sufficient to give very good signal to noise ratios in the scattered spectra.

5.4 Calibration of the Optical Systems

A calibration of the detection sensitivity must be performed in order to determine electron densities from observed scattered intensities. Therefore, before showing some of the plasma scattering spectra, calibration by Rayleigh scattering is discussed. In the process, an important limitation of the current geometry will be pointed out.

The frequency integrated differential scattering cross-section is related to the electron density n_e by:

$$d\sigma/d\Omega = n_e \sigma_e S_i(k) \ .$$

Direct application of this relationship requires an absolute calibration of the complete imaging and detection system, a very difficult if not impossible procedure to implement with reliability. The general practice is to perform a relative calibration by Rayleigh scattering off neutral gases. This form of calibration can be done as follows.

Given the present scattering system, the discharge vessel is filled to a number density, n_o of molecules with known Rayleigh cross-section σ_R. Scattering off this gas produces a signal P_R which, when normalized to the incident laser intensity, can be expressed as

$$P_R = n_o \sigma_R V_R f \ .$$

All molecules contributing to P_R are contained in the scattering volume V_R. The unspecified factor f contains all properties of the system that remain identical for both Thomson and Rayleigh scattering experiments. For example, factors such as: solid angle of collection, throughput of imaging components, dispersion instruments or detectors, etc., would all be included in f. Using exactly the same system for Thomson scattering gives a similar expression for scatter into the ion feature,

$$P_T = n_e \sigma_e S_i(k) V_T f \ .$$

Forming the ratio P_T/P_R and solving for the electron density, n_e gives:

$$n_e = \frac{P_T}{P_R} \left\{ \frac{n_o \sigma_R V_R}{S_i(k) \sigma_e V_T} \right\} , \qquad [15]$$

where the factor in square brackets is just the calibration constant for the detection system.

Given $S_i(k)$, the electron density may be determined simply by comparing the plasma scattering signals with those obtained by scattering from a known pressure of calibration gas. Many gases can be used for calibration purposes (George, et. al., 1965; DeSilva, 1970) the most common being nitrogen where $\sigma_R/\sigma_e = 3.65 \times 10^2$. Assuming for the moment that $V_R = V_T$ and $S_i(k) = 1$ then scattering from 110 torr of N_2 will give the same total signal as a plasma with $n_e = 1.0 \times 10^{16}\ cm^{-3}$.

It should be noted that Rayleigh scattered light has a bandwidth which is very small, being determined from Doppler broadening by molecules in a room temperature gas. Therefore, measurements must be made at the laser wavelength. Even at zero gas pressures, laser light can be accidentally scattered into the detection system giving a constant level of stray light which will be added to the Rayleigh signal. When stray light is present, the true Rayleigh signal is determined by examing the linear variation of scattered intensity with gas pressure. Extrapolation to zero pressure will reveal the stray light level.

Measurement of the electron density using equation [15] does require a knowledge of $S_i(k)$ and hence of alpha. For both scattering systems, Table II shows $\alpha >> 1$ and therefore $S_i(k)$ approaches the constant value $Z/(1+ZT_e/T_i) = 2/3$. Apart from the discrepancy in volume then, equation [15] is essentially independent of alpha, giving a quite simple determination of n_e.

In many circumstances, equation [15] can be further simplified since the two volumes V_R and V_T are identical and can be incorporated into the cancelled factor f. However, for the current experiment this is not the case. Figure 14 shows the scattering volume in detail. This figure is to be viewed in conjunction with the wavevector diagram of Figure 12. The incident beam is focussed to a diameter d = 0.25 mm on the plasma axis. Imaging the monochromator entrance slits at a shallow 7.5° angle with respect to $\bar{k}_o$ produces a rather long region of overlap from which scattered light will be collected. With the geometry of Figure 13, the scattering volume is determined to have a length, normal to the plasma axis of L = 1.9 mm. Recalling the streak or shadow photographs, the diameter of the high density plasma core is significantly smaller than the scattering volume during portions of the pinch phase.

Two important aspects of the scattering system should therefore be kept in mind when viewing and analyzing scattered signals. Firstly, when equation [15] is used to calculate electron densities, the relative volumes V_R/V_T must be estimated and this is taken to be directly proportional to the respective lengths of the scattering volumes, L_R/L_T. Using Figure 14, L_R is fixed at 1.9 mm. As long as the plasma diameter is larger than this, $L_R = L_T$. Otherwise, L_T is measured from streak photographs as the bright core diameter. The second, now obvious point, is that along the viewing direction there is considerable lack of spatial resolution. Parameters determined from scattered light will therefore be average values for the high density plasma core.

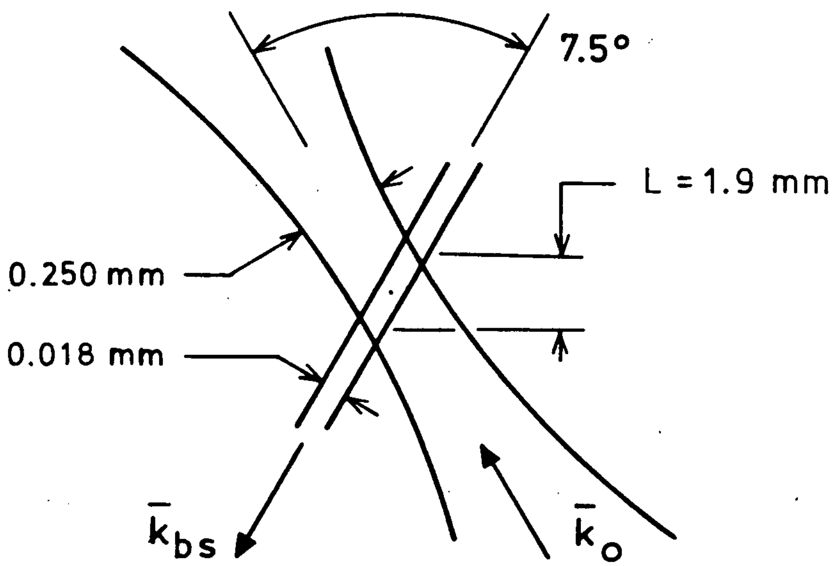

FIGURE 14

Details of the scattering volume

CHAPTER 6 SCATTERING OBSERVATIONS AND RESULTS

6.1 Introduction

Some aspects of the scattering experiments were not quite expected and lead to a few questions about the interpretation of observed signals. The first section of this chapter presents a sampling of the raw spectral data to show the type of information that was obtained. Answers to the questions that arose will give better insight into the shock wave nature of the plasma structure at pinch time. As well, it will be seen that the effects of refraction can enter into consideration in rather a subtle way. A complete interpretation of the data will be seen to rely heavily on the earlier streak and shadowgram observations.

The final section of this chapter concludes the scattering experiments by presenting the electron temperature and density measurements obtained for the full duration of the pinch phase. The data confirm and extend the results of previous experiments on this Z-pinch. The density measurements are compared with the estimates made in Chapter 3, and, in particular, with the snow-plow model of plasma collapse.

6.2 Discussion of the Spectra

A few backscatter spectra are reproduced in Figure 15. Each of the spectra was recorded on a single shot of the ruby laser. These traces display the full 500 channel OMA records. The horizontal scale spans a total wavelength interval of 12 Å, though note that the scale is inverted, wavelength increasing linearly to the left. The top spectrum, Figure 15(A) is a calibration shot showing Rayleigh scattering from 1/2 atmosphere of nitrogen gas. Laser mode structure due to the oscillator output etalon is

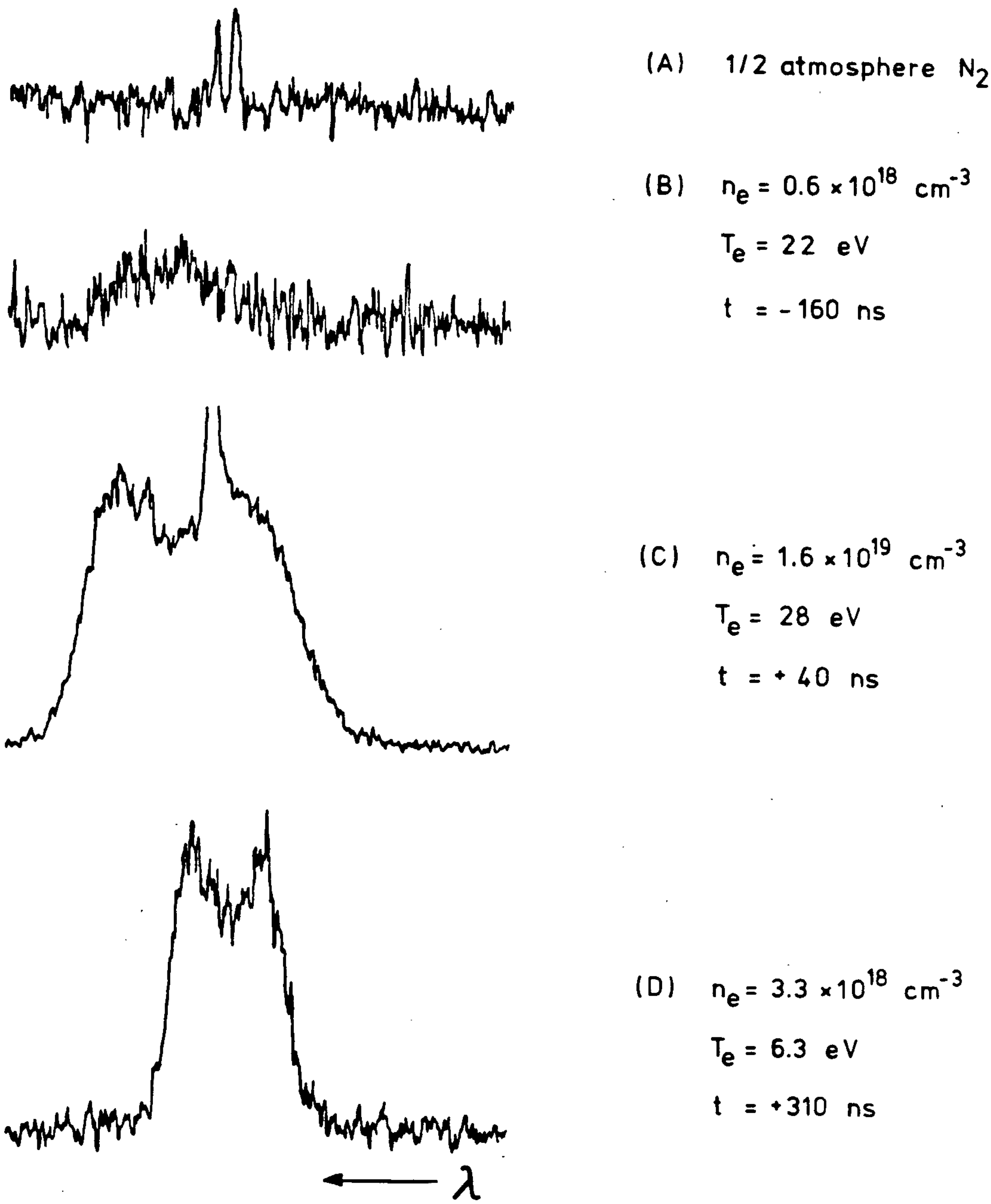

FIGURE 15

Examples of observed spectra. The full interval displayed is 12 Å, with wavelength increasing to the left.

evident. For this shot, there were only two longitudinal modes present, with the modes separated by 0.37 Å. The remaining three spectra are plasma scattering events, each labelled according to the observation time and computed temperature and density.

Spectra 15(A) and 15(B) are displayed with approximately equal sensitivities in the vertical direction. Compared to the calibration shot, 15(B) shows statistical fluctuations of the baseline which are now more severe since plasma background light is also recorded. As well the plasma density is low and baseline fluctuations make for a rather ill-defined spectral shape. However, Thomson scattered light is clearly present. The bottom two spectra in Figure 15 show that higher density plasma give quite strong scattered signals, well in excess of the noise levels.

In order to illustrate one complication that can arise when Thomson scattering from high density plasma, the first observation to be discussed is concerned with the level of stray light appearing in both forward and backward scattering detection systems. For the series of calibration shots, Rayleigh scattering was measured as a function of fill pressure in order to ascertain the detection sensitivity along with the stray light levels (see Section 5.4). In backscatter, there was no measurable stray light. In forwardscatter, stray light was present, and only amounted to scattering from an equivalent electron density of 7×10^{16} cm^{-3}. This level of stray light is well below the electron densities of interest and, though accounted for in the analysis, it was not a significant contribution to plasma scattering signals during most of the pinch phase.

However, around the time of maximum compression the forward scattering signals would show unpredictable shot to shot variations (for fixed timing) of as much as six orders of magnitude above expected thermal scattering levels. Large amounts of stray light also appear in backscattered spectra, though only when the forward scatter signals are greatly enhanced. Figure 15(C) gives an example of this circumstance. The narrow spike superimposed on top of the scattered signal is stray light. Like the Rayleigh scattered signal in Figure 15(A), stray light is unbroadened and appears at the laser wavelength. Figure 15(B) and (D) show no stray light, consistent with the N_2 calibration.

These observations are of course explained by noting that the applicability of a shadowgram technique depends on ray bending. The angular deflection estimates made earlier do indicate that the incident ruby laser light can be deflected to such an extent that transmitted light will be inadequately absorbed by the beam dump. Considering that the incident beam power is at the megawatt level while scattered light is measured at the photon level, it is easy to see that even slightly inefficient beam dumping can lead to serious stray light problems. The large enhancements of forward scattered light and correlated appearance of stray light in the back scatter spectrum have therefore been attributed to high levels of stray light brought about by refraction of the incident laser beam.

A second aspect of the spectra to notice is that the middle two spectra of Figure 15 appear noticably red shifted with respect to the incident laser wavelength. It will be recalled, from the wavevector geometry of Figure 12, that the backward direction detects scattering from density fluctuations which propagate in the radial direction. Therefore, a net displacement of the spectrum gives an indication of the average radial speed of plasma contained within the scattering volume.

Radial velocity estimates based on a net Doppler shift of the spectra are not very accurate since the shifts are much smaller than the width of the spectra, and, primarily because the shifts observed are of the same magnitude as shot-to-shot fluctuations in the wavelength of incident light. (For some spectra like 15(C), stray light has aided as a wavelength reference). As well, only a limited number of shots were made at early times when the red shifts were significant. Nonetheless, the shifts are significant and Table III presents the radial velocity measurements, dr/dt, as they could be extracted from the available scattering data.

TABLE III

Radial Speeds from the Scattering Spectra

Time (ns)	dr/dt (x 10^6 cm sec^{-1})
-150	-3.2 ± 1.6
$-50 < t < 0$	-0.9 ± 0.4
$t > 0$	0

The above measurements can be considered along with the streak and shadowgram results presented in Chapter 3. Most notably, the first two entries in Table III show that the scattering volume, located near the plasma axis, sees radial speeds that differ with time. The outer boundary of the plasma (see Figures 7(A) and 7(B)) moves inward with an approximately uniform speed, which is roughly equal to the second entry in Table III. At somewhat earlier times, plasma near the axis is travelling significantly faster. This difference in plasma speed near the axis is at least qualitatively consistent with a description of the pinch effect that includes the formation of shock waves (Allen, 1957). The difference in speed can be understood as follows.

The magnetic forces driving plasma inward act much like a piston driven into a gas filled tube. Compressed plasma, collected up by, and moving inward with this magnetic piston, can be preceded by a shock wave travelling inward faster than the bulk of the plasma located near the piston. The shock front therefore reaches the axis sooner than the bulk of the plasma. Since the scattering volume is located near the plasma axis, the net Doppler shift at early times is interpreted as indicating the appearance of the shock front, while, shortly afterwards, slower plasma, accumulated at the piston, would enter the scattering volume. Radially directed motions would eventually be thermalized and no net Doppler shift would be evident, as the final entry in Table III indicates.

This view of the pinch phase could have been alluded to in Chapter 3 when the streak pictures (Figures 4 or 7) were discussed. Development of a two component structure in the plasma column is also indicative of the shock wave nature of plasma collapse. In particular, the precursor shock converging on axis is what initiates formation of the high density plasma core. However, the photographic experiments do not measure particle velocities directly. In combination with Chapter 3, the Doppler shift data can be explained qualitatively, but, the scattering experiments lack the spatial resolution required to make quantitative evaluations of the shock structure.

The final point of discussion in this section concerns again the net wavelength shift appearing in the backscatter spectra. A question about the average Doppler shift arises, not from the presence of a red shift, but from the absence of a blue shift. Presumably, if the scattering volume is symmetrically located on the plasma axis, scattered light should be observed from both 'sides' of the plasma. The region of plasma nearest the laser and backscatter optics will be moving away from the incident beam giving rise to the observed red shift. Beyond the axis, plasma collapsing radially inward will in fact be moving towards the incident beam. Hence, one would expect not only red shifted spectrum, but also a similtaneous blue shifted one, the total spectrum showing symmetry about the ruby wavelength. One plausible explanation for the absence of a blue shifted component will be put forward in terms of refraction. Before doing so though, it is worth indicating why refraction effects were considered a plausible explanation.

As has already been shown by shadowgrams and, from the discussion of stray light there can be rather large deflections of ruby laser light by the plasma. Figure 9 shows that the angular deflections can exceed approximately 23 mrad or 1.3 degrees. In fact, during the course of the interferometric measurements, it was verified that the sharp density gradients, existing near the core boundary, produce deflections in excess of 3.5°. Nonetheless, if it is accepted that the maximum deflection is 1.3°, refraction effects will be negligible if this deflection is small compared to the acceptance angle of the backscatter collection optics. However, this is not the case. Recalling the discussion in Section 5.3, backscattered light is collected by a 50 cm focal length lens which views the scattering volume with an F/# of 16. In other words, the collection cone has a half-angle of 1.8°. Therefore, the minimum deflection angle is quite comparable with the maximum acceptance angle. The following discussion illustrates how such a circumstance can lead to only red-shifted spectra.

Consider then that the scattering volume is symmetrically located on-axis and represents a line source of light. The total amount of scattered light collected by the backscatter optics will be some integral over all the elemental contributions along the line. Figure 16 shows a cross-section of the high density core plasma and indicates how two symmetrically located portions of the line would contribute to the total signal. Also, in Figure 16, the scattering volume has a length which is comparable to or larger than the core diameter.

On the left of the plasma axis, scattered light, originating from plasma moving towards the incident beam, must re-traverse the plasma and

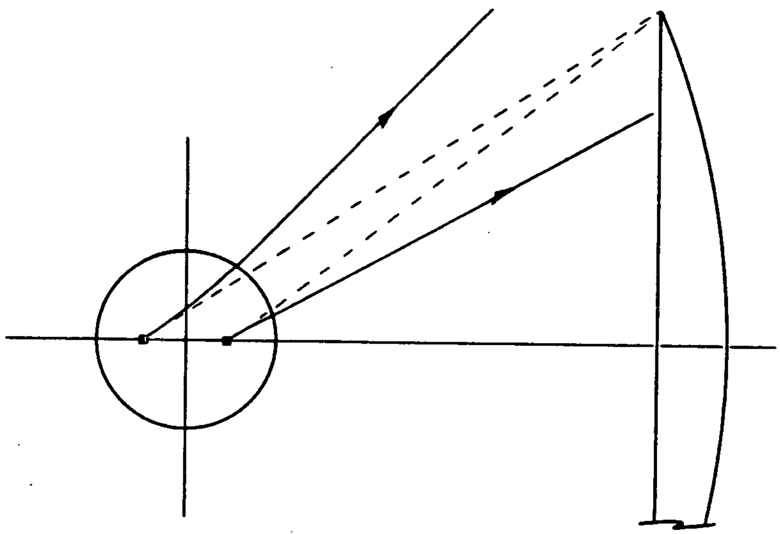

FIGURE 16

Refraction effects in the backscatter collection optics.

therefore be refracted away from the collection lens. This is shown by the solid line in Figure 16 and can be compared with the ray trajectory given in Figure 6. The dotted line in Figure 16, originating from the same point in the plasma, shows the path of the same ray if refraction were neglected. The result of refraction then is to decrease the effective collection cone for this region of the scattering volume.

On the other hand, the corresponding element of the scattering volume which is closer to the lens produces the red shifted spectral component and contributes to the signal with a collection cone that is increased as a result of refraction. In a first approximation, the amount of light lost from the 'far' side of the scattering volume will be gained from the near side so that the total amount of scattered light collected remains fixed. However, with the inclusion of refraction effects, one can see that it is possible for the plasma to produce a scattered signal that is dominated by the characteristics of the plasma nearest the collection lens.

The effects of refraction are considered at least a partial explanation for not seeing a blue shift. The most likely reason for observing only red-shifted spectra is that there is simply an error in imaging the scattering volume symmetrically about the plasma axis. Alignment of the scattering system was accomplished by placing a small pinhole at the precise geometrical location of the axis of the discharge vessel. The incident beam and monochromator entrance slits were then imaged on the center of this pinhole. However, considering that the scattering volume is only 2 mm in length, it is quite possible that the discharge itself was not so accomodating as to have the plasma axis correspond exactly to the geometrical axis of the vessel. For instance, if the plasma axis was displaced from the center of the focal volume, in the direction of the incident beam, by 0.5 mm, scattering from the far side of the plasma would constitute only 25% of the total signal.

Apart from some of the uncertainties in fully explaining the scattering observations, and, to the extent that the scattering experiments represent a radially averaged investigation of the plasma column, it will be seen in the following section that the plasma parameters determined from scattering agree very well with previous independent measurements.

6.3 Plasma Parameters for the Z-Pinch

Results for the plasma parameters obtained from the Thomson scattering experiments are shown in Figures 17 and 18. These give the plasma temperature and electron density respectively as a function of time during the pinch phase. Again, the time axis is referenced to $dI/dt = 0$. The smooth curves drawn on each plot represent a visual approximation to the data points.

Ion temperatures, Figure 17, were determined using a computer aided visual fitting routine to compare the observed backscatter spectra with theoretical profiles. The theoretical shape for the ion feature is calculated using Salpeter's (1963) approximation with $Z = 2$ for fully ionized helium and $T_e = T_i$. Over the range of plasma parameters measured, electron-ion collision times are in the sub-nanosecond regime so it is quite valid to assume equal electron and ion temperatures. When the shape of the backscatter spectrum is well defined, as in Figure 15(C) or (D), the fitting procedure allows the average ion temperature to be determined to an uncertainty of 10 - 20%. Below an electron density of approximately 1×10^{18} cm^{-3}, the backscatter spectra show rather poor signal to noise ratios (see Figure 15(B) for example). In these instances, temperature measurements become less accurate and are good to, at worst, about 40%.

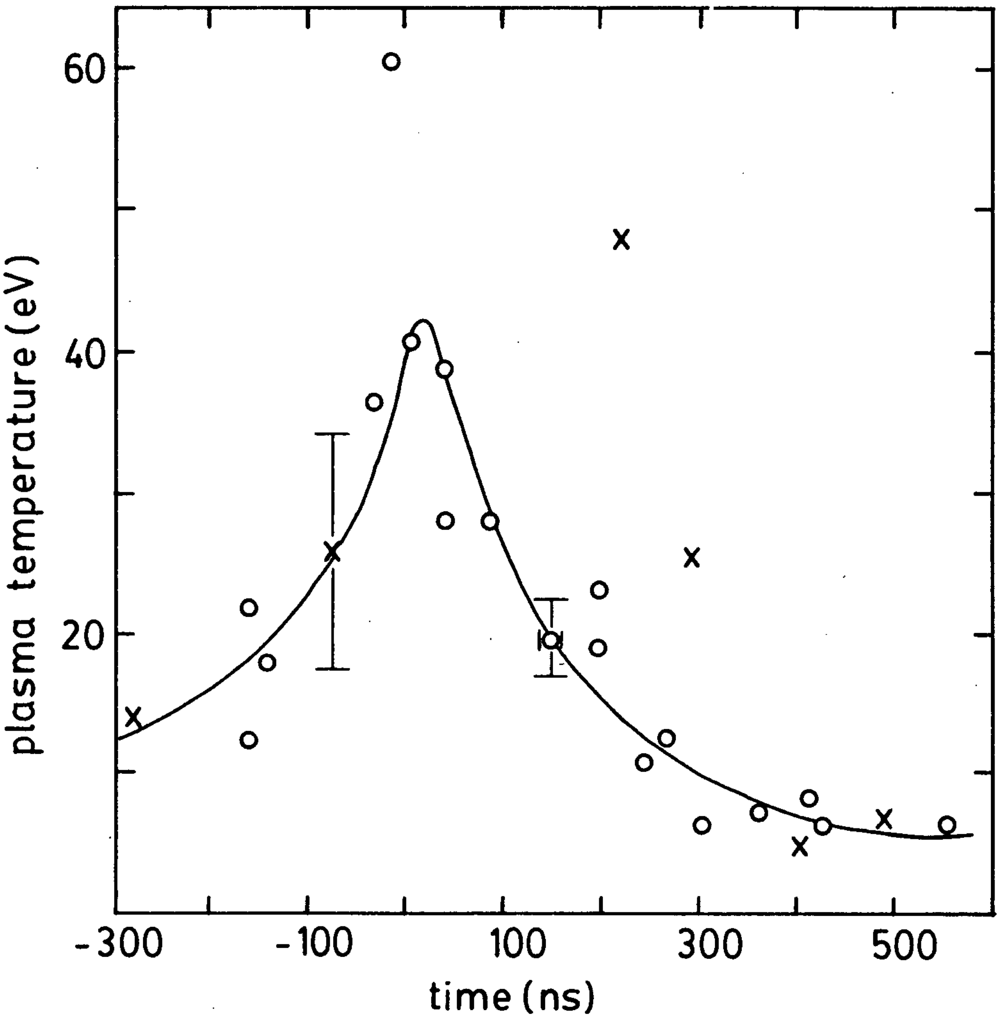

FIGURE 17

Plasma temperature results. Measurements are from Thomson scattering in the backward direction (open circles) and line to continuum ratios (crosses).

For comparison, the data points drawn as crosses give temperature measurements from earlier work, (Houtman, 1977; Albrecht, 1979; Hilko et.al., 1980). These estimates were based on the line to continuum ratio for the HeII 4686 Å emmission line. Above 25 eV, this spectral line is essentially non-existent since the plasma is fully ionized. However, the spectroscopic data below 25 eV is reliable and agrees favourably with the Thomson scattering results. Typical error bars have been indicated in Figure 17.

Electron density data, Figure 18, is obtained from both forward (open squares) and backward (open circles) scattering experiments. Using the Rayleigh scattering calibrations, n_e was computed from equation [15] with $S_i(k) = 2/3$. As shown in Figure 14, the scattering volume had an estimated length of 1.9 mm which, at times during maximum compression, exceeded the plasma diameter. When comparing Rayleigh and plasma scattering signals this discrepancy in collection volumes was accounted for.

Collective scattering, i.e.: an ion feature in the backward direction was not observed for densities below 2×10^{17} cm^{-3}. Density measurements at early times could be extended to $< 10^{17}$ cm^{-3} since the ion feature in forward direction still contained significant amounts of scattered light. During the high compression phase, Figure 18 shows apparently spurious data points with $n_e > 10^{20}$ cm^{-3} which originate from the forward scatter data. These and other off scale points are due to the large stray light enhancements discussed earlier. Accordingly, those measurements in the forward direction that indicate electron densities well in excess of

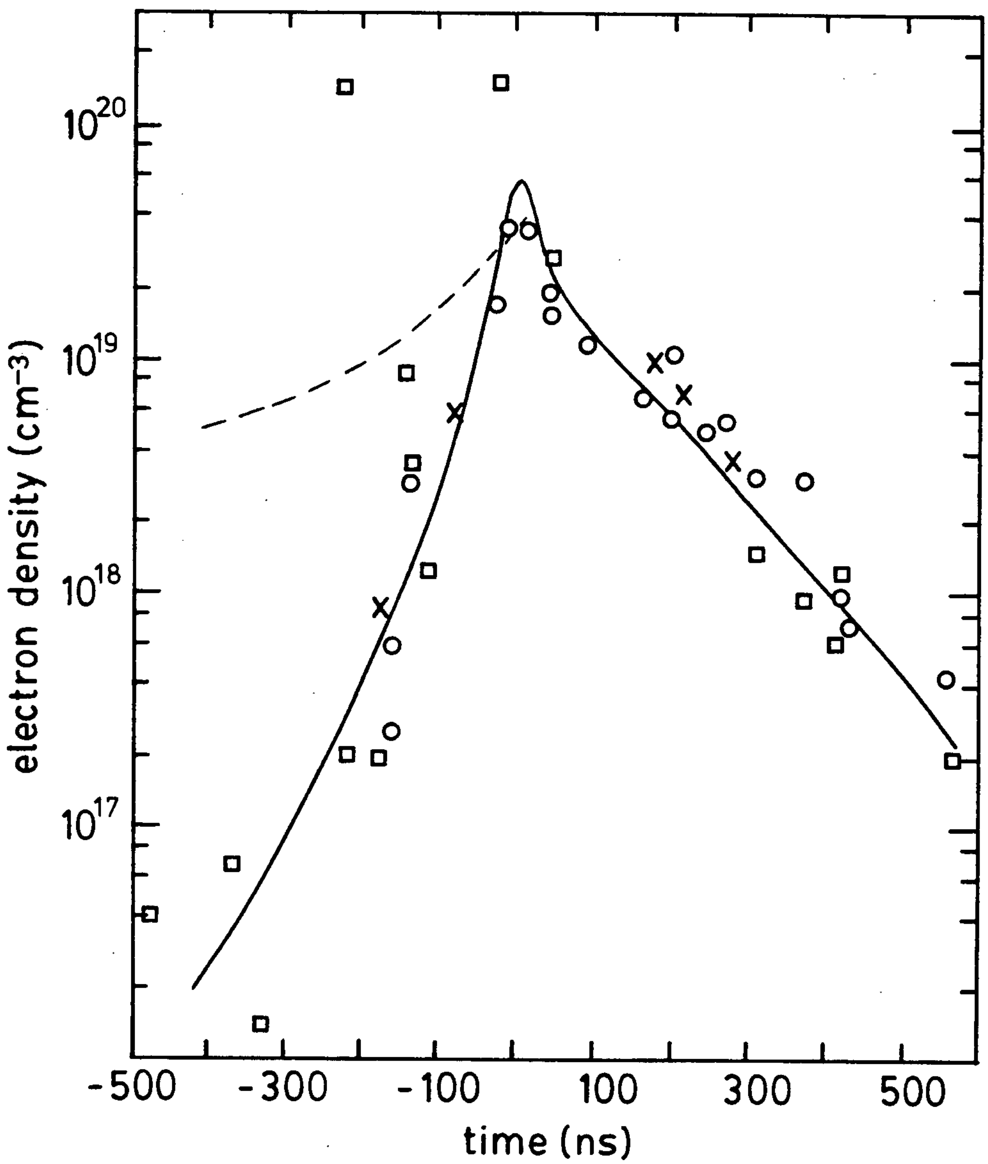

FIGURE 18

Electron density results. Measurements are from Thomson scattering in backward direction (open circles) and forward direction (open squares), and Stark brodening (crosses). The dotted line shows the snow-plow model prediction for Z = 2.

10^{20} cm^{-3} are not plotted in Figure 18. Again, the first density measurements on this Z-pinch were obtained spectroscopically and are included in Figure 18 as crosses. (Like the scattering geometry, the spectroscopic experiments had been arranged to view the on-axis plasma in a radial direction). The agreement between all three density determinations is quite good.

It is interesting to compare density measurements from Thomson scattering with the snowplow model of plasma collapse described in Section 3.4. Equation [1] specifies that the average electron density within the plasma column is determined by the column radius and assumes total sweep-up of the initial fill gas. The dotted line in Figure 18 shows the predictions of equation [1] for fully ionized helium with the outer radius as a function of time taken from the streak and shadowgram plots, Figure 7(A) or 7(B).

At peak compression, the scattering measurements and predictions from total sweep-up correspond completely because the averaging properties of the scattering system and the averaging properties of equation [1] also correspond. However, prior to peak compression, the plasma density on-axis is considerably lower than an internally uniform distribution predicts. The radial distribution of electron density is of course not uniform. Both the streak and shawdowgram studies show that most of the gas that is swept-up by the magnetic field remains confined within a relatively thin shell up until about t = -50 ns. Prior to this time, the plasma density inside the shell (that is, near the axis) will be comparatively low and the scattering experiments have more than adequate spatial resolution to show this clearly. The average electron density of the shell itself will closely follow the dotted line since at these times, the plasma radius is small compared with the size of the vessel so the amount of gas that remains to be collected up will contribute little to the electron density of the shell plasma.

This concludes presentation of the Thomson scattering diagnostics and the Z-pinch plasma parameters obtained by this method. The following discussion provides a brief review of some of the important aspects of he current scattering experiments.

The scattering results have verified previous spectroscopic measurements of the plasma parameters obtained for the pre and post-pinch phases of the discharge. Where spectroscopic (and other) diagnostics attempted previously have failed, scattering from ion acoustic fluctuations has proved to be a valuable method for extending measurement capabilities into the high temperature, high density phase. The plasma density and density gradients are sufficiently large to result in significant refraction at the ruby laser wavelength. This has introduced some problems with stray light. Spectrally resolved detection, as in the backscatter system, can aid in discriminating against stray light. However, in order to resolve the thermal ion spectrum in the forward direction, more efficient beam dumping will be required.

Two vital aspects of the scattering experiments have limited the detail with which the high compression phase could be investigated. Firstly, the current arrangement of the scattering systems has resulted in a lack of high spatial resolution. Consequently, the measurements have given only the average line-of-sight plasma conditions whereas the plasma temperature, density and radial velocity distribution within the scattering volume can be quite non-uniform. Secondly, the temporal resolution afforded by the q-switching process is insufficient to isolate some of the more rapid changes that occur during the on-axis collapse. Though these limitations are present, the scattering experiments, combined with the streak and shadowgram study, have contributed greatly to diagnosing the current z-pinch plasma.

The final experiment of this thesis work attempts to give a second independent measurement of the electron density with, as well, the specific goal of overcoming the temporal and spatial limitations of the scattering experiments, thus providing a more detailed view of the peak compression phase.

CHAPTER 7 INTERFEROMETRIC DETERMINATION OF ELECTRON DENSITY

7.1 Introduction

With scattering methods, the plasma is interrogated at the microscopic level via particle fluctuations. Such a technique is important for the interaction experiments since the CO_2 laser can be absorbed by coupling directly to specific fluctuations. Effects of the CO_2 laser can also be observed at the macroscopic level since localized disturbances will eventually decay in some hydrodymanic fashion. Therefore, in the next stage of diagnostic investigation, the Z-pinch is examined by measuring a macroscopic plasma parameter, namely, the index of refraction. This has been done using double exposure holographic interferometry. The interferometric measurements have given a complete two dimensional view of the plasma electron density distribution. These experiments then not only complement the scattering results with an independent measurement of n_e, but also dramatically improve spatial resolution.

The first section describes the major advantage of the double exposure holographic technique and why this method was selected over more conventional ones. Next, a simple approach to the formation and interpretation of the interference pattern will be given. However, the remainder of this chapter expresses a concern for the applicability of interferometric techniques to high density plasma, or in general, highly refracting phase objects. The problem results from the additional phase distortions introduced as a result of curvature in the ray paths. Though the calculations presented will show that refraction effects are not of primary importance for the current Z-pinch diagnostics, it has in fact been important to verify this. In particular, it is vital to point out that the currently used imaging arrangment may not be adequate for the proposed interaction experiments.

7.2 Double Exposure Holographic Method

Holographic interferometry covers a wide range of topics in optics and photographic processing (e.g. Collier et.al., 1971). A very recent and complete treatment of the theory, practice, and application of holographic interferometry can be found in the text written by Charles M. Vest (1979). No attempt will be made here to describe all aspects of the method, though relevant features of the techniques involved, as they apply to the current experiments will be pointed out where appropriate.

This first section illustrates the basic idea of the double exposure procedure and points out the most important difference between conventional interferometry and the holographic method, namely, that the methods are respectively differential in space or, differential in time. The consequences of this difference will also be discussed and it will be seen that the double exposure holographic technique offers a great deal of flexibility in the study of transient events.

The double exposure method is illustrated in Figure 19 which shows nothing more than a schematic arrangement for recording and reconstructing off-axis holograms of a transparent object. In Figure 19(a), the incident laser beam is split into two beams which travel different paths before being recombined, and the interference pattern is recorded on a photographic plate. One wavefront, designated the reference beam, has a spatially uniform (or at least simple) amplitude and phase distribution. This beam is used holographically to record the amplitude and phase distri-

(A) Recording

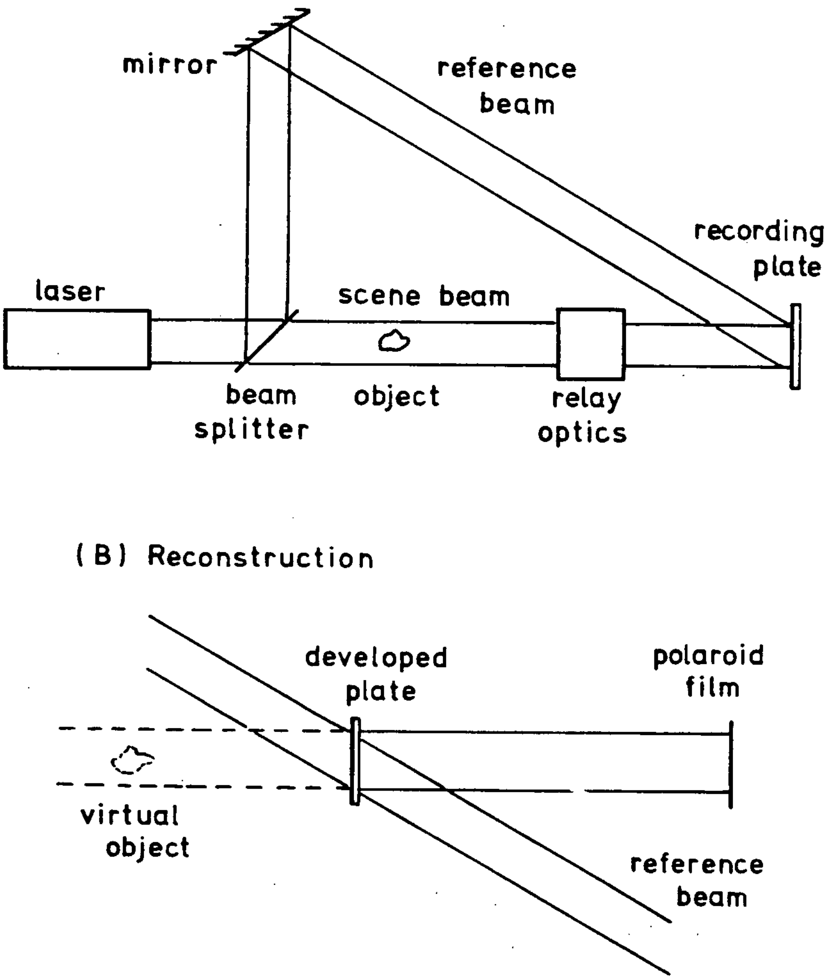

FIGURE 19

Illustration of the double exposure method.

bution of the second wavefront, the scene beam. Since the object under consideration is transparent, upon transmission through the object, only the phase distribution of the scene wavefront is altered while the amplitude distribution remains unchanged.

The scene beam also contains some unspecified relay optics. This could be a simple optical delay for matching the beam paths to the coherence length of the laser source, and/or a more complicated imaging arrangement allowing for say, magnification of the object wavefront onto the plate. Though not shown, the reference beam as well could contain similar beam handling or magnification matching components.

This system then is used to record two different scene beams on the same photographic plate. The first exposure records the wavefront of the scene beam when the object is not present, while the second exposure is made with the object in place. The two scene beams must therefore be recorded at different times. However, after development and processing of the plate, a single reference beam is used to reconstruct both scene beams simultaneously, as illustrated in Figure 19(B). Now, interference between the two reconstructed wavefronts can be observed and recorded. The difference between the (reconstructed) scene beams is due only to the presence of the object since all else in the scene beam path was identical for both exposures.

Examination of the two scene beams of Figure 19(B), from the point of view of the polaroid film, would lead to the conclusion that the interference pattern originated from a conventional Michelson or Mach-Zender interferometer with a transparent, phase distorting object in one arm. In this sense then, the double exposure holographic technique just described merely mimics all the usual interferometric methods except that the two wavefronts of interest are permanently recorded through holography and can be viewed at leisure. The most important difference though is that the interfering wavefronts in the double exposure method originate, not from different regions of space, but from different times. Conventional interferometry is just the opposite since the beams that interfere must be present simultaneously but travel through different regions of space. In the following brief discussion, the flexibility allowed by the interferometric studies which are differential in time are pointed out through the example of the current laser/plasma interaction experiments.

In the present experiment, the first exposure can be made before firing the Z-pinch discharge and the vessel contains low pressure helium. The second exposure can then be taken at various times during the pinch phase. Each exposure will last only for the duration of the laser pulse, which must of course be short enough that the plasma appears as a stationary object. The interference pattern produced will be entirely equivalent to that obtained in say a Mach-Zender configuration where the plasma is in one arm of the interferometer and there is a uniform refractive index distribution in the other arm. In this instance then, a holographic record of the wavefronts might only be considered an advantage because it allows some flexibility for subsequent image processing.

Using a short pulse laser for holographic interferometry allows for another possible exposure sequence. If it is arranged to have the time interval between exposures also very short, then both exposures could be obtained during the pinch phase. Then, only the change in plasma conditions which occurred in the time interval between exposures would be seen in the reconstructed interference pattern. One could therefore completely isolate rapid plasma motions from more slowly varying 'ambient' configurations (Armstrong, 1977). As an example, application of such an arrangement will be of particular importance in isolating effects of the CO_2 laser in the proposed interaction experiments since the CO_2 laser pulse will last for the order of a nanosecond or less, a time scale over which the target plasma is essentially stationary. However, the most often cited example of the temporal isolation advantage of double exposure holographic interferometry is when the ambient configuration contains rather poor quality optics, a circumstance which cannot be tolerated with conventional methods.

In any event, the above possibilities arise from the fact that the double exposure method is differential in time. For the present purposes, the first interferometric measurements were intended to extend the scattering results by examining the plasma configuration during maximum compression, that is, when the first exposure is made before firing the discharge. For this case, Section 7.4 gives a simple analysis of the formation and interpretation of the interference pattern. Before doing this though, the following short section establishes some data for the plasma refractive index as a function of electron density.

7.3 Plasma Refractive Index

The basic plasma property that is of interest for interferometry in the index of refraction which, in its simplest form (Jahoda, 1971) is related to the electron density through equation [2].

$$\mu(r) = (1 - n_e/n_c)^{1/2} \qquad [2]$$

The index of refraction depends on the wavelength at which it is measured, through the critical density, n_c, where:

$$n_c = 1.12 \times 10^{21}\lambda^{-2}\ \mathrm{cm}^{-3},$$

if the wavelength is given in microns. Using ruby laser light, $n_c = 2.33 \times 10^{21}$ cm^{-3}.

In terms of interferometric measurements, the refractive index differs significantly from unity when the electron density becomes the order of 1% n_c. For comparison, the plasma refractive index is smaller than unity by about the same amount that ordinary air is larger than unity, at an electron density of 0.05% n_c. This provides a more or less quantitative distinction between high and low density plasma, the current Z-pinch being in the former category.

In what follows later, the actual numbers involved may be of interest, so, as a matter of convenience and reference, Figure 20 is included here to show the plasma refractive index at the wavelength of ruby laser light.

7.4 Formation of the Fringe Pattern

This section gives a simple analysis of the generation and interpretation of the interference pattern produced when the effects of refraction are not important. As will be seen later, refraction effects, as well as generating a good deal more mathematical complication, will also introduce a more serious problem. The basic ideas presented here though will remain unchanged when refraction is included.

The pinch plasma is assumed to have a symmetric electron density distribution, $n_e = n_e(r)$ which does not vary along the plasma column, i.e.:

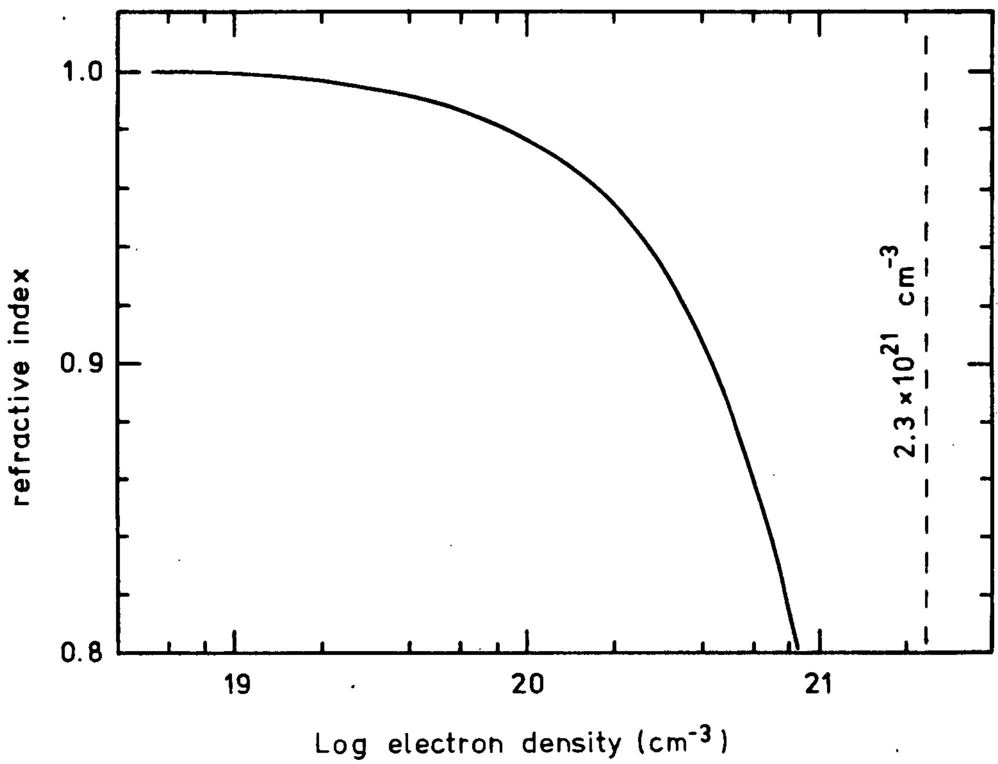

FIGURE 20

The plasma refractive index vs. electron density.

in the z direction. The plasma can therefore be replaced by its equivalent refractive index distribution according to equation [2]. In Figure 21, a cross-section of the plasma column is shown where $\mu = \mu(r)$ inside a maximum radius of r_o. For $r > r_o$, $\mu = \mu_o = 1$.

The plasma is illuminated by a collimated beam, entering parallel to the x-axis. Consider then the optical pathlength of a ray incident at height y. The light ray is assumed not to deviate from a straight line path. Ray curvature due to refraction effects is therefore ignored.

As a first or reference exposure, plasma is not present and the ray travels an optical path $l_o = \mu_o(x_B - x_A)$ in going from A to B. For the second exposure, the plasma is in place and the optical path from A to B is now l_1, where

$$l_1 = \int \mu(r)dx$$

evaluated over the limits x_A to x_B. The path difference $\Delta l = l_o - l_1$, between reference and scene ray can be expressed alternatively as a phase difference $\Delta\phi = 2\pi\Delta l/\lambda$ or, more appropriately, in terms of the number of wavelengths $P = \Delta l/\lambda$. (Lambda will be consistently taken as the vacuum wavelength.)

Upon reconstruction, the two wavefronts are present simultaneously and they will interfere. The interference pattern that is then produced will display contours of constant P, interference maxima occurring when P is integer while half-integer P correspond to minima. In the fringe pattern, the only directly measurable quantity is the fringe number P. The desired pathlength information is therefore obtained by simply counting fringes. Each fringe is located in the interference pattern and identified by its corresponding value of P.

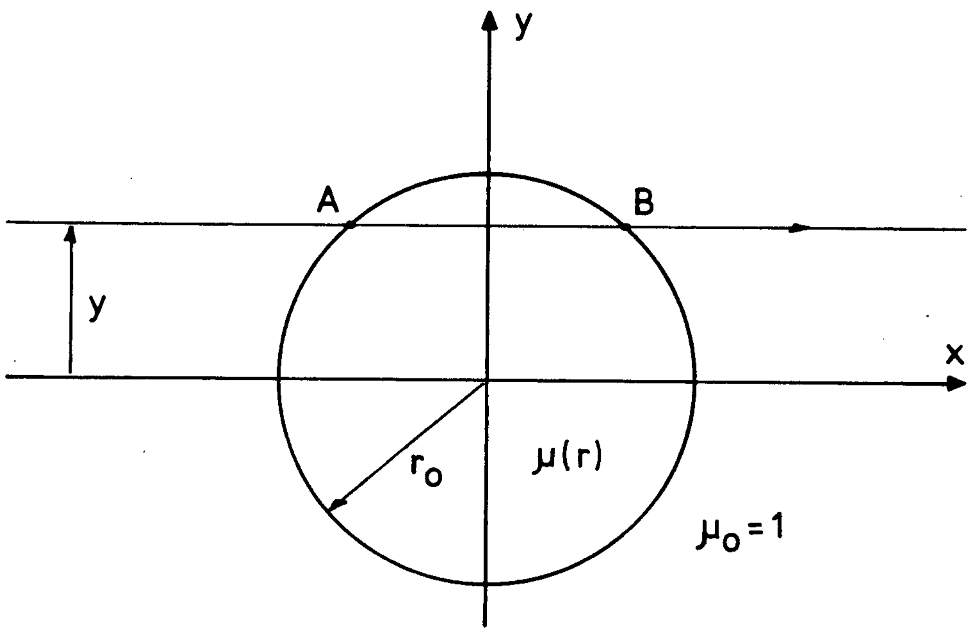

FIGURE 21

A ray path without refraction.

With the axisymmetric configuration of Figure 21, it is clear that the fringe number depends only on y

$$P(y) = \frac{1}{\lambda}\int_{x_A}^{x_B} (\mu_o - \mu(r))dx \ , \qquad [16]$$

whereas the refractive index is a function of the radial coordinate r. Equation [16] can be shown to be the Abel transform relationship between the observable function, P(y) and the line integral of the desired function $\mu(r)$. Standard numerical routines (e.g. Fan, 1975) can then be used to Abel invert the interferometric data to give the complete radial distribution $\mu(r)$ and therefore $n_e(r)$.

The analysis and equations leading to the distribution of fringes P(y) in the interference pattern is not so straight forward if ray refraction is taken into account. In particular, Abel inversion is no longer strictly valid since this assumes explicitly that the ray paths are straight lines. However, without this assumption the unfolding of interferometric data becomes an extremely lengthy and complex procedure, and, in fact, the data can be ambiguous enough to make interferometry an unsuitable diagnostic. In the following section, the problem of ray refraction in an axisymmetric object is outlined and the assumption of straight line paths is considered in order to illustrate the care which must be taken when performing interferometry on highly refracting objects.

7.5 The Problem of Imaging

In order to help reduce the effects of refraction, wavefronts are recorded by using a lens or system of lenses to form an image of the object directly on the photographic plate. This is of course a more or less obvious approach to the problem of refraction, depending on how the actual imaging process is viewed. From the point of view of interferometry, only the phase relationship between reference and scene ray, at a given point in the object, is of interest. By producing an image of the object, a lens acts to restore the original phase relationship, independently of the directions the two rays may have left the object point in question. One can then see the necessity of using some imaging element when refraction cannot be neglected.

The basic question to be considered in this section can be stated as follows. Given an axisymmetric refractive index distribution, where, in relation to the object, must the image plane be located in order to neglect the effects of refraction when analyzing interferometric data? This question is clearly related to the present Z-pinch investigation, but it is of considerably more general interest. For example, in virtually all laser/plasma experiments the focal volume of the laser is cylindrical or conical. The plasma contained in the focal volume can therefore be described in an axisymmetric coordinate system. Equally important is that such plasmas have high electron densities and are therefore strongly refracting objects.

This question has been addressed, in part, by Vest (1975) who has shown that ray curvature effects can in fact be neglected if the plasma axis (the plane $x=0$ of Figure 21) is imaged. Then, Abel inversion of the fringe data, based on the assumption of straight line paths, will yield the correct distribution $\mu(r)$ to within a few percent. This result was shown to be valid even for very extreme cases of refraction by axisymmetric objects. However, only the image plane located precisely on the axis of symmetry was examined. In order to obtain a more complete picture and therefore gain a better understanding of the true limitations of Vest's results, it was felt that consideration should be given to other image planes, particularly in view of the fact that it may not always be possible to know before hand where precisely the plasma will be located. (Based on the earlier discussions of the Thomson scattering results, this possibility has indeed shown itself to be quite real in the present diagnostic experiments.) In the following description it will be shown how various image planes have been analyzed.

Figure 22 depicts again an axisymmetric refractive index distribution $\mu = \mu(r)$ extending to a radius R_o, beyond which the refractive index is unity. The probe beam is collimated and enters from the left, parallel to the x-axis. A photographic plate, used to record the wavefronts, is imaged into the object at the plane $x = x_{image}$.

In the presence of the object, one ray of the probe beam is shown entering the distribution at a height $y = B$ and travelling the refracted path CD. This ray leaves the object at an angle ψ with respect to the x-axis. In the discussion of refraction angles in Chapter 3, the differential ray path was given in cylindrical coordinates by Bouguer's formula:

$$\frac{dr}{d\theta} = \frac{r}{B}(\mu^2 r^2 - B^2)^{\frac{1}{2}} , \qquad [3]$$

and the angular deviation can then be determined (Schreiber, et al., 1973) as:

$$\psi(B) = 2\cos^{-1}(B/R_o) - 2\int_{r_m}^{R_o} (dr/d\theta)^{-1} dr . \qquad [17]$$

The lower integration limit is the inflection point of equation [3], where the derivative is zero. To avoid additional complications to this description, it will be assumed that there is only one such stationary point with-

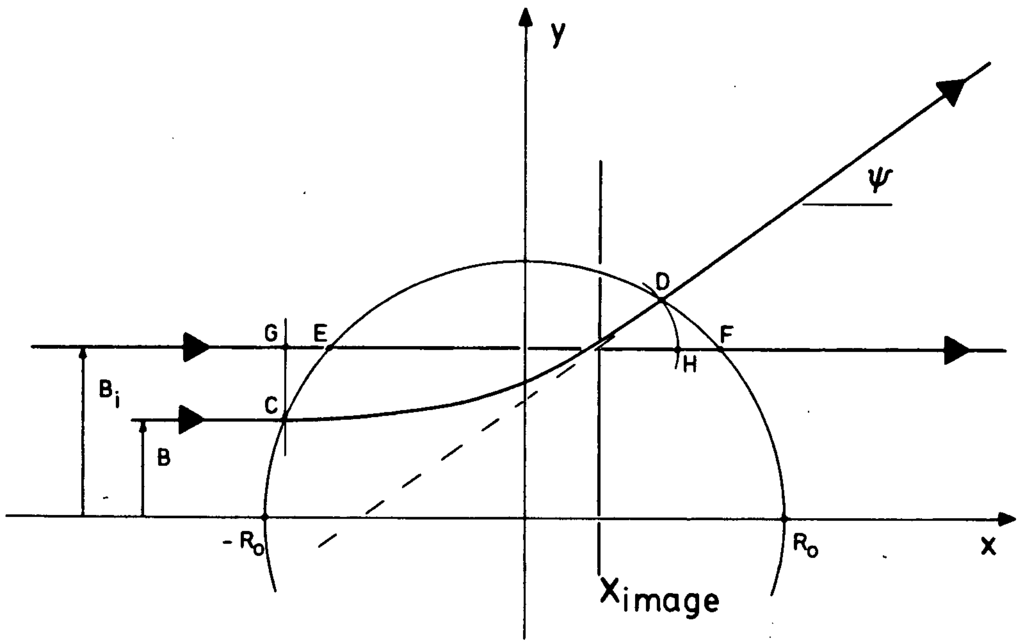

FIGURE 22

Imaging in a strongly refracting plasma.

in the distribution. The equations presented here can be easily extended, if desired, in a piecewise fashion, to include more elaborate distribution functions.

Now, when the ray in question, namely the scene ray, exits the distribution, it travels a straight line path $dy/dx = \text{const.} = \tan\psi$. Extrapolating backwards, this scene ray intersects the image plane at a height $y = B_i$. When the reference exposure is taken, the object is not present and the ray which will interfere with the above scene ray is just that reference ray which also intercept the image plane at height $y = B_i$. This reference ray is shown in Figure 22 travelling parallel to the x-axis along the path GEHF.

The reference and scene rays of Figure 22 will interfere according to their relative phase, or optical path difference, at the photographic plate. To determine the path difference, consider first the scene ray which, inside the distribution, travels an optical pathlength L given by the integral of $\mu(r)ds$ from point C to point D. Here, ds is an incremental arc segment along the refracted path. In cylindrical coordinates

$$
\begin{aligned}
(ds)^2 &= (dr)^2 + (rd\theta)^2 \\
&= (dr)^2\left(1+r^2(d\theta/dr)^2\right) .
\end{aligned}
$$

Using equation [3] and the assumption that the distribution is symmetric about the stationary point gives:

$$
L = 2\int_{r_m}^{R_o} \frac{\mu^2 r dr}{(\mu^2 r^2 - B^2)^{\frac{1}{2}}} \quad . \qquad [18]
$$

The reference ray path to be compared with L is found by first noting that both reference and scene rays can be considered in phase at the points G and C respectively. Secondly, on the exit side of the distribution, the curve through points D and H is a circular arc centered at the apparent point of origin of the two rays. Through an ideal imaging system, both rays will travel the same optical path from D or H to the recording film. Therefore, the optical path difference between the reference and scene rays shown will be:

$$\Delta = \mu_o \overline{HG} - L \, . \qquad [19]$$

The interference pattern observed will display contours of constant delta, and the interferogram is analyzed by simply counting fringes. For the experiment depicted in Figure 22, the measured distribution of fringes in the image plane will be called M, where:

$$M(y) = \Delta(y)/\lambda \, . \qquad [20]$$

Because the refractive index distribution is axisymmetric, M and delta are indicated explicitly to be only a function of the y coordinate in the image plane. Implicitly though, M is understood to be also a function of x_{image}, the location of the image plane. Given a specific refractive index distribution, equations [3], and [17] to [20] allows the fringe function M to be calculated for any desired image plane.

The question being asked here can now be restated as follows. How does the observed function M(y) differ from the fringe function P(y) in equation [16], where P(y) is calculated on the assumption that no refraction takes place? If P and M differ significantly, then Abel inversion of the observed data will not yield the correct refractive index distribution.

As the equations involved are not very amenable to analytical investigation, they have been solved numerically, with the observed and assumed functions, P and M, being compared in the following manner.

The image plane is divided into N evenly spaced values of y, with the spacing given by y_{max}/N, where:

$$M\ (y \geq y_{max}) = 0.$$

Depending of course on the image plane chosen, the observed fringe pattern will extend out to at least $y_{max} = R_o$. Also, for each of the N y-coordinates in the observed pattern, the straight line fringe function, P(y) is calculated. The measured and assumed fringe patterns are determined to differ by an amount:

$$\sigma = \frac{1}{P(0)} \left[\sum_{i=1}^{N} \{M(y_i) - P(y_i)\}^2 / N \right]^{\frac{1}{2}} . \qquad [21]$$

With the majority of the calculations that were performed, sigma was essentially invariant for $N > 10$. However, for those results presented here, N = 50 was used to ensure a completely representative sampling. The normalization factor $P(y = 0) = M(y = 0)$, makes sigma independent of the actual size of the refractive index distribution, so that equation [21] can be used as a basis for comparing a large variety of experiments.

Several functional forms for the refractive index distribution were examined. As a typical example, equation [21] will be presented using the following parabolic function:

$$\begin{aligned} \mu(r) &= 1 - \varepsilon(1-r^2) \quad &, r < 1 \\ &= 1 &, r > 1 . \end{aligned} \qquad [22]$$

Figure 23 displays several curves of constant sigma, given as a function of the refractive index on-axis and the location of the image plane. The axis of symmetry for the object is located at $x = 0$, as indicated in Figure 22. Given the refractive at $r = 0$, Figure 23 shows that the error introduced by assuming straight line paths will increase as the image plane is moved increasingly farther behind ($x < 0$), or in front ($x > 0$) of the axis. As well, for a particular maximum error, the allowed latitude in locating the image plane decreases very dramatically as the refractive index begins to deviate from unity. A not so extreme example (Sweeney, et al., 1976) might be that, if, at $\mu(r = 0) = 0.8$, the average error in the observed fringe pattern is to be less than 5%, then the image plane must be located within the object with a precision of better than $\pm$ 1/10 the diameter of the object.

It will be noted also that in Figure 23, the apparent optimum image plane is located just in front of the axis, at a slightly positive value of x. However, the image planes being considered are the image locations in vacuum. When the object is in place, it will, in the present case, act like a diverging lens and displace the vacuum image more towards the axis. Thus, the combined effect of the 'plasma lens' and external lens results in an image of the axis of symmetry. On the other hand, if the object considered had a refractive index always larger than 1, that is, $\varepsilon < 0$ in equation [22], the apparent optimum image plane would be slightly negative.

There are two aspects of equation [21], as presented in Figure 23, which should be kept in mind. Firstly, Figure 23 indicates only the average error introduced in the observed fringe pattern when it is assumed that the pattern has been generated by unrefracted rays. Specific areas of a given fringe pattern will show deviations that can be significantly more severe, particularly in regions where the gradients that must be traversed are very steep. Secondly, though the parameter sigma is a natural choice for comparing the fringe patterns $M(y)$ and $P(y)$, critical examination of the straight line path assumption must ultimately be performed on the desired function $\mu(r)$. However, from an experimental standpoint, the basic observable is only $M(y)$. Since the Abel inversion process can be viewed as a weighted

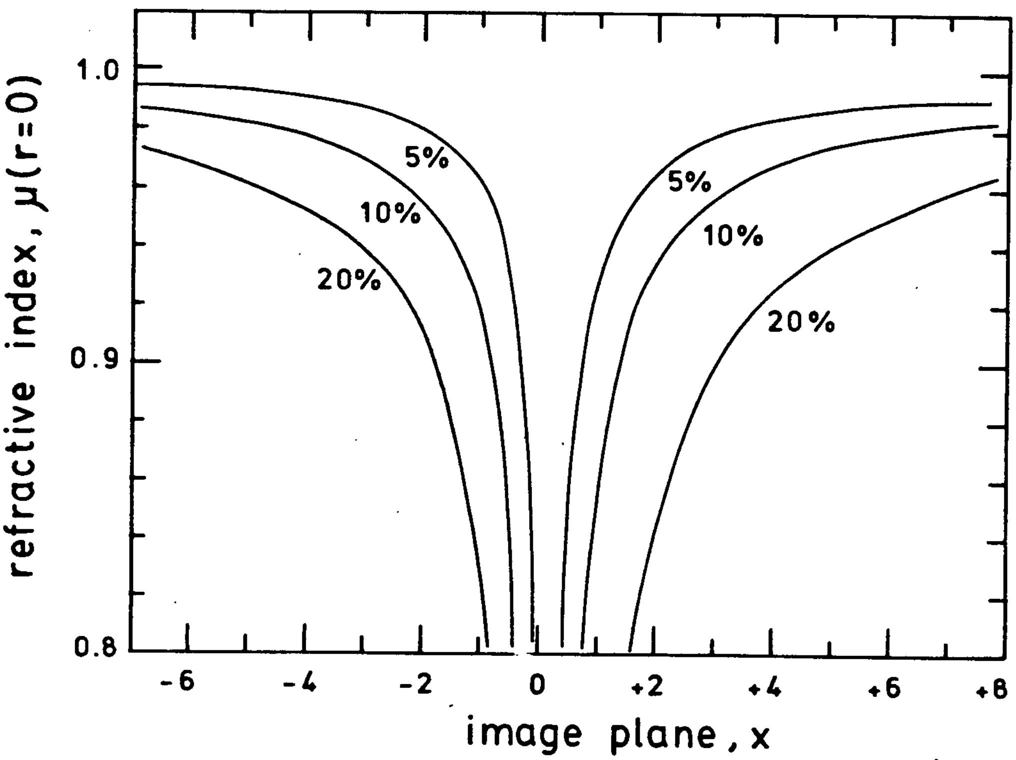

FIGURE 23

Errors introduced in an interferogram by assuming straight line paths.

integration over the slope of the fringe function, it may be more appropriate to make comparisons based on the derivatives of M and P, rather than on the functions themselves.

The problem of imaging in highly refractive objects is a nontrivial one and has yet to be solved in any generally satisfactory way. The calculations that have been shown here do, however, give a better indication of the limitations of interferometry as a diagnostic for high density plasma. For the present Z-pinch diagnostics, the minimum refractive index on axis will be in the range 0.99 to 0.98. Since the Z-pinch plasma has a size the order of a few millimeters and can currently be located with about this precision, Figure 23 shows that these investigations will not be dominated by imaging considerations. The following chapter describes in detail the complete experimental arrangement used to perform interferometric measurements on the Z-pinch plasma.

CHAPTER 8 LAYOUT OF THE INTERFEROMETRIC EXPERIMENT

8.1 Introduction

The light source for producing interferograms is again a ruby laser. Operating the laser in Q-switched mode produces exposure times in the 20 to 30 ns range. However, the electron density can change significantly over the duration of a Q-switched pulse so that the plasma cannot always be considered stationary. The effect of plasma motion during an exposure will be to smear out the interference pattern. Though interferometry was attempted with a Q-switched pulse, the results were not satisfactory. The first section in this chapter shows a simple ruby laser oscillator that uses cavity dumping generating much shorter light pulses. The remainder of the chapter outlines many pertinent details of the rest of the experimental arrangement including the optics of the scene and reference beam paths as well as photographic processing and reconstruction data.

8.2 Cavity Dumping of the Laser Oscillator

The idea and theory of laser cavity dumping was first presented by A. Vuylsteke (1963). Since then, many different arrangements have been used to extract short duration light pulses from a laser cavity (Siegman, 1973; Hamal, 1978). Here, a very simple scheme is used and the essential aspects of the procedure can be described with the aid of Figure 24. The upper portion of this figure shows the current arrangement of components in the oscillator cavity.

The rear mirror is 100% reflecting while the previously described etalon remains as a front mirror. PC1 and PC2 are pockels cells and the polarizer is calcite in a Glan-Thompson arrangement. Without PC2 present,

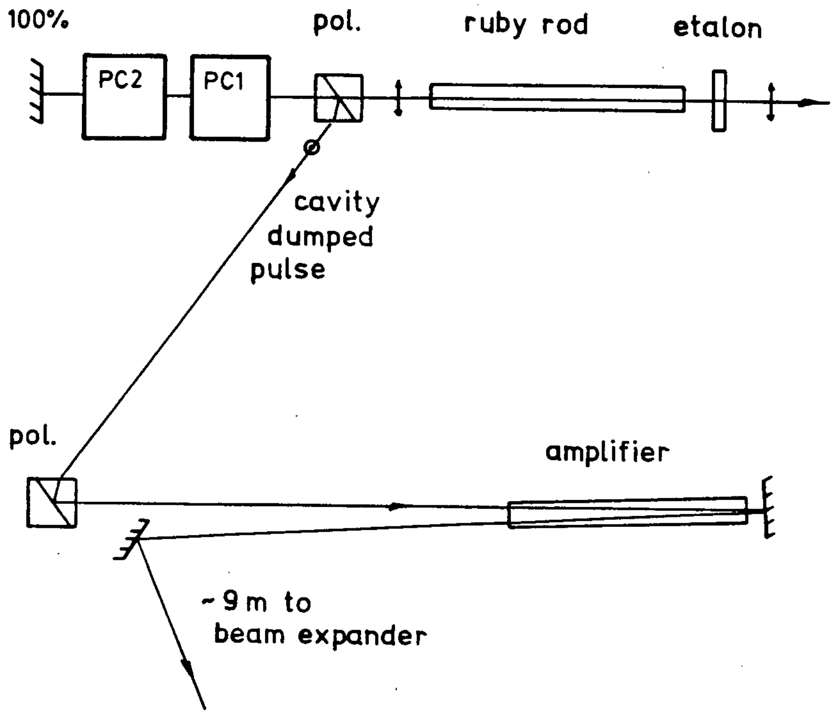

FIGURE 24

Oscillator and amplifier sections of the cavity dumped laser.

the cavity appears as a conventional Q-switched oscillator. PC1 and the polarizer provide the Q-switching action. PC2 is placed inside the cavity and, with no voltage applied, it behaves merely as a passive, freely transmitting component.

Initially, the quarter wave rotation voltage is held on PC1 while the ruby rod is pumped. At maximum inversion the voltage on PC1 is dropped to zero, now rendering PC1 also freely transmitting. This initiates build-up of the Q-switched pulse. In Figure 24, the preferred polarization inside the cavity is in the plane of the page. However, when the photon density inside the cavity is maximum, the quarter wave voltage is applied to PC2. Photons which now double pass through PC2 will have their polarization rotated by 90° and be reflected or dumped by the polarizer.

The time it takes to dump all light from inside the cavity is determined purely by the cavity transit time. If n is the average refractive index, L the distance between front and rear mirrors, and c is the speed of light, then the cavity dumped pulse will have a total duration of $t \simeq 2\ nL/c$, approximately twice the mirror-to-mirror transit time.

Currently, $nL \simeq 75$ cm giving a pulse width of about 5 ns. This is a considerable improvement over the Q-switched pulse duration. However, the cavity length need not limit the pulse width since PC2 can be supplied with a voltage pulse that is shorter than the double transit time. The simplicity of cavity dumping makes it quite an attractive method for generating pulses in the 1 to 10 ns range.

In order to extract high energy pulses by cavity dumping one would normally consider replacing the etalon with a second 100% reflecting mirror. The etalon here provides longitudinal mode selection to improve the temporal coherence length of the laser. Light coupled out through the etalon, though representing a significant fraction of the available energy, is simply rejected.

The lower portion of Figure 24 shows the remainder of the ruby laser system, which is simply a double pass amplifer stage. The only odd component here is a second calcite polarizer used to steer the beam through the amplifier. The reason for this is one of experimental convenience. The entire optical system is aligned using the beam of a low power Helium-Neon laser. In the cavity dump direction, light does not leave the first calcite polarizer normal to the exit face. Consequently, the alignment beam and ruby laser beam exit the oscillator cavity at slightly different angles. Dispersion data for calcite (Machewirth, 1979) shows this difference to be approximately 0.05°. The second polarizer compensates for the dispersion of calcite, allowing the whole experiment to be aligned with the He-Ne laser.

8.3 Optics of the Beam Paths

After leaving the amplifier, the ruby laser has a beam diameter of approximately 2.5 mm. Natural divergence over a 9 m path increases the beam diameter to about 6 mm. A final x4 beam expander, with a focal plane pinhole, is used to filter and collimate the beam for interferometry. Figure 25 shows a partially simplified version of the remainder of the interferometer optics.

Passing the beam through a 50% reflecting mirror provides equal amplitude reference and scene beams. The scene beam is directed radially into the discharge vessel. A system of three lenses produces an image of the plasma axis on the photographic plate, with a total magnification of x3.5. The photographic plate itself is housed in a light tight box indicated by the dotted rectangle in Figure 25. The angular acceptance of the imaging optics is limited by lens L1 to a full cone angle of 7.2° or F/8.0.

In the reference arm, lens L2 focusses the reference beam through a spatial filter pinhole P1. The beam subsequently expands freely to strike

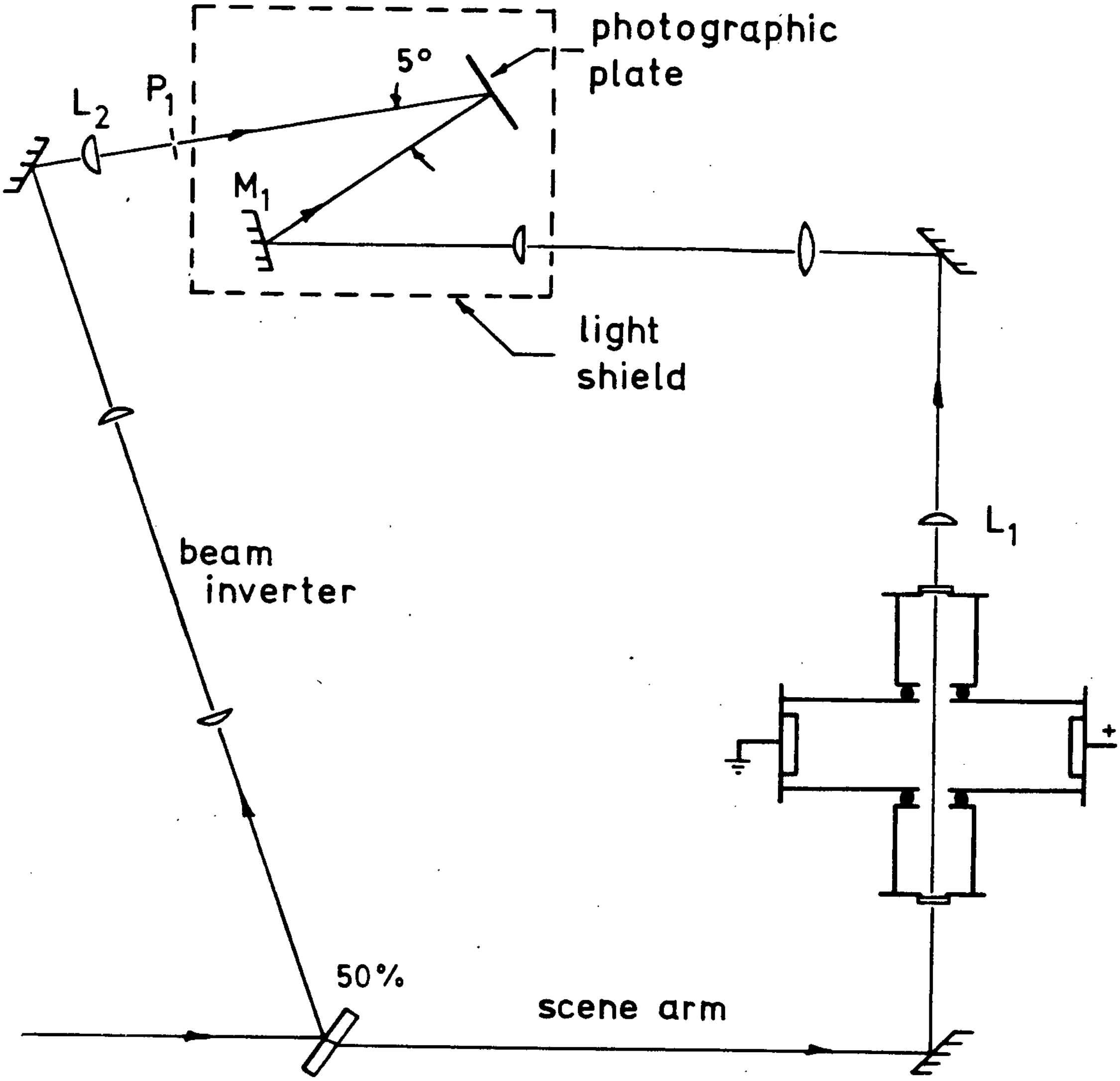

FIGURE 25

Optics of the interferometry experiment.

the plate at an angle of 5° with respect to the scene beam. Two other lenses in the reference arm serve simply to invert this beam so that the recombined wave fronts have the proper spatial orientation with respect to each other.

Even with the provisions for beam filtering, the spatial coherence of the laser was not particularly good. Lense L2 was chosen to expand the reference beam by exactly the same amount as the scene beam. Then, by adjusting mirror M1, both beams could be precisely overlaped on the plate. Lack of spatial coherence was therefore not a problem. Considering temporal coherence, both beam paths are matched to within 5 to 10 mm over the 8.5 m distance from beam splitter to plate. This matching was sufficient to produce good quality fringes.

8.4 Recording and Post Exposure Processing

The wave fronts are recorded on Kodak type 120-02 high resolution holographic plates. This 0.006 mm thick emulsion has a contrast index between 4 and 6 (depending on development time) and requires an exposure of about 300 ergs/cm^2 at 7000 Å to produce a developed density D = 1.0. After both exposures are made, the plates are processed in the standard recommended fashion using D-19 for 5 minutes as the developer stage.

Many of the photographic emulsions available for holography have high contrast, making them very sensitive to variations in exposure. Because of this, and since the ruby laser intensity can fluctuate by 50% or more from shot to shot, exposures are biased towards the heavy side to ensure that each shot gets fully recorded. After development, the plates have a density usually ranging from 1 to 4. The final step before reconstruction then is to bleach the emulsion using a simple, dry, bromine vapour method (Graube, 1974).

The procedure of heavy over exposure and subsequent bleaching is quite standard in holographic interferometry. This is because one is interested in producing high contrast fringes rather than recording linearity. As well, bleached holograms have very high diffraction efficiencies (Chang, 1970). This greatly facilitates both alignment of the reconstruction optics, and photographing of the interference pattern.

When recording the holograms, the plate itself was imaged onto the plasma axis to eliminate refraction effects. In order to maintain this feature in reconstruction, the interference pattern must be recorded at an image of the plate. Reconstructions of the wave fronts are obtained using helium-neon laser light and a simple, single lens imaging arrangement. The helium-neon laser serves as the original reference beam and the plate is illuminated from the emulsion side, as was done during the recording process. Using only the first order transmitted light (corresponding to the original scene beams), the plate, and therefore plasma axis, is imaged onto ordinary polaroid film. High resolution film is not required to record the interference pattern since the lens allows the plate image to be magnified as desired.

CHAPTER 9 RESULTS FOR THE Z-PINCH PLASMA

9.1 General Features of the Interferograms

This section presents a qualitative interpretation and discussion of the fringe patterns that were observed. The first exposure was made prior to firing the discharge. The second exposure, made at various times during the pinch phase, is again referenced in time to the dI/dt trace. A few reconstructed interference patterns are shown in Figure 26. The circular field of view represents the holes (1.9 cm diameter) in the discharge vessel. The z-axis of the discharge vessel corresponds to a left to right diameter of these circles.

If the plasma had perfect cylindrical symmetry, the fringes would be straight lines running parallel to, and symmetrically centered about the discharge axis. This is clearly not the case here. Each photograph displays quite a complex two dimensional structure. This lack of symmetry is introduced into the plasma column during the formative stages of the discharge, when current is flowing along the interior wall of the vessel. In the vicinity of the access ports, there is of course the physical perturbation of the holes in the vessel. Along with this, there is a complex distortion of the magnetic field configuration since there are also holes in the outer return conductor.

The interferometric experiments were performed using a vessel with four holes, two for the diagnostics and two for the CO_2 laser. In Chapter 2 it was pointed out that these holes constitute a significant fraction of the circumference of the vessel so that complete rotational symmetry of the plasma column was not expected. However, the severity of the distortions could not be predicted and there was some hope that the symmetry would not

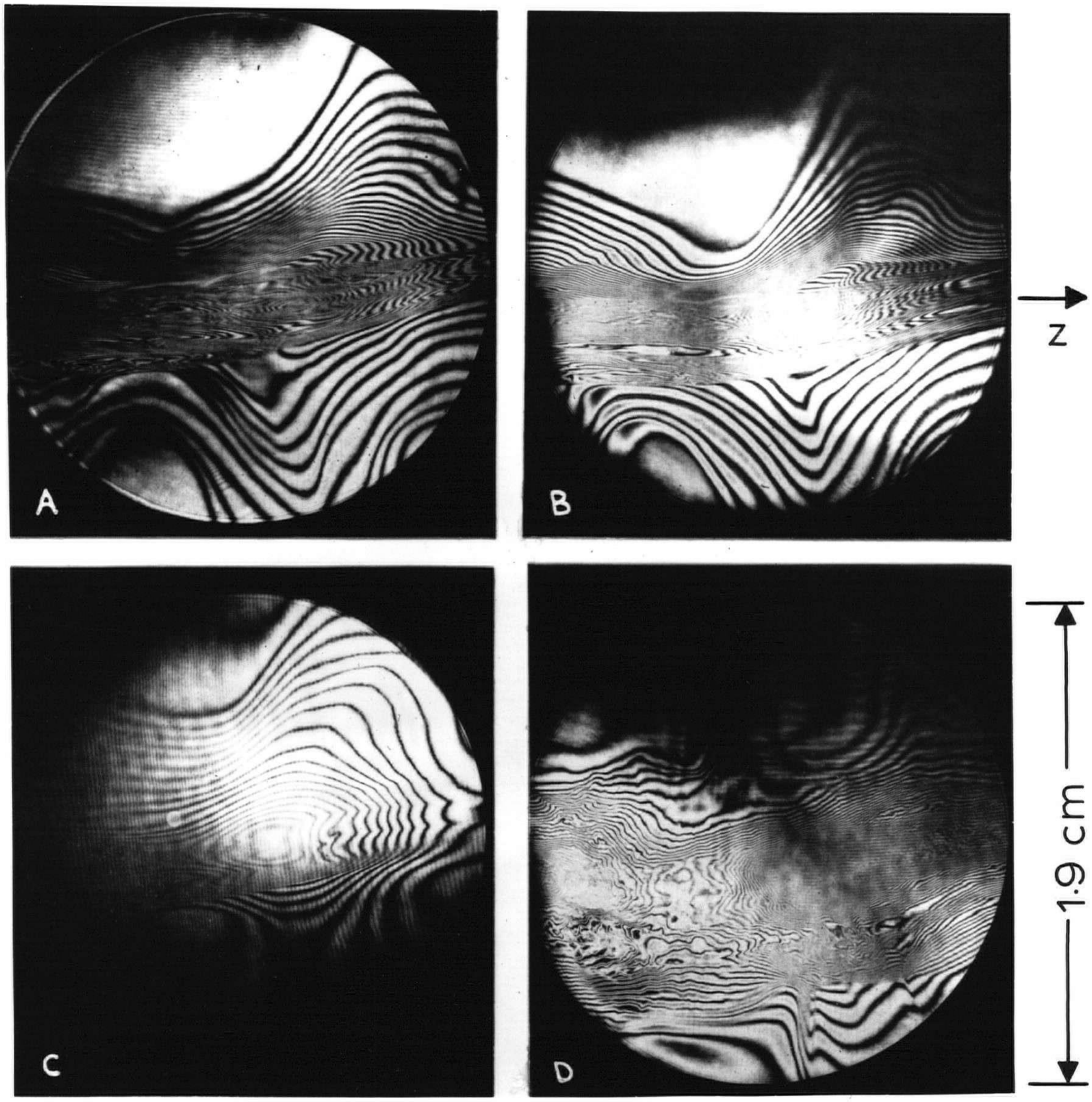

FIGURE 26

Samples of the interferograms obtained near peak compression. The observation times are:

(A) t = -31 ns,
(B) t = -30 ns,
(C) t = -90 ns, and
(D) t = +85 ns.

be degraded to the extent seen in Figure 26. For comparison, the shadowgram photographs shown in Figure 5 were obtained using a discharge vessel having only the two diagnostic ports. With only two holes in the vessel, the plasma symmetry is well preserved.

Apart from the lack of symmetry, formation of the plasma from shot to shot is quite reproducible. This is best illustrated in Figures 26(A) and 26(B), which were both taken at identical times t = -30 ns. In the low density regions, outside the plasma core, the fringes are broad and widely spaced. In these regions of the plasma, both fringe patterns are remarkably similar in terms of spacing, number, and contour of the fringes. Interferometric measurement techniques are characterized by their high sensitivities so that, relatively small variations in the plasma distribution would be apparent in the fringe pattern. As a very rough guide, the average electron density changes by about 1×10^{17} cm^{-3} in going from a maxima to the adjacent fringe minima.

Similarities between the fringe patterns of Figures 26(A) and (B) extend into the more dense regions of the plasma core. Though the fringes here are closely spaced and difficult to see in these reproductions, there is a considerable degree of correspondence between structural details of the two interference patterns.

Near the time of maximum compression (again Figures 26(A) and (B)), the interferograms often do not show a clear fringe pattern throughout the vicinity of the plasma axis. Lack of fringes near the axis is primarily the result of refraction of the probe beam. Though it remains true here that ray bending will be compensated for since the interfering beams are recombined at an image of the plasma axis, the imaging system must be able to collect all refracted light. The current optics has an acceptance cone of F/9 which is not small enough to collect those rays passing through the strongly refracting regions of the core.

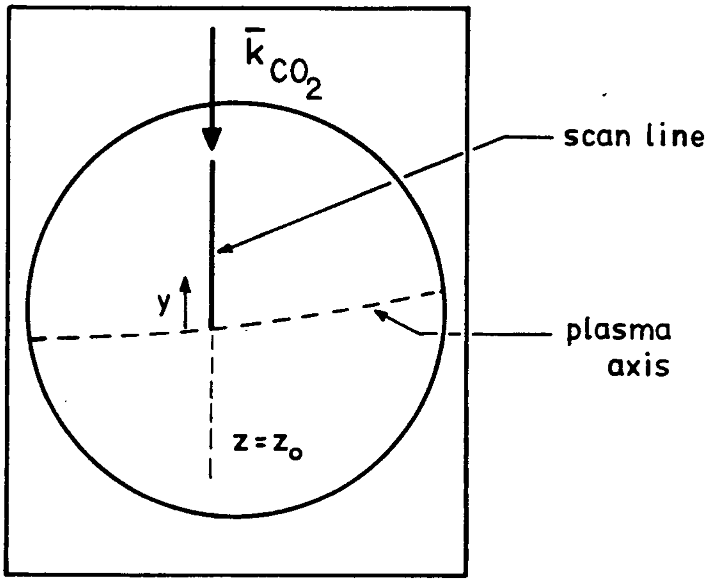

FIGURE 27

Illustration of the region for which interferograms were analyzed.

Though refraction is at least partially responsible for missing fringes in the core region, motional blurring may still be a contributing factor. The following estimate indicates that the fringes can also be smeared out during a 5 ns probe pulse.

A ray travelling through the plasma column can be assigned a fringe number P given by equation [16]. If the ray travels along a diameter of the plasma, and, only the first order expansion of the refractive index (equation [2]) is used, P will be given by:

$$P = \frac{1}{\lambda} (nr/n_c) \ , \qquad [23]$$

where n is the average electron density within the column, radius r. Both n and r vary with time. Equation [1] suggests that, if the particle inventory is fixed, n and r do not change independently of one another. When r decreases, n increases so that P tends to remain constant, though this cancellation effect is not quite complete.

Over an exposure time of Δt, the fringe number will change by ΔP. Assuming n and r are related according to equation [1], then, differentiating equation [23] with respect to time results in:

$$\Delta P \simeq \frac{1}{\lambda} \frac{n}{n_c} \left(\frac{dr}{dt}\right) \Delta t \ .$$

Chapter 3 gives $dr/dt = 1 \times 10^6$ cm sec^{-1}. As a worst case estimate, the maximum average electron density is 4×10^{19} cm^{-3}. Taking these figures with $\Delta t = 5$ ns gives $\Delta P \simeq 1.2$.

Negligible motional blurring would require $\Delta P \ll 1$. This condition is well satisfied during much of the pinch phase. However, near maximum compression, the above estimate shows that the effect of a finite exposure time cannot be neglected as a possible factor contributing to the absence of well defined fringes.

At early times, as in Figure 26(C), the plasma is much less dense, and has correspondingly weak density gradients. Plasma motion and refraction are therefore completely negligible and fringes can be observed throughout the plasma column. Figure 26(D) has been included for completeness and shows an interferogram that was taken well after peak compression. This photograph corresponds to the shadowgram of Figure 5(B) where the plasma has blown apart in a rather turbulent fashion.

9.2 Data Processing

Quantitative analysis of the data requires that the fringe function P(y) in equation [16] be determined from the interferograms. Each interferogram corresponding to a different time in the pinch phase. Once found, P(y) was Abel inverted using the numerical routine described by Fan (1975), and the electron density distribution $n_e(r)$ is obtained.

Clearly though, complete analysis of each interference pattern is quite a formidable task since (i) there are a very large number of fringes, (ii) the perturbations produced by the access ports have given an additional z-dependence to the plasma distribution, and (iii) for much of the time interval observed, the complexity of the fringe pattern near the plasma axis does not allow for an unambiguous assignment of fringe numbers. For these reasons, the analysis has been limited to a single z coordinate, z_o and $P(y, z = z_o)$ is found as a function of time in the pinch phase. Since the primary interest is in establishing the plasma distribution for interaction studies, the coordinate z_o is chosen to correspond with the focal position of the CO_2 laser. The sketch of Figure 27 is arranged to correspond with the orientation of the interferograms of Figure 27. This sketch locates the region of plasma for which data is collected. The interaction laser beam enters the field of view from the top of Figure 27 with the anode and cathode of the discharge being respectively off to the right and left of the frame.

The y coordinate of each visible maxima and minima along the scan line is recorded. Highly magnified reconstructions were made to aid in measuring the very closely spaced fringes near the plasma core. All photograph dimensions are scaled to real space plasma coordinates using the known image magnifications. The fringe functions are then Abel inverted with the assumption that, at least over the half-diameter region of the plasma column that is being measured, the plasma is very nearly axisymmetric. Though it may not be very satisfying to make this assumption, the following discussion points out two, more important, sources of error.

In order to specify the radial position of fringes, the location of $r = y = 0$ is required. The plasma axis, $r = 0$ is determined to be centered within the region where the fringe density is high. The best judgement that can be made here is that the origin, $y = 0$, is uncertain to no more than $\pm$ 0.5 mm which corresponds to about $\pm$ 2 mm in the pictures of Figure 26. The origin uncertainty enters into the unfolding computations in a rather complex way. However, for the results that will be shown, the net effect is primarily an uncertainty, by the same amount as given above, in locating the radial coordinate axis with respect to the electron density distrubition, rather than an error in the electron density itself. From a qualitative point of view, this effect is to be expected since the inversion integral is mainly sensitive to the derivative, $dP(y)/dy$ which is invariant under translation.

The fringe number P must also have a reference point corresponding to the outer boundary $y = r_o$ of the plasma where $P(r_o) = 0$. Far from the axis, the fringes are widely spaced and appear to extend beyond the field of view. The boundary r_o is obtained by plotting P(y) vs. y, with the horizontal axis being y. By extrapolating to large y, r_o and therefore P = 0, is determined as the point where P(y) becomes horizontal line. This procedure, amounts to simply terminating the distribution at some more or less arbitrary, but large maximum radius, which was usually estimated to be between 1.5 to 2 times the radius of the viewing ports. The precise choice of r_o was unimportant since the absolute error introduced is the order of 10^{16} to 10^{17} cm^{-3} and is quite insignificant compared to the electron densities of interest, namely 10^{18} to 10^{20} cm^{-3}.

At this point, the discussion of the interferograms may appear to be dominated by the uncertainties and assumptions required to extract the electron density distribution. This is, in part, a consequence of the inherently high sensitivity of interferometry. The interferograms do indeed give a very detailed picture of the plasma, but, in the following section, a more quantitative view is presented, and this will help put the uncertainties into better perspective.

9.3 Plots of the Electron Density Profile

Figure 28 shows the interferometric results for the electron density $n_e(r,t)$ over the time interval -90 ns $\leq t \leq 60$ ns. At times later than about t = +50 ns, the plasma has broken-up and the fringe patterns cannot be analyzed (see Figure 26(D)). Earlier than t = -90 ns, the plasma column has the combination of large radius and low density and produces a fringe pattern that extends well outside the field of view. This makes it difficult to extrapolate the fringe pattern to large radii. Information about the on-axis plasma density is absent due to the lack of observable fringes near r = 0. The profiles are extended from r = 0 to the first data point with a horizontal dashed line in order to indicate the region where fringes could not be measured with certainty. As well, these dashed lines are indicative of the accuracy with which the plasma axis could be defined. However, for the time interval shown, build-up of the electron density within the plasma column is well mapped out.

Though the interferometric data appears somewhat sketchy, it is worthwhile here to recall the results of the Thomson scattering measurements as presented in Figure 18. The time span covered by the interferometric data of Figure 28 represents only the central 15% of the scattering data. From this point of view, it is clear that the cavity dumped laser system has provided a considerable improvement in the temporal resolution capabilities of these experimental investigations. Such a large discrepancy in time scales makes it somewhat difficult to correlate the two experiments since, over the time span of the interferometric data, the scattering results yield only a few data points. Also, in terms of spatial resolution, the scattering measurements represent radially averaged densities, while the interferometric data would be expected to show higher peak densities. Nonetheless, the remainder of this discussion will provide some comparison of the interferometric data with previous results, and it will be seen that the correspondence is quite good.

A simple judgement of the reliability of the density profiles can be made on the basis of an inventory of electrons. Before firing the discharge, the total number of available electrons per unit length, namely, $0.63 \times 10^{19}\ cm^{-1}$, is determined by the initial fill conditions. Each of the electron density profiles were integrated, assuming cylindrical symmetry, to find the total number of electrons measured to be within the pinch column. An average of ten profiles shows the number of electrons to be

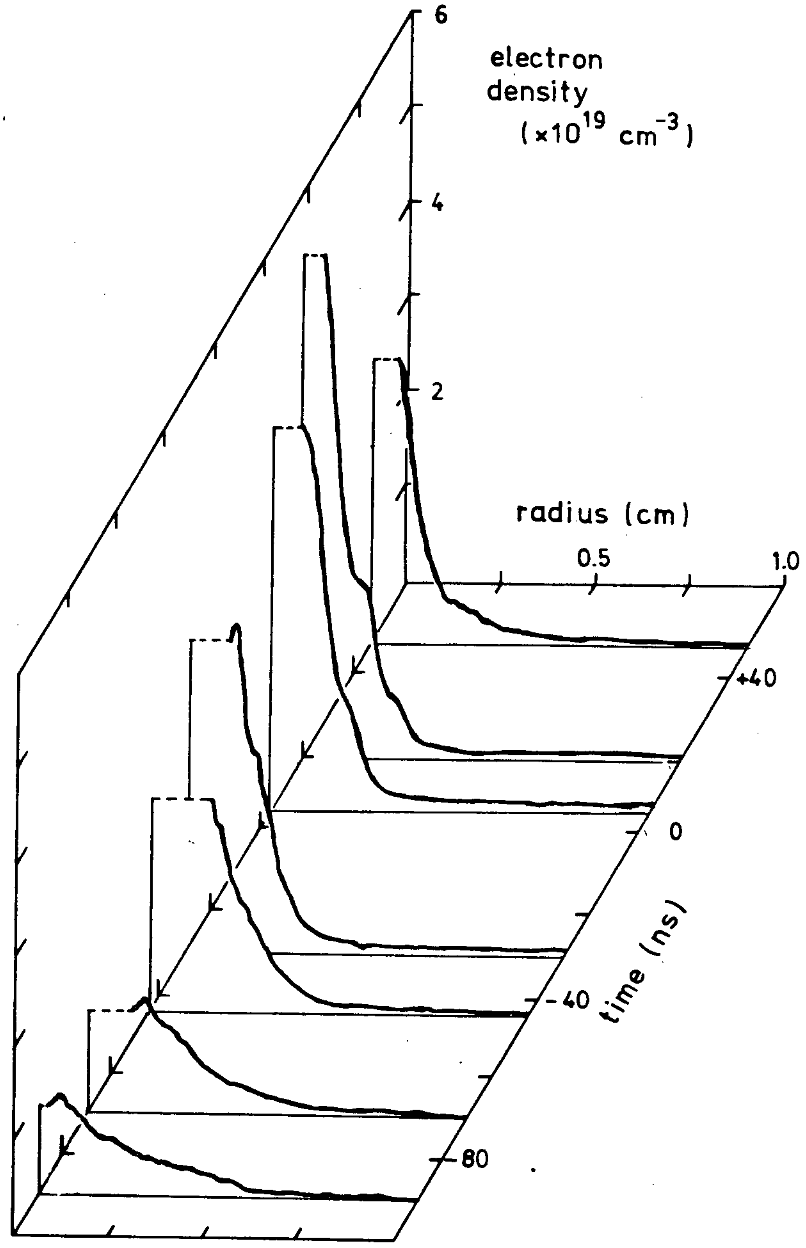

FIGURE 28

The plasma distribution during the pinch phase.

$0.47 \pm 0.9 \times 10^{19}$ cm^{-1}, which accounts for 75% of the fill gas. Of course, not all the gas will have been swept-up during the early implosion stage of the discharge. If 25% of the gas is assumed to remain uniformly distributed within the chamber, the background electron density would be 2×10^{16} cm^{-3}. With the observation field limited to comparatively small radii, this background electron density is somewhat below the present sensitivity. Therefore, a measured collection factor of 75% represents a lower bound. In view of this, the inventory of electrons is rather complete.

Figure 29 gives a comparison of the interferometric data with the Thomson scattering results. The open circles in this figure show the electron density measurements obtained from the scattering experiments plus one spectroscopic value at t = -80 ns. The interferometric data is shown as bars, but these bars require some explanation.

Because the scattering experiments lack spatial resolution in the radial direction, the density profiles of Figure 28 were therefore radially averaged over the 2 mm length of the scattering volume. The upper limit of the bars in Figure 29 show the average density assuming that the scattering volume was symmetrically located on the plasma axis. However, recalling the discussion in section 6.2 concerning the net red shift in some scattered spectra, an attempt was made to see if the interferometric data would be more consistent with a scattering volume that had been displaced with respect to the plasma axis. The lower limit of the bars in Figure 29 corresponds to averaging the density profiles assuming the scattering volume was displaced in the radial direction by 1 mm.

Even though there does appear to be a tendency for the scattering experiments to give lower electron densities, if error bars were placed on the scattering data, they would be approximately $\pm$ 30%. Consequently, any

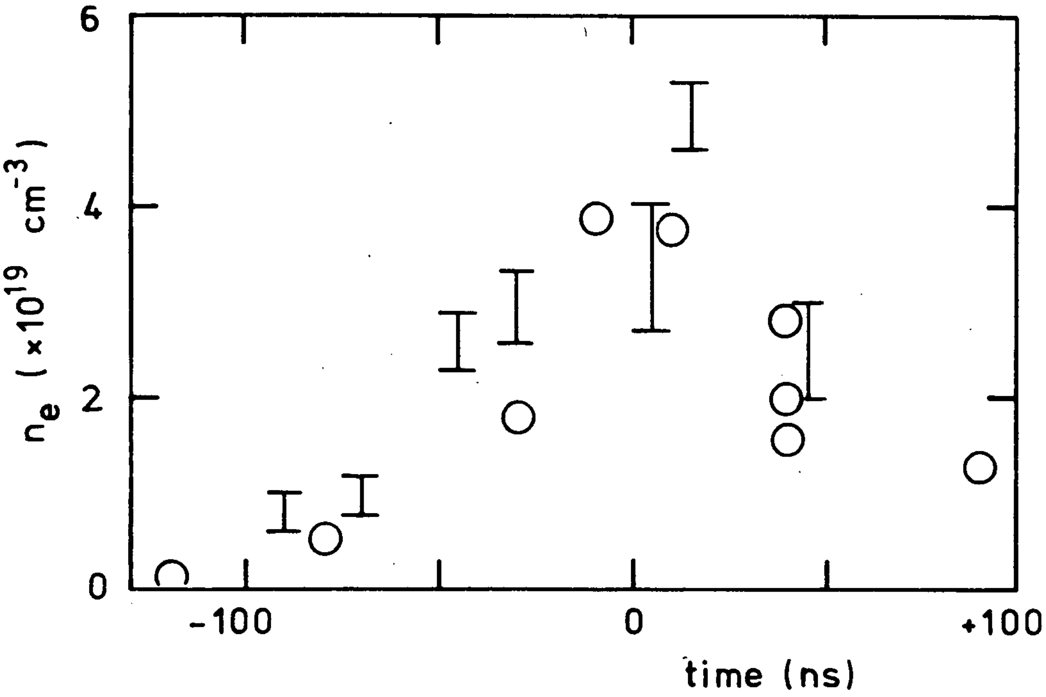

FIGURE 29

Comparison of the interferometric and scattering measurements. Open circles show the Thomson scattering results. The bars give the corresponding measurements that were extracted from the density profiles.

judgement concerning imaging in the scattering experiments would have tenuous justification. Nonetheless, this exercise in comparison illustrates clearly and most importantly, that, if the density profiles are averaged over the scattering volume, the interferometric and scattering measurements agree very closely.

On the other hand, if the density profiles are extrapolated to r = 0, the peak electron density on axis would be significantly higher (about a factor of two higher) than the scattering data shows. In particular, the peak density at maximum compression is indicated to be 7×10^{19} cm^{-3}. Now, in section 3.5, the shadowgram analysis provided an early estimate of 6×10^{19} cm^{-3} for the on-axis density at maximum compression. Although such a close correspondence between these two values may be fortuitous, the shadowgram experiment has proven to be a very reasonable estimator.

CHAPTER 10 CONCLUSION AND SUGGESTIONS

This final chapter will conclude the presentation of the experimental investigations performed as part of this thesis work. The following discussions will consider briefly each of the experiments, with the aim of providing (i) a review of the salient features of the high density Z-pinch plasma that have been observed, (ii) a summary of the diagnostic experiments, with some consideration given to (iii) their application to the laser/plasma interaction studies.

The first two experiments, namely, the streak and shadowgram photography, were performed and intended as an introduction to the previously unexplored high compression phase of this Z-pinch discharge. To this end, these initial experiments have been given a clear view of the evolutionof the on-axis plasma by establishing the plasma size, along with the basic structure and dynamics, as functions of time during the pinch phase. The plasma structure is characterized by two major components. A diffuse plasma shell, having relatively low electron density ($< 10^{18}$ cm^{-3}), collapses to a minimum outer radius of 0.25 cm. The plasma on-axis is shock compressed and heated to form the high density plasma core. This on-axis plasma develops from sub-millimeter dimensions and grows in size as plasma from the shell continues to accumulate and be compressed into the core.

These initial experiments have had one very important feature in common: they are simple and easy to do. Here, with only modest attention to experimental details, a wealth of quantitative information has been obtained. Refraction methods, such as the shadow photography, should not be overlooked as being well suited to the laser/plasma studies. At very high incident power densities, the interaction region is known to be characterized by small scale structure and steep density gradients (Milroy, et.al., 1978; Ng, et.al., 1979). With appropriate modifications, techniques based on refraction can be very sensitive probes of the interaction volume. For instance, through angular decomposition of the transmitted probe beam, one can obtain direct information about the plasma structure and shape without requiring any special (and often expensive) consideration for high spatial resolution.

From the Thomson scattering experiments, the plasma temperature was seen to range up to a maximum of 45 - 50 eV, and the electron density has been measured over a range of three orders of magnitude. The measured peak density, 4×10^{19} cm^{-3}, was closely corroborated by two independent estimates obtained from the streak and shadowgram observations.

Complex numerical modelling of the plasma collapse in a Z-pinch discharge (Hain, et.al., 1960) predicts strong shock heating of the on-axis plasma. However, the plasma temperature has not been an easily accessible parameter in this and similar discharges (e.g. Steel, et.al., 1978). Spectroscopic measurements have proved to be inappropriate during peak compression (Houtman, 1977, Albrecht, 1979) because of the high temperature and density. Also, more recent attempts to examine this Z-pinch using X-ray measurement techniques have proved inadequate because the plasma temperature is too low. The scattering experiments have therefore been vital for establishing the plasma temperature during the pinch phase. As well, it is believed that these Thomson scattering experiments represent one of the few, if not the first application of the ion feature as a routine diagnostic tool.

The scattering experiments will be of paramount importance for the interaction studies since they will interrogate the plasma at the microscopic level. All of the parametric processes expected to occur (Drake, et. al., 1974) have their signatures in the frequency and/or wavevector spectrum of the induced plasma fluctuations. The scattering experiments that have been presented were arranged to provide for high spectral resolution and single shot recording of the entire low frequency fluctuation spectrum.

In the low frequency regime of scattered spectra, the problem of stray light can be a very important one. Firstly, knowing that stray light is introduced because of refraction will aid in arranging for more efficient beam dumping. Also, the backscattered spectra of Figure 14 show that stray light can be isolated from scattered light via spectral resolution. Finally, the ruby laser has recently been modified to produce sub-nanosecond duration diagnostic pulses. If the optical gating method used in the present scattering experiments is correspondingly scaled in time, stray light can be further discriminated against on the basis of time of flight. Therefore, with the means made available by these experiments, stray light should not present a serious problem for future scattering investigations using this Z-pinch.

At the macroscopic level, the interferometric investigations have given a detailed picture of the plasma distribution. Qualitatively, the holes in the discharge vessel and return conductor have degraded the local symmetry of the plasma column. Consequently, some uncertainty has been introduced into the analysis of the fringe patterns. However, because the perturbations appear in an extremely reproducible manner, any effort to restore the plasma symmetry will be time well spent in providing for precision measurements of the density distribution. It is well established that surface instabilities develop on the plasma column as a result of perturbations in the shape of the vessel wall (Curzon et.al, 1964). It should, therefore, be possible to adopt the methods of Curzon et.al. and thereby produce a cylindrical perturbation which effectively overwhelms the azimuthal irregularity generated by the access ports.

It has been shown that, even though refraction effects on the interferometric experiments are not negligible, precise imaging was not an important requirement for examining the Z-pinch plasma itself. However, for the interaction experiments, the plasma region of interest will have dimensions the order of, and smaller than, the CO_2 laser focal spot size. This, in turn, will be significantly smaller than the dimensions of the plasma column. Then, imaging the interaction region with the accuracy indicated by Figure 22 may not be possible, particularly in view of the physical limitations imposed by the size of the discharge vessel. (Generally, high quality imaging of small objects requires placing short focal length optics close to the object - a situation not acceptable here.) The most reasonable solution would be to avoid refraction effects by using frequency doubled ruby laser light. The loss in sensitivity of a factor of 2 can be easily tolerated. The corresponding increase in the critical density (a factor of 4) will produce an enormous relaxation of the imaging requirements when the electron density is below about 1×10^{20} cm^{-3}.

Finally, by using the time differential nature of double exposure holography, short time scale variations in the plasma density in the CO_2 laser interaction region can be completely isolated from the unperturbed "background" plasma column. This was tested in a very preliminary way by photographing the plasma column itself, near peak compression, using a 12 ns inter-exposure separation. Though the plasma core does change over this time interval, all fringes outside the core were completely eliminated from the interference pattern. Considerable improvements can be made along these lines without a great deal of difficulty anticipated.

The investigations that were presented in this thesis have fulfilled their intended functions. A thorough examination of the Z-pinch plasma characteristics throughout the high density compression phase has given a complete data base of information on the initial target conditions, prior to irradiation with the CO_2 laser. The experiments that were presented provide a sequence of micro and macroscopic diagnostic methods that can be fruitfully applied to a detailed study of laser/plasma interactions.

REFERENCES

Albrecht, G.F., Ph.D. Thesis, University of British Columbia, (1979).

Albrecht, G.F.; Kallne, E. and Meyer, J., Rev. Sci. Instrum., 49(12), 1637 (1978).

Allen, J.E., Proc. Phys. Soc., B70, 24 (1957).

Armstrong, W.T. and Forman, P.R., Appl. Optics 16(1), 229 (1977).

Artsimovich, L.A., in 'Controlled Thermonuclear Reactions' Ch. 6, (Gordon and Breach, 1964).

Barnard, A.J. and Ahlborn, B., Am. J. Phys., 43(7), 573 (1975).

Barnard, A.J. and Gulizia, C., Can. J. Phys., 58, 565 (1980).

Born, M. and Wolf, E., in 'Principles of Optics', 5th Edition, 123 (Pergamon, 1975).

Chang, M. and George, N., Applied Optics, 9 (3), 713 (1970).

Chen, F.F., In 'Introduction to Plasma Physics', (Plenum, 1974).

Collier, R.J., Lin, L.H. and Burchhardt, C.B., 'Optical Holography', (Academic, 1971).

Curzon, F.L.; Hodgson, R.T. and Churchill, R.J., J. Nuclear Energy C, 6, 281 (1964).

Desilva, A.W. and Goldenbaum, G.C., in 'Methods of Experimental Physics' Edited by R.H. Lovberg and H.R. Griem, Vol. 9A, Ch. 3, 61 (Academic, 1970).

Drake, J.F.; Kaw, P.K.; Lee, Y.C.; Schmidt, G.; Liu, C.S. and Rosenbluth, M.N., Phys. Fluids, 17 (4), 778 (1974).

Evans, D.E. and Katzenstein, J., Rep. Prog. Phys., 32, 207 (1969).

Fan, L.S. and Squire, W., Computer Phys. Commun., 10, 98 (1975).

George, T.V.; Goldstein, L.; Slama, L. and Yokoyama, M., Phys. Rev., 137 (2A), 369 (1965).

Graube, A., Appl. Optics, 13 (12), 2942 (1974).

Grek, B.; Martin, F.; Johnston, T.W.; Pepin, H.; Mitchel, G. and Rheault, F., Phys. Rev. Lett., 41(26), 1811 (1978).

Hain, K.; Hain, G.; Roberts, K.V.; Roberts, S.J. and Koppendorfer, W., 7, Naturforschg, 15 (A), 1039 (1960).

Hilko, B., Meyer, J., Albrecht, G., and Houtman, H., J. Appl. Phys., 51 (9), 4693 (1980).

Holder, D.W. and North, R.J., 'Schlieren Methods', Notes on Applied Science No. 31, (HMSO London, 1963).

Houtman, H., M.Sc. Thesis, University of British Columbia, (1977).

Jackel, S.; Perry, B. and Lubin, M., Phys. Rev. Lett., 37(2), 95 (1976).

Jahoda, F.C. and Sawyer, G.A., in 'Methods of Experimental Physics', Plasma Physics, Vol. 9 (b), 1 (Academic, 1971).

Keilmann, F., Plasma Physics 14, 112 (Pergamon, 1972).

Kogelschatz, U. and Schneider, W.R., Applied Optics, 11 (8), 1822 (1972).

Kunze, H.J., in 'Plasma Diagnostics', 550 (North-Holland, 1968).

Leontovich, M.A. and Osovets, S.M., J. Nuclear Energy II, Vol. 4, 209 (1957).

Machewirth, J.M., Optical Spectra, December (1979).

Milroy, R.D.; Capjack, C.E.; McMullin, J.N. and James, C.R., Can. J. Phys., 57, 514 (1979).

Morgan, C.G., Rep. Prog. Phys., 38, 621 (1975).

Ng, A.; Salzmann, D. and Offenberger, A.A., Phys. Rev. Lett., 43 (20), 1502 (1979).

Salpeter, E.E., Phys. Rev., 120 (5), 1528 (1960).

Salpeter, E.E., J. Geophys. Res., 68 (5), 1321 (1963).

Schreiber, P.W.; Hunter II, A.M. and Smith Jr., D.R., Plasma Physics, 15, 635 (1973).

Shmoys, J., J. Appl. Phys., 32 (4), 689 (1961).

Siebe, J., Phys. Fluids, 17 (4), 765 (1974).

Siegman, A.E., IEEE J. Quantum Electron., QE-9, 247 (1973).

Simpson, R.W. and Talmi, Y., Rev. Sci. Instrum., 48 (10), 1295 (1977).

Steel, D.G.; Rocket, P.D.; Bach, D.R. and Colestock, P.L., Rev. Sci. Instrum., 49 (4), 456 (1978).

Sweeney, D.W.; Attwood, D.T. and Coleman, L.W., Appl. Optics, 15 (5), 1126 (1976).

Rosenbluth, M.N. and Rostoker, N., Phys. Fluids, 5 (7), 776 (1962).

Vest, C.M., Appl. Opt., 14 (7), 1601 (1975).

Vest, C.M., 'Holographic Interferometry', (John Wiley & Sons, 1979).

Vuylsteke, A.A., J. Appl. Phys., 34 (6), 1615 (1963).

Zel'dovich, Y.B. and Raizer, Y.P., in 'Physics of Shock Waves and High-Temperature Hydrodynamic Phenomenon', Vol. 1, 258 (Academic, 1966).

APPENDIX A

TRIGGERING OF THE DISCHARGE

Details of the design, construction and operation of the discharge circuit are well documented in our laboratory (e.g.: Houtman, 1977). This appendix has been included here in order to establish the necessary documentation of those changes to the circuitry that were made by the present author.

Figure A-1 shows one of the six main gap trigger circuits. The master gap is an entirely co-axial arrangement, housing the six 2700 pF trigger capacitors. The pre-ionization circuit that was added to the master gap is described via Figure A-2. Note that the Z-pinch anode has a 3 cm diameter hole in the center in order to accommodate the trigger electrode. With this arrangement, and, at the current operating conditions, the pre-ionization was sufficient to reduce the jitter in the main discharge from greater than 50 ns to less than 5 ns.

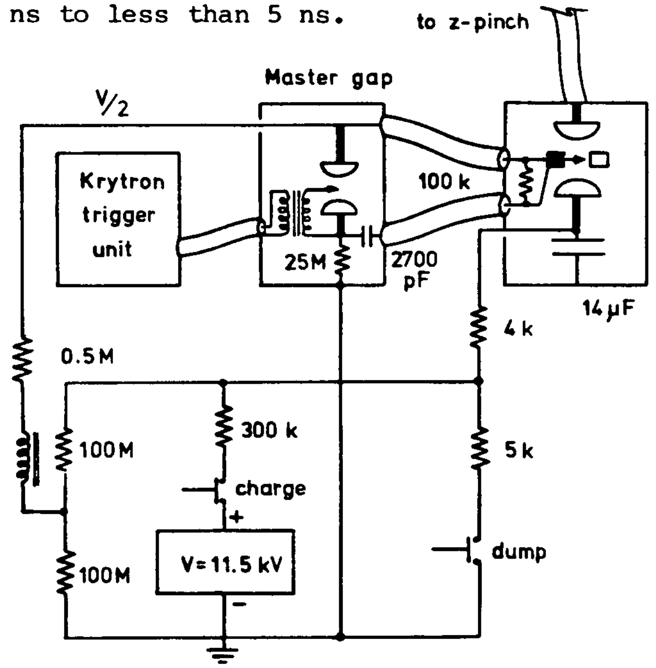

FIGURE A-1

Biasing and main gap trigger circuits.

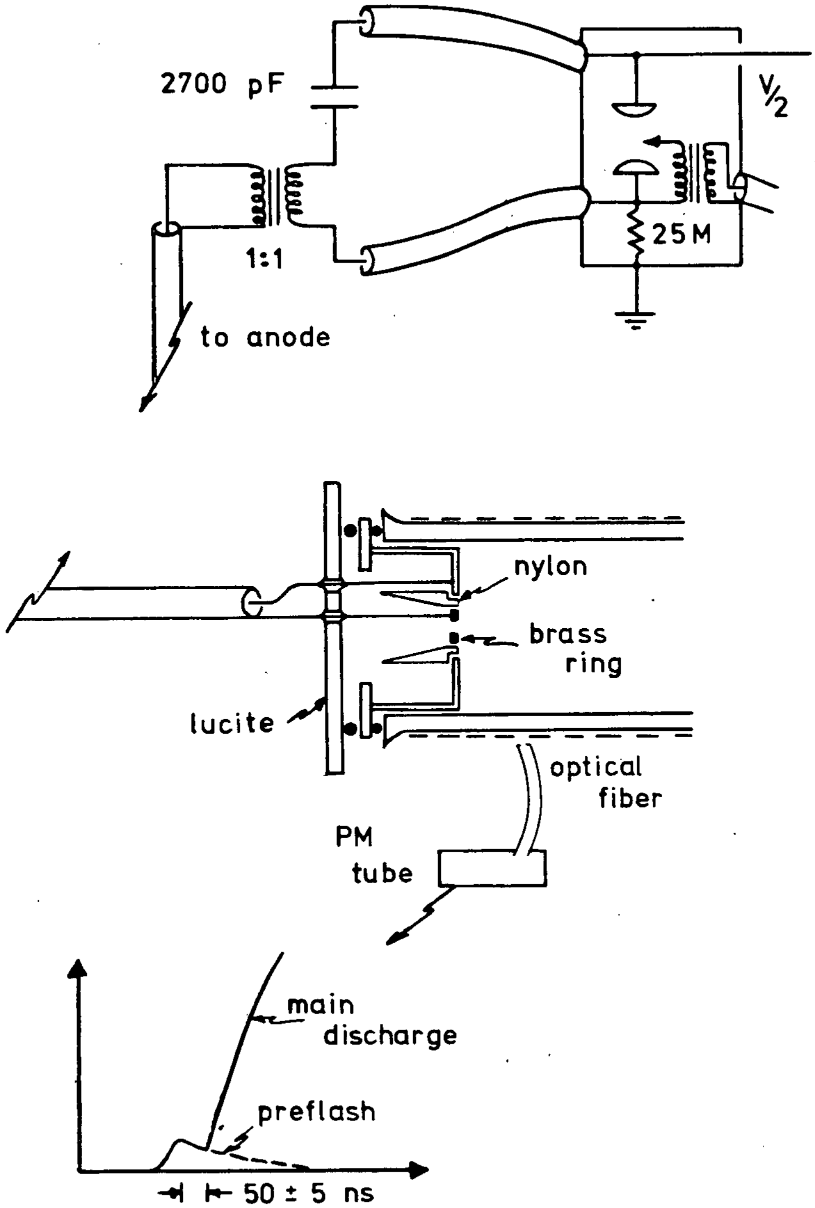

FIGURE A-2

Description of the pre-ionization.